UNIVERSIDAD
DE ANTIOQUIA
1803

Development of Multilayer Systems Al/NAA/TiO_2 with Variable Reflectance for Optics Applications

Doctoral Thesis in Materials Engineering

Sara María Aguilar Sierra

Supervisor:

Félix Echeverría Echeverría, PhD

Centro de Investigación, Innovación y Desarrollo de Materiales - CIDEMAT

UNIVERSIDAD DE ANTIOQUIA

MEDELLÍN

2018

Centro de Investigación, Innovación y Desarrollo de Materiales CIDEMAT

Sede de Investigación Universitaria – SIU

Universidad de Antioquia

Cr 53 # 61 – 30

Medellín, Colombia

This Doctoral thesis has been carried out in the Centro de Investigación, Innovación y Desarrollo de Materiales (CIDEMAT) at the Universidad de Antioquia, in the framework of the project: "*Desarrollo de nuevos sistemas de alta reflectividad para aplicaciones en concentradores solares térmicos*" founded by Departamento Administrativo de Ciencia, Tecnología e Innovación – COLCIENCIAS (Colombia), with the Universidad de Antioquia. Also, by the Spanish Ministry of Economy and Competition under grants number TEC2015-71324-R (MINECO/FEDER), the Catalan Government AGAUR 2017-SGR-1527 and the ICREA under the 2014-ICREA Academia Award. I was able to conduct this work thanks to the call number 617 of 2013 Doctorados Nacionales COLCIENCIAS.

ACKNOWLEDGMENTS / AGRADECIMIENTOS

Agradezco enormemente a mi Pacho por acompañarme en esta montaña rusa de emociones y ser mi polo a tierra, por tantas risas y amor. Gracias mami, el amor que siento por aprender, entender y descubrir cosas nuevas definitivamente viene de ti, siempre tienes las respuestas que necesito escuchar. Gracias a mis hermanitos Rober y Kike, a mis cuñadas Ana y Alejita y a mi tía María que me recargaron de energías para atravesar este camino.

Agradezco a mi tutor Félix, por la paciencia, el acompañamiento y sobre todo por los valiosos aportes académicos que me hizo durante este proceso. Quiero también agradecer al profesor Jaime Osorio por asesorarme y guiarme cuando más lo necesitaba. Gracias al profesor Lluis F. Marsal por recibirme en su grupo y valorar mi investigación, muchas gracias también al profesor Josep Ferré por enseñarme cómo escribir un artículo, por acompañarme durante mi pasantía y por compartir sus conocimientos conmigo.

Gracias a Nacho y Rafa de Ruta N, a Juan Humberto de estado sólido y a René de Eafit por resolver mis dudas, explicarme fenómenos e interesarse en responder mis preguntas ópticas. Gracias a Adrián por resolver cualquier inconveniente que se me presentara en el laboratorio. Gracias a Tiff por ser un ejemplo, por enseñarme tantas cosas. A Robin, mi compañero de anodizado, por las valiosas discusiones. Gracias a Felipe por ayudarme con el electropulido.

Gracias a mis amigos, todos ustedes aportaron momentos invaluables que me llenan de amor y fortaleza. Johi, Chris Daniel, Andre, Nata, Dani, Ruby, Triny, Natha, Marllo, Ricardo y la profe Claudia.

Agradezco a todos los profesores del Centro de Investigación, Innovación y Desarrollo de Materiales (CIDEMAT) quienes enriquecieron mi trabajo con sus preguntas y comentarios durante los seminarios. Gracias a los compañeros de CIDEMAT y de NEPhoS (Universitat Rovira i Virgili) porque al ser grupos interdisciplinarios aportaron a mi desarrollo profesional y personal.

Finalmente, agradezco al “Departamento Administrativo de Ciencia, Tecnología e Innovación–COLCIENCIAS” por el apoyo financiero.

ABSTRACT

In this doctoral thesis, aluminum anodization was used to produce nanoporous anodic alumina (NAA) structures. The influence of the fabrication parameters on the NAA physical characteristics was determined. The effective medium approximation (E.M.A.) and Bruggeman's equations were used to model and simulate the optical properties of the Al/NAA systems and as support to understand its optical behavior (reflectance and photoluminescence). Afterwards, the NAA samples were used to develop multilayer systems by means of titanium dioxide (TiO_2) spray pyrolysis. The Al/NAA/TiO_2 systems were also simulated and their optical properties were analyzed.

As a starting point, as anodizing pretreatment aluminum electropolishing was carried out in three substrates and using the three different electrolytes described next.

First, the aluminum alloy (AA) 8005 was electropolished using an acid electrolyte composed of sulfuric acid (H_2SO_4), phosphoric acid (H_3PO_4) and chromic acid (H_2CrO) recording both current density and time. Second, a chromium free electrolyte was used to electropolish commercially pure AA 1100; this solution was composed by H_2SO_4, H_3PO_4 and nitric acid (HNO_3). Third, the same alloy was electropolished in an alkaline electrolyte constituted by sodium phosphate (Na_3PO_4), aluminum sulfate ($Al_2(SO_4)_3$) and sodium hydroxide (NaOH). Finally, the alkaline electrolyte was used as anodizing pretreatment of AA 1100 and pure aluminum (99.999%) surfaces.

Afterwards, the materials and methods for fabricating NAA were presented. The previously electropolished AA 1100 was anodized at different potentials and during different times to establish the proper anodizing conditions to be used during the pure aluminum anodization. When the best anodizing conditions were found, 99.999% pure aluminum was used as a substrate to produce NAA samples with the two-step anodization process under mild anodization conditions in oxalic acid ($H_2C_2O_4$).

In consequence, the effect of the anodizing parameters such as applied potential, temperature and duration of the first step on NAA morphology and ordering is discussed. Samples with different thickness, pore diameter, interpore distance and ordering level were fabricated.

Later, titanium dioxide (TiO_2) layers were sprayed on top of the previously characterized NAA samples. The TiO_2 layers were deposited by spray pyrolysis of a solution of titanium isopropoxide in anhydrous ethanol and sintered at 500°C. TiO_2 thickness was modulated and the optical response measured.

Finally, the optical properties of NAA are discussed in terms of photoluminescence (PL) and reflectance (R). The reflectance behavior of the Al/NAA and Al/NAA/TiO_2 multilayer systems was analyzed with numerical simulations. The numerical simulations were based on the Transfer Matrix Method. The porosity of both the NAA film and the porous sprayed TiO_2 film, was modeled using a Bruggeman effective medium approximation (E.M.A.).

The results of this thesis are expected to highly contribute to the optical understanding of NAA and NAA/TiO_2 in the UV-Vis zone in order to develop new nanodevices and optical applications.

LIST OF PRODUCTS OBTAINED DURING THE DOCTORAL RESEARCH

PUBLISHED PAPERS

i. Improvement of Electropolishing of 1100 Al Alloy for Solar Thermal Applications. Sara María Aguilar-Sierra & Félix Echeverría E.
Journal of Materials Engineering and Performance (2018) 27:1387-1395.

SUBMMITED PAPERS

i. Titanium Dioxide-Coated Nanoporous Anodic Alumina Optical Properties.
Sara María Aguilar-Sierra, Josep Ferré-Borrull, Félix Echeverría E, Lluis F. Marsal.
Applied Surface Science

PAPERS IN PROGRESS

i. Growth mechanisms of porous anodic alumina through time.
Sara María Aguilar-Sierra & Félix Echeverría E.

ii. The Influence Anodizing Potential on the Optical Properties of Aluminum/Nanoporous Anodic Alumina/ Titanium Dioxide Systems.
Sara María Aguilar-Sierra, Josep Ferré-Borrull, Lluis F. Marsal, Félix Echeverría E.

CONFERENCES

i. Influence of Pore and Cell Sizes on Aluminum/Nanoporous Alumina Optical Properties.
Sara María Aguilar-Sierra & Félix Echeverría E.
NANOP Nanophotonics and Micro/Nano Optics International Conference, Paris (France). Dicember 7-9, 2016.

ii. Electropolishing 1100 Aluminum Alloy Mirror for Solar Concentrators
Sara María Aguilar-Sierra & Félix Echeverría E.
Graduate Students Meeting on Electronics Engineering. Departament de Enginyeria Electrònica Elèctrica y Automàtica, Universitat Rovira i Virgili, Trarragona (Spain). June 28-29, 2018.

INTRODUCTION

Over the last decades, developments in optical telecommunications, space applications and integrated optics are challenging researchers to design and optimize materials making optical multilayers and thin-film coatings in the core of recent investigations [1,2]. Optical multilayers have been used as interferential coatings [3,4], antireflection [5,6], perfect mirrors [7,8] and absorbing systems [9]. Moreover, in the design of structures for infrared detectors, bolometers, optical sensors, among others [10,11]. It is well known that the optical response of a multilayer system is determined by the interference generated by the multiple light beams reflected in each interface of the coating. It can be expected that knowing the properties of the constituent material of each layer provides information about the final response of the system, supporting the development of new or improved materials [12–17].

A wide range of materials and synthesis approaches is available to design multilayer coatings with complex reflection and transmission profiles. Recently, nanoporous anodic alumina (NAA) produced by anodization of aluminum has been identified as a promising material due to its intrinsic properties in terms of mechanical robustness, thermal stability and chemical inertness as well as controllable and versatile nanopore geometry and also exhibiting high aspect ratio and facile fabrication [18–23]. Furthermore, the effective medium of this nanoporous material can also be engineered with precision by carefully controlling the anodization parameters. Meanwhile, titanium dioxide (TiO_2) exhibits good photocatalytic properties, high refractive index, is transparent in the visible and near infrared range while absorbs in the UV zone, presents good adhesion and high stability against mechanical abrasion, chemical attack and high temperatures [24–26]. However, the characteristics of TiO_2 films are strongly dependent on the preparation methods and the deposition parameters [27–30].

This doctoral thesis aims to understand the optical properties of Al/NAA (aluminum/nanoporous anodic alumina) and Al/NAA/TiO_2 (aluminum/nanoporous anodic alumina/titanium dioxide) systems obtained by means of aluminum anodizing. The TiO_2 coated systems were obtained using the spray pyrolysis technique. The optical modulation in terms of reflectance was achieved controlling the anodizing parameters and through the number of deposited TiO_2 layers. The relationship between the anodizing process variables, morphology, composition and thickness of NAA with the optical properties of the developed systems was studied. Simulations were performed with the effective medium approximation (E.M.A.) as supporting tool to understand the optical behavior of the multilayer systems. Scanning Electron Microscopy (SEM) and Atomic Force Microscopy (AFM) were used to study the morphology of the coatings. Spectrophotometry UV-Vis and fluorimetry were used to measure the reflectance and photoluminescence PL of the developed systems.

HYPOTHESIS

It is possible to modify and control the optical response of multilayer systems Al/NAA/TiO_2 by tuning the morphological characteristics of the NAA layer.

OBJECTIVES

General Objective

To develop multilayer systems Al/NAA/TiO_2 with different reflectance percentages controlled by morphology and thickness of NAA layer coated with transparent TiO_2 for its application in optical systems.

Specific Objectives

- To set the aluminum AA 1100 electropolishing parameters (chemical nature, electrolytes concentration, electropolishing time, current density, electrolyte temperature) in order to obtain surfaces with a reflectance percentage 90 % and less than 600 nm roughness.
- To obtain porous anodic aluminum coatings on the electropolished aluminum substrate by anodization process and evaluate the influence of the anodizing parameters on the morphological distribution and chemical composition of the anodic coatings by means of surface and compositional characterization techniques (SEM/EDS, AFM).
- To develop transparent TiO_2 films by means of sol gel technique on the selected Al/NAA systems and to evaluate the influence of the number of layers on their morphology.
- To study the relationship between obtained multilayer systems optical properties and morphological distribution, chemical composition and thickness of NAA and TiO_2 coatings.

THESIS STRUCTURE

The reader is going to find five chapters as follows:

Chapter 1 focuses in the electropolishing of aluminum as a pretreatment for several applications, specifically anodization.

Chapter 2 describes the fabrication of nanoporous anodic alumina (NAA) and the effect of anodizing parameters on NAA ordering and morphology.

Chapter 3 describes the influence of pore diameter and thickness on the optical behavior of NAA and introduces a model to better understand the NAA and the NAA/TiO_2 optical properties.

Chapter 4 discusses the influence of anodizing potential on optical properties (PL and R) of NAA and deals with the optical effect of spraying TiO_2 on top of NAA. An improved model is introduced to clarify the NAA and the NAA/TiO_2 optical response. Simulations are performed to analyze the optical response of the evaluated systems.

Chapter 5 summarizes the conclusions of this doctoral dissertation and includes some additional comments.

Contents

1. ALUMINUM ELECTROPOLISHING

1.1 Introduction

Electropolishing (EP) is a surface treatment that produces smooth metallic surfaces. The metal piece to be electropolished serves as the anode. A power source produces an electrical current that passes from the anode to the cathode causing the oxidation of the metal surface and the removal of irregularities, which are dissolved in the electrolyte and diffuses through the film to the cathode at a controlled rate. The EP process involves electrochemical anodic dissolution on the surface of anode according to the equations 1 and 2 [31].

$$Al \rightarrow Al^{3+} + 3e^{-} \quad (1)$$

$$2Al + 6OH^{-} \rightarrow Al_2O_3 + 3H_2O + 6e^{-} \quad (2)$$

The electrochemical reaction occurs under diffusion mechanisms dissolving metal ion, acceptor species from the electrolyte and water molecules. Commonly the diffusion limitation is the metal ion where a liquid layer is generated by a viscous complex salt near the surface, this layer presents higher electrical resistivity on the anode related to the electrolyte volume. Metallic surfaces are inhomogeneous making the thickness of the viscous layer over the material surface non-uniform resulting in a different ohmic resistance from the cathode to the anode. This causes greater dissolution of the peaks compared to the valleys, thus creating a uniform surface profile [32,33].

The current density (j) vs potential (V) curve, characteristic of an electropolishing system, depend on many factors such as orientation of anode and cathode in the bath, cathode material used, anode to cathode surface area ratio, electrolyte type, temperature of the electrolyte and degree of agitation. Jacquet [34], found that depending on the potential applied the result can be polishing, pitting or gas evolution. The electropolishing is usually done by applying a voltage on the plateau of the j-V curve. However, the best polishing results were reported to appear when the applied voltage is just below the potential at which the oxygen evolution starts [33]. Hoar et al. [35] related this behavior to the viscous layer formed on the surface while electropolishing. The dissolution of metals results in formation of cations that move through the film to the solution, leaving vacancies at the metal-film interface. If the vacancy concentration increases too much, they could merge and form voids that might lead to the detachment of the ion conducting film from the surface. To avoid this, the potential should be kept as high as possible while ensuring that anions in the film are kept pressed against the metal surface in the receding metal-film interface [36].

Electrolytes suitable for electrolytic polishing include those composed by acids such as perchloric acid, phosphoric acid, sulfuric acid, chromic acid, mixture of acids and

also salts [37–39]. Otherwise, there are the alkaline electrolytes and those composed for methanol and nitric acid [40]. Electropolishing electrolytes containing perchloric acid have been well known for their strong oxidizing properties and are highly used for aluminum electropolishing, especially when it is used as a flat substrate for applications such as anodizing [2,41–55]. However, perchloric acid is particularly prone to decompose and react, and in certain cases it is dangerous, mainly when exposed to temperatures higher than 38°C or when it is concentrated [56].

In 1982 [57], were published the processing conditions for three common electrolytes to electropolish aluminum. The first one was composed by 2.5 % w/w fluoroboric at 29 °C with a current density between 1-2 A/dm^2, for 5 to 10 minutes. The second one consisted of 15% sodium carbonate, 5% de trisodium phosphate at a pH of 10.5, keeping the temperature between 79 and 82°C, using a current density between 2-3 A/dm^2. The third process was a mixture of 4-45% of sulfuric acid, 40–80% phosphoric acid, 0.2-9% chromic acid using a temperature of 71-93 °C and a current density of 2.5 y 95 A/dm^2. A different recommended process to obtain smooth surfaces used a solution made of 70% H_2SO_4, 15% H_3PO_4, 1% nitric acid between 75-85 °C for 2-10 min and a current density between 10-15 A/dm^2; the attractive part of the last process was due to the use of less toxic solutions to generate mirror-like surfaces.

Adelkhani, H., et al [31] evaluated a bath composed by a mixture of 58% phosphoric acid, 14% sulfuric acid, and 8% chromic acid in distilled water and reported that under the adequate conditions they achieved a mirror-like surface with more than 90% of reflectivity. Alam K.M. et al. [58] proposed a chemical polishing electrolyte avoiding perchloric acid and the related hazards discussed before. The electrolyte consisted of 15 parts of nitric acid and 85 parts of phosphoric acid. The polishing was suitable as pretreatment for aluminum anodization, reporting roughness values of 66.5 nm, like the obtained with perchloric acid mixtures.

There are commercial electropolishing processes such as the Brytal process designed in Britain, which uses an alkaline electrolyte composed by sodium carbonate and trisodium phosphate, where some variations can be included [59]. Otherwise, it is the Alzak process, developed in America for reflector finishing that uses two types of baths: Fluoborate electrolytes and hydrofluoric acid. It is also the Batelle process involving sulphuric, phosphoric and chromic acids. The Aluflex process is based on sulfuric and chromic acids and was developed in Germany. Over time different processes have been tested and used; a good summary can be found in [57,59].

It has been well established that in order to obtain a smooth surface, it is necessary to consider metallurgical factors such as size and orientation of grains and chemical

compositions that can lead to a multiple phase metal. Metal characteristics such as grain size, segregations, oxide inclusions, lamination marks or orientations can be controlled by applying different heat treatments [60–67]. Most metallic sheet materials are the result of cold rolling processes that induce deformation and grain orientation. Annealing is a heat treatment used to relieve stresses and to homogenize the grain size and to transform elongated grains into equiaxial grains [68].

It has been reported that the aluminum grain size is one of the key elements to control the domain size in ordered nanoporous anodic alumina (NAA), then, larger aluminum grains can promote larger domains in self-ordered NAA [50]. The main factors to control the grain size are the temperature and time used during a heat treatment process, previously to electropolishing and anodizing processes [67,68]. In consequence, heat treatments performed to the AA 1100 before electropolishing were evaluated in this chapter. Spectrophotometry UV-Vis, profilometry, SEM and EDS have been used to investigate the conditions under which the electropolishing process can be improved. High total reflectance and low roughness were obtained.

1.2 Experimental Procedure

At the beginning, this research was carried out in an aluminum alloy AA 8005 in order to find the best electropolishing conditions using a widely reported acid electrolyte with chromium (E1). Current density and time were evaluated (see table 1.2). Nevertheless, the chromic acid is known for its hazardous characteristics because Chromium (IV) is one of its constituents, which is an oxidizer and a carcinogen in humans and experimental animals [69]. Due to the previous, the acid electrolyte was changed for a chromium free acid electrolyte (E2) and the electropolishing parameters evaluation was restarted using a commercially pure aluminum alloy AA 1100, considering that the final substrate to be used would be pure aluminum. Theoretical composition of AA 8005 and AA 1100 are shown in table 1.1.

Table 1. 1 Composition of the used aluminum alloys [70].

Aluminum grade	Si	Fe	Cu	Mg	Mn	Zn	Unspecified other elements	
							Each	Total
AA 8005	0.22-0.50	0.40-0.80	0.05	0.05	-	0.05	0.05	0.15
AA 1100	0.95 Si+Fe		0.05-0.20	-	0.05	0.10	0.05	0.15

This chapter can be divided in two main sections. The first part was done in order to compare two electropolishing processes and their influence in aluminum total reflectance and the second part was carried out to evaluate the effect of heat treatment on the total reflectance of electropolished samples.

Commercial sheets of AA 8005, AA 1100 and Al 99.999% pure (Al 5N) were used. Prior to electropolishing, the AA 8005 and AA 1100 samples were mechanically polished up to 1200 grid and degreased in an ultrasonic acetone bath for 5 min and then rinsed with distilled water.

1.2.1 Electrolyte evaluation

The AA 8005 was electropolished using an acid electrolyte with chromium. Then, a commercially pure AA 1100 was electropolished with a free chromium acid electrolyte and with an alkaline electrolyte and the reflectance and roughness results were compared. Afterwards, based on the electrolyte evaluation results, the alkaline electrolyte was used as pretreatment for anodizing the AA 1100 and Al 5N substrates. The used electrolytes and its electropolishing conditions are presented in Table 1.2.2.

Table 1.2. Evaluated electropolishing parameters.

Electrolyte	Composition	Alloy	Temperature (°C)	Conditions	Time (min)
Acid: E1	58% v/v H_2SO_4, 14% v/v H_3PO_4, 8% v/v H_2CrO_4, 20% distilled water [31]	AA 8005	75-90	5 A/dm^2, 10 A/dm^2, 15 A/dm^2, 20 A/dm^2, 25 A/dm^2	2, 5, 10, 15
Acid: E2	70% v/v H_2SO_4, 15% v/v H_3PO_4, 1% v/v HNO_3, 14% distilled water [61]	AA 1100	75-90	1.54 A	2, 5, 10, 15, 18, 25
Alkaline: Modified Brytal	150 g Na_3PO_4, 20 g $Al_2(SO_4)_3$ 10 g NaOH in 1l solution [59].	AA 1100	80	3 V (from j-V curve)	10, 11, 12, 13, 14, 15, 16
		Al 5N	80	3 V	10

With the aim of better understand the electropolishing behavior of each system, polarization curves (potential vs current density) were obtained at 80 °C until a voltage of 20 V was reached and using a scan rate of 1 V per second with a holding time of 15 s at each potential.

The total reflectance (R_T) of the electropolished samples was determined on at least three specimens of each condition by UV-Vis spectroscopy, using a Cary 100 spectrophotometer with integration sphere with an 8° edge. The evaluated wavelengths were between 200 nm and 800 nm at a speed of 10 nm/s. The used reference was a Sinoy mirror ® with 93% R_T in the 400-600 nm range.

The roughness of the electropolished surface was measured by profilometry with a DEKTAK XT (Bruker) profilometer using a load of 4 mg and 5000 µm length in 30 s. At least five measurements were performed for each sample.

1.2.2 Heat treatment evaluation

To evaluate the effect of the heat treatment holding time on the reflectance of the electropolished samples and to obtain larger size grains, the AA 1100 samples were heat treated at 500 °C during 5 min, 15 min, 30 min, 1 h, 2 h, 4.5 h, 7.5 h and 14 h and then electropolished under the same conditions for 15 minutes using the modified Brytal process. Additionally, a set of samples was heat treated at 345 °C for 5 minutes, and the reflectance was evaluated. The microstructural characterization and the electropolished surfaces were obtained by means of optical microscopy (OM) and scanning electron microscopy (SEM). The reflectance percentage of previously heat-treated electropolished samples was measured as described above.

1.3 Results and discussion

Figure 1.1 shows the total reflectance (R_T) curves of AA 8005 electropolished with the chromium containing electrolyte. To better understand the graph, the electropolishing times are distinguished by colors; black: 2 min, red: 5 min, green:10 min and blue: 15 min and the applied current densities are differentiated by shapes; 5 A/dm^2: filled square (■), 10 A/dm^2: empty square (□), 15 A/dm^2: empty square with a x inside (⊠), 20 A/dm^2: filled circle (●) and 25 A/dm^2: empty circle (○). Additionally, color rectangles are showing the covered reflectance values related to each color (current density). In the inset of Figure 1.1 the maximum reflectance between 400 nm and 700 nm was plotted vs current density for each evaluated time, the same colors were used as indicated above.

Figure 1.1 show high reflectance values from the visible to the ultraviolet (UV) spectral range, followed by a reflectance reduction around 200 nm as previously reported for smooth aluminum surfaces [60,71]. It can be also observed that in the visible range, the samples electropolished for 15 min exhibited variations in reflectance around 20%, while the samples electropolished for 2 min and 5 min showed half of that variation and those electropolished during 10 min presented just 5% of variation in the reflectance among the evaluated current densities. From the inset, it can be noticed that there is a tendency for all the evaluated times to present higher reflectance values when electropolishing between 10 and 20 A/dm^2, except for the sample electropolished at 15 A/dm^2 during 15 min.

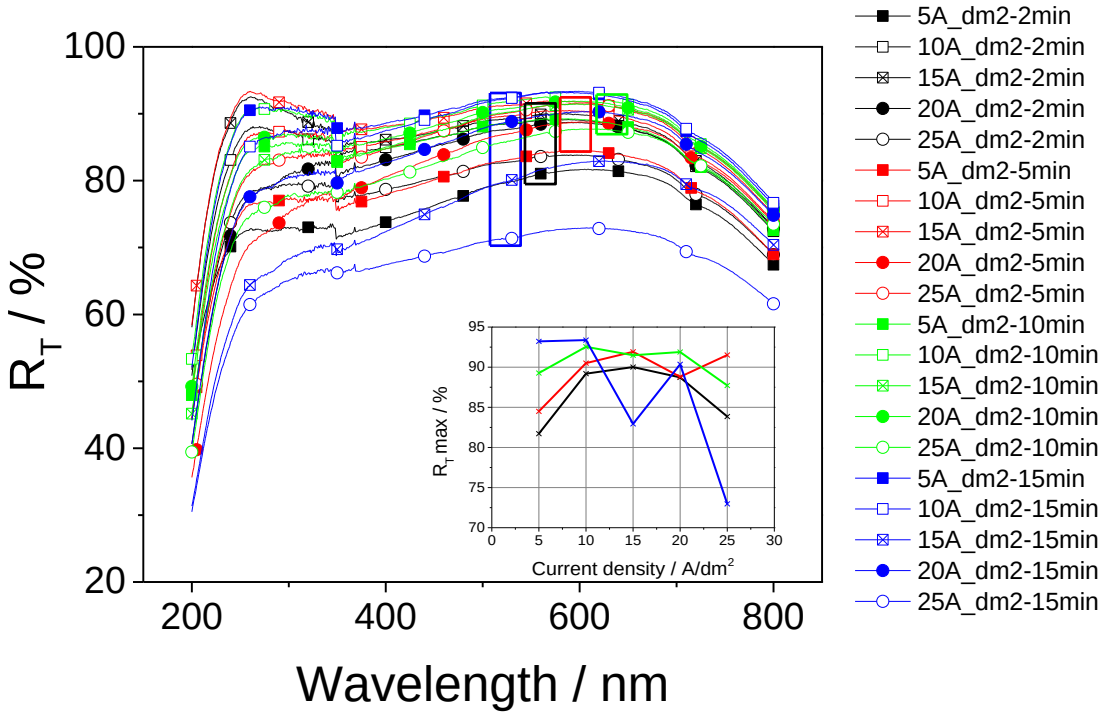

Figure 1.1 Total reflectance curves of AA 8005 electropolished with the chromium containing electrolyte. Electropolishing times are distinguished by colors; black: 2 min, red: 5 min, green:10 min and blue: 15 min. Current densities are differentiated by shapes; 5 A/dm^2: filled squared, 10 A/dm^2: empty square, 15 A/dm^2: empty square with a x inside, 20 A/dm^2: filled circle and 25 A/dm^2: empty circle.

Even though an aluminum alloy was used, with iron contents between 0.4-0.8%, increasing the probability to generate second phases, different dissolution rates and iron rich precipitates, high reflectance percentages were achieved using the acid electrolyte with chromium. It can be also said that current densities around 10 A/dm^2

for 10 min were found to be the best conditions to electropolish the AA 8005 using the E1 acid electrolyte.

From this point on, AA 1100 and Al 5N alloys are going to be the substrates studied and the chromium free acid electrolyte will be simply named as acid electrolyte.

In order to better understand the electropolishing behavior for each electrolyte the current density vs applied potential curves were obtained (see Figure 1.2a). For these electropolishing plots it was common to observe three zones; the first one was the etching zone characterized for an increase in current due to the dissolution of existing oxides, once all the natural oxide was removed the oxidation and reduction processes were in equilibrium and the current reaches a plateau, where a better surface quality is normally achieved. Then, a further increase in potential causes the current to rise again, due to gas evolution and pitting of the surface is observed under these conditions. Polishing and brightening processes are attributed to the formation of a viscous layer capable of generate a diffusion limiting phenomena [72]. In Figure 1.2a, the modified Brytal curve exhibited the first two zones described above, with the pitting zone not observed in the range of potentials evaluated here. In this case, the curve showed a large plateau zone at a current density of around 27 A/dm^2 and starting approximately at 3 V, providing a wide range of electropolishing potentials. On the other hand, for the acid electrolyte, the electropolishing zone was not observed, the current density increased continuously with potential and no plateau zone was observed, indicating that an active dissolution process was taking place, where no viscous layer was formed, allowing metallic ions to freely dissolve into the electrolyte.

The literature recommends using a galvanostatic process for the acid electrolyte and a potentiostatic procedure for Brytal [59]. Based on the results obtained from Figure 1.2a, the electropolishing potential was fixed at 3 V for the Brytal process. For this process, the current density vs time curve displayed in Figure 1.2b, shows a nearly constant current density, during the whole experiment, indicating a stable dissolution process.

Nevertheless, in the case of acid electrolyte, as no plateau zone was obtained (see Figure 1.2a), the current density was chosen based on the reflectance responses. It was observed that current densities between 10 A/dm^2 and 20 A/dm^2 promoted a mirror like finish (see Figure 1.3a). The potential vs time curve using 10 A/dm^2 shows that a voltage across the cell of about 8 V was obtained after 200 seconds of electropolishing and it increased very slowly to near 9 V after 900 seconds (see Figure 1.2b).

Calculation of the charge involved for each case under the conditions selected, it is, for the Brytal process a constant voltage of 3 V and for the acid electrolyte a constant

current density of 10 A/dm^2. As in the first case, the charge density employed was about 27 A/dm^2, and therefore the Brytal process requires about 3 times more energy than the acid process. These values are in good agreement with the values reported by Wernik [59], Wood [61] and Buhlert [73] for acid electrolytes being between 15 to 25 A/dm^2, 10 to 15 A/dm^2 and 10 to 30 A/dm^2, respectively. Nonetheless, the reported I-V curves and current density values for alkaline processes were restricted to the general Brytal composition (sodium carbonate 15% and trisodium phosphate 5% wt) and not for its modifications. Then, the obtained 27 A/dm^2 for the modified Brytal seems to be higher than the commonly reported current density responses between 6-8 A/dm^2 obtained at voltages around 8 V [59,61]; this was possibly due to the addition of aluminum sulfate which avoids the characteristic current drop of the standard process as Pinner proposed [74].

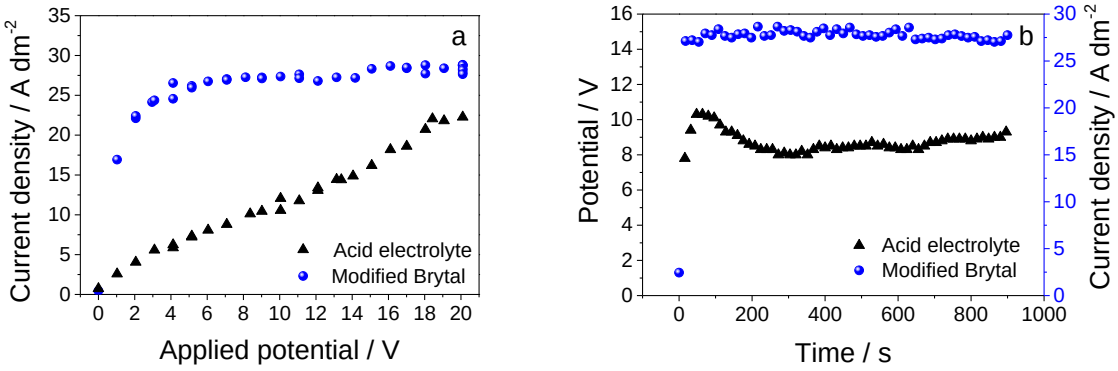

Figure 1.2 a) Current density vs applied potential graph for both acid and modified Brytal electrolytes at 80 °C until 20 V using a scan rate of 1 V/sec with a holding time at each potential of 15 s. b) Current density vs time curve for modified Brytal process at 80 °C, 3 V, 15 min and potential vs time curve for acid electrolyte process at 80 °C, 10 A/dm^2, 15 min.

1.3.1 Effect of electropolishing electrolyte on reflectance

For the acid bath, Figure 1.3a shows the total reflectance curves for various current densities at a fixed electropolishing time of 2 minutes and in Figure 1.3b, it is shown the effect of polishing time on surface reflectance treated at a fixed current density of 10 A/dm^2. As typically observed for aluminum surfaces, the curves in Figure 1.3 exhibited two reflection peaks around 270 nm and 600 nm and a dramatic drop around 200 nm, which is related to light absorption. Current density affects differentially the reflectance in the UV and the visible range of the spectrum; whereas the effect of electropolishing time on surface reflectance was more or less equal in both parts of the spectrum. Higher reflectance percentages were related to current densities between 10 and 15 A/dm^2 and times in the range of 10 to 15 minutes as it

can be easily observed from Figure 1.4. In terms of reflectance and energy consumption, the higher average reflectance was obtained for a current density of 10 A/dm^2 and an electropolishing time of 10 minutes.

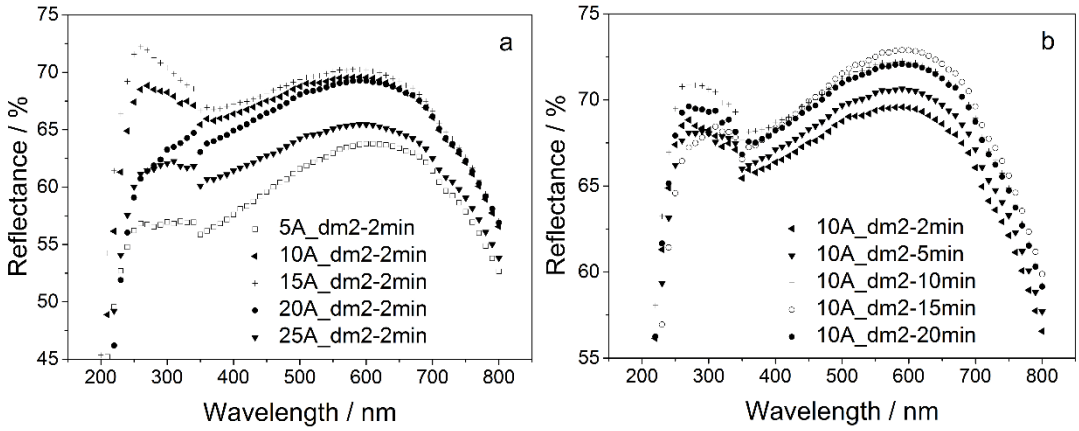

Figure 1.3 Total reflectance curves of AA 1100 no-heat-treated. a) Current density effect at 2 minutes of electropolishing time using acid electrolyte b) Time effect at 10 A/dm^2 as applied current density using the acid electrolyte.

Figure 1.4 shows reflectance percentage variation with current density and electropolishing time at three selected wavelengths: 270 nm, 400 nm and 600 nm. As Figure 1.4a shows, the maximum reflectance percentages observed at 270 and 600 nm are exhibited at electropolishing current densities between 10 and 15 A/dm^2. Nevertheless, at 400 nm and after 10 A/dm^2 as current density increases, reflectance decreases. From Figure 1.4b it can be noticed that maximum reflectance values were displayed at times between 10 and 15 min.

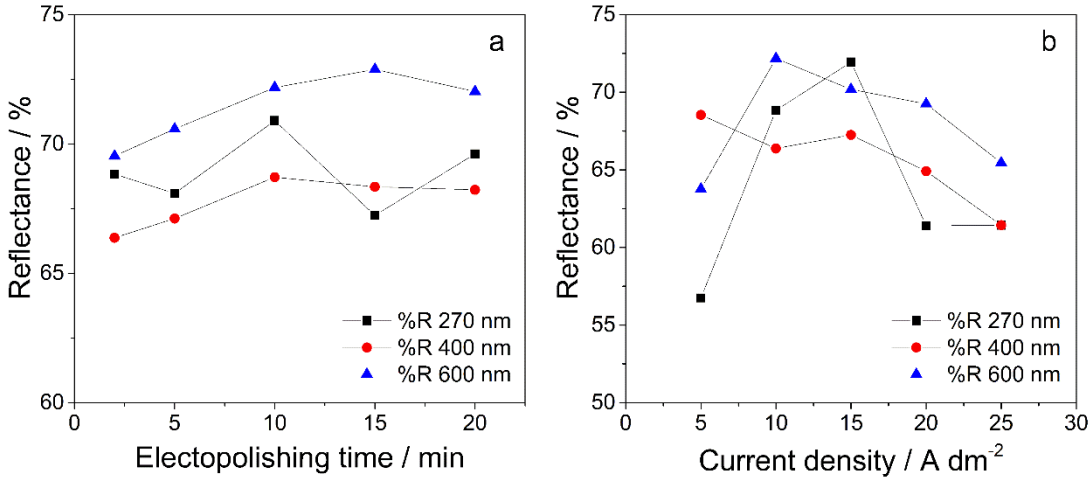

Figure 1.4 Reflectance values at 270 nm, 400 nm and 600 nm of wavelength for samples electropolished in acid solution a) at a constant electropolishing time of 2 minutes b) at a current density of 10 A/dm^2.

The results of reflectance measurements of samples treated with the modified Brytal process are shown in Figure 1.5a. All curves showed similar shapes, with reflectance varying similarly for the two parts of the UV-Vis spectrum regardless the electropolishing time used. The maximum reflectance was obtained between 12 to 13 minutes of polishing; this is easily observed in Figure 1.5b, where total reflectance at different electropolishing times for both 270 nm and 600 nm wavelengths is depicted.

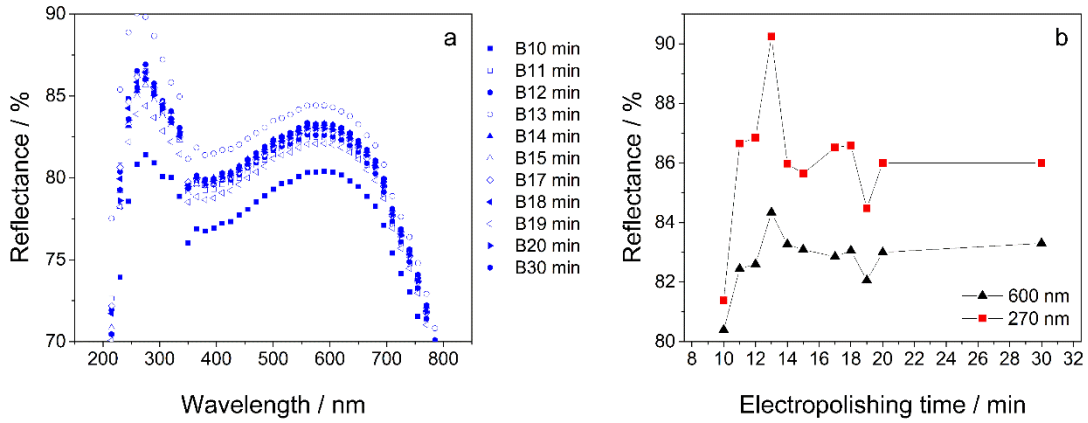

Figure 1.5 a) Total reflectance of AA 1100 heat-treated at 600 °C for 6 hours and electropolished with modified Brytal at 3 V during various times (B: Basic electrolyte) and b) total reflectance at different electropolishing times at 270 nm and 600 nm wavelength.

1.3.2 Determination of the influence of the previous heat treatment on reflectance

Based on the knowledge that the rolling process creates a wave-shaped unidirectional roughness in aluminum sheets, three samples where heat treated at 500 °C during six hours in order to diminish rolling marks, stress concentration and grain alignment. The samples were then electropolished using the above described procedure for the acid electrolyte during 15 minutes in order to evaluate if there is an effect of previous mechanical processes on surface reflectance.

Figure 1.6 shows images of surfaces electropolished in both acid (10 A/dm^2, 15 min) and basic (3 V, 15 min) electrolytes without previous heat treatment. Figure 1.6a shows the non-heat-treated surface of the sample electropolished in acid solution characterized by an oriented scalloped surface, which seems to resemble the rolling direction. The surface texture is better observed in Figure 1.6c where particles detachment was evidenced, this was also reported by Mallinson et al. [75] and Li et al. [76]. Surface of non-heat-treated Brytal electropolished sample exhibited an

aluminum matrix with second-phase particles distributed all around the surface. Figure 1.6d also reveals some detached particles as reported by Lunder et al. [77] and crevice around second-phases in agreement with the results of other works [60,75,78,79]. However, it seems that most of the particles are still attached to the aluminum matrix [65,75]; EDS measurements reveal the presence of iron and silicon as components of these particles.

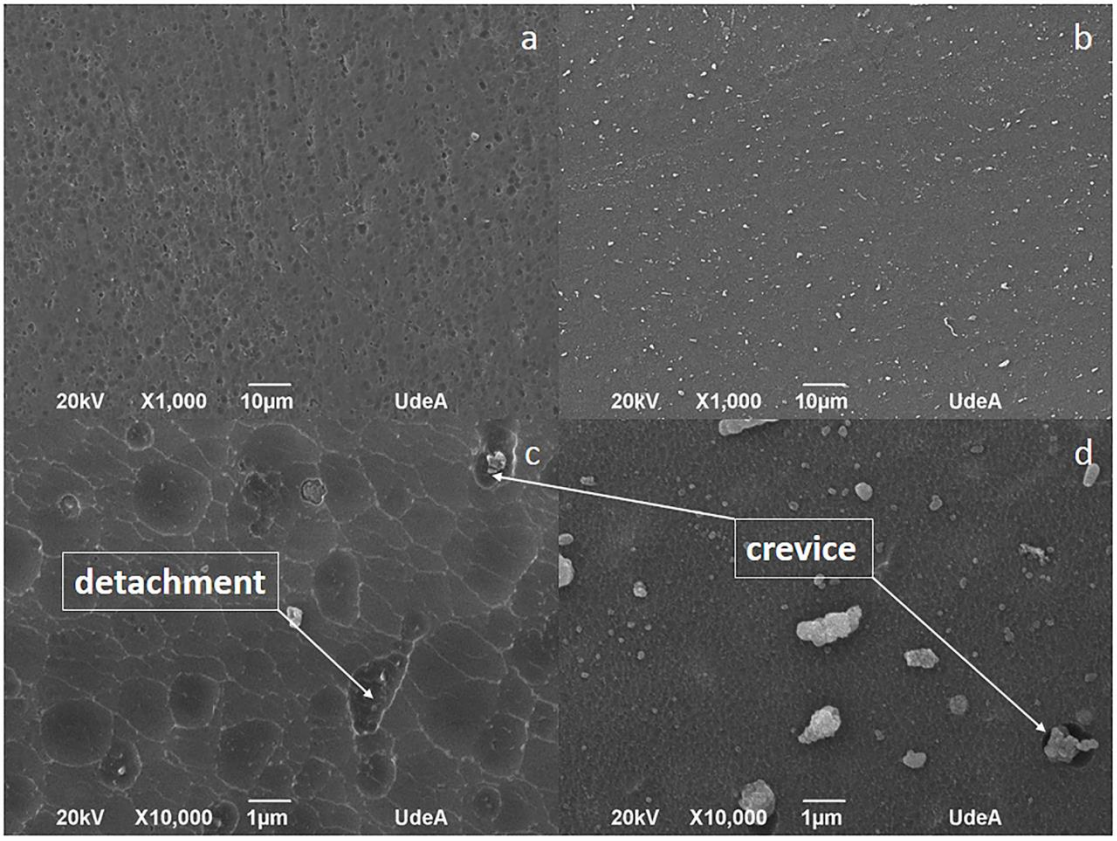

Figure 1.6 Images of the electropolished aluminum surfaces without previous heat treatment using a) acid electrolyte b) modified Brytal c) acid electrolyte showing detached second-phase and crevice around a particle and d) modified Brytal pointing crevice.

In Figure 1.7, results of surface analysis of samples electropolished in the two electrolytes after heat treatment are shown. Figures 1.7a and 1.7b show low magnification optical microscopy images of samples electropolished with the acid and the modified Brytal electrolytes, respectively. Both surfaces presented dark spots, which are both much bigger and higher in density for the sample treated in the acid electrolyte. Figure 1.7c is a zoom-in image of the boundary zone between a dark area and the aluminum matrix pointed in Figure 1.7a. The zoomed image clearly exhibited two zones, the dark cluster is an iron rich zone and the other zone corresponds to an aluminum matrix with dispersed intermetallic compounds mainly

compose by iron and silicon according EDS measurements. Figure 1.7d corresponding to the Brytal surface, shows a homogeneous microstructure of aluminum with dispersed intermetallic particles similar to those observed by [80]. Energy dispersive spectroscopy (EDS) measurements show aluminum, iron and silicon for both Figures 1.7c and 1.7d as it is observed in Figure 1.7h. Meanwhile, Figures 1.7f and 1.7g correspond to aluminum and iron EDS mappings, respectively, carried out in the zone displayed in Figure 1.7e. The analysis revealed the cracked cluster as an iron rich area probably due to the detrimental effect that second-phases show on the corrosion resistance of aluminum. These phases are known for being mostly cathodic to the aluminum matrix, acting as preferential sites for oxygen reduction and hydrogen evolution which induces localized etching generating pitting attack of the surface rather than an even polishing [65,75,76,81–85].

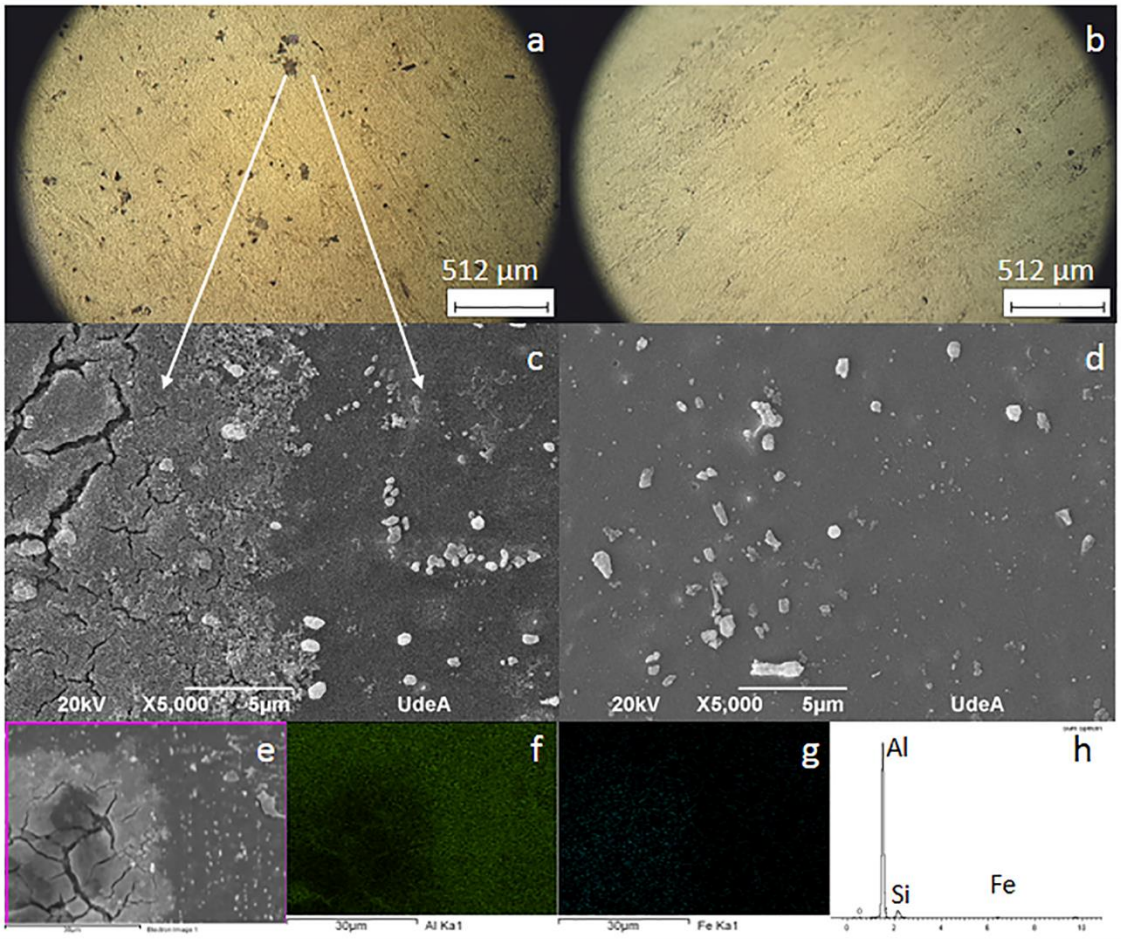

Figure 1.7 Images of the electropolished AA 1100 aluminum surfaces heat-treated at 500 °C a) in acid electrolyte b) in modified Brytal c) in acid electrolyte showing high magnification in the boundary of a cluster d) in modified Brytal showing an aluminum matrix with dispersed second-phase particles e) analyzed zone by EDS element mapping f) Aluminum map g) Iron map and h) EDS spectrum corresponding to image e.

Microstructural and superficial characteristics of the electropolished samples have a direct influence on reflectance response as it can be observed from Figure 1.8 where the reflectance curves of samples electropolished in both acid and modified Brytal electrolytes, with and without previous heat treatment are illustrated. Curves corresponding to non-heat-treated samples for both electrolytes showed reflectance percentages around 70% in the visible range, which were lower than those obtained for the samples previously heat-treated that were around 84%. It can be also noted that despite the reflectance values above 600 nm were similar for the samples electropolished with both electrolytes, towards the UV part of the spectrum, the reflectance values obtained in the sample treated with the alkaline solution were higher than those of the samples processed in the acid electrolyte. This can be explained by the less homogeneous surfaces obtained after treatment in the acid electrolyte, inducing either an scalloped surface in the no heat treated samples or the formation of dark areas in the heat treated ones; the acidic media, was more aggressive at high temperature than the alkaline media [86]. The textured surfaces obtained after electropolishing non-heat-treated aluminum were generated probably due to second-phases acting as stress concentrators [87] making their surroundings more susceptible to dissolution and then leading to particle detachment. Nonetheless, after 500 °C for 6 hours, the stresses around intermetallic compounds were released and no second-phases removal was observed.

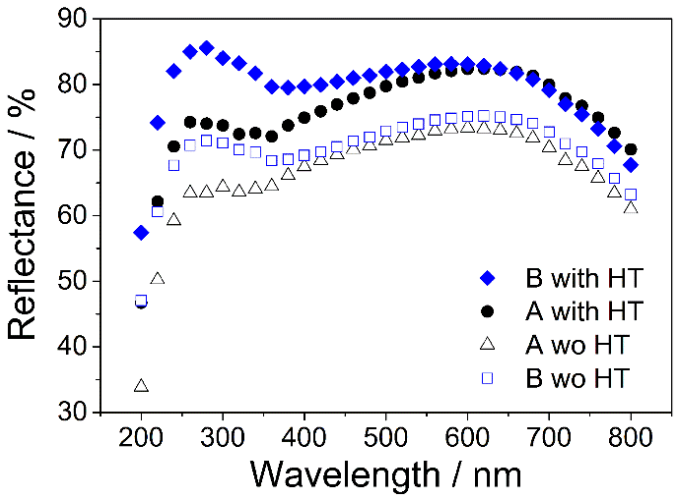

Figure 1.8 Total reflectance curves of AA 1100 samples with and without (wo) previous heat treatment electropolishing in both acid (10 A/dm^2, 15 min) and modified Brytal (3 V, 15 min) electrolytes. A: Acid electrolyte and B: Modified Brytal process.

Knowing that the increase of surface roughness is an important characteristic for substrates to be anodized, average surface roughness measurements were done after electropolishing the samples under three different conditions: The acid

electrolyte with previous heat treatment at 500 °C and the alkaline solution with previous heat treatments at 500 °C and 345 °C. Roughness values for the samples electropolished using the modified Brytal process were 176 ± 27 nm for those previously heat-treated at 500 °C and 161 ± 34 nm for those heat-treated at 345 °C. The measured roughness was higher and less homogeneous for the samples polished using the acid electrolyte with previous 500 °C heat treatment, with values around 219 ± 97 nm. The higher roughness values obtained for the acid electropolished samples were related to the observed surface defects showed in Figures 1.7a and 1.7c.

The reflectance spectra showed in Figure 1.8 are in good agreement with microstructural and roughness results, showing higher reflectance percentage in the visible range for samples previously heat-treated and electropolished with the modified Brytal process in comparison with the samples polished with the acid electrolyte.

Grain boundaries and grain orientations generate light diffraction, diminishing the specular component of the reflectance. The as-received aluminum sheet exhibited a structure common for rolled materials with elongated grains aligned in the rolling direction. After heat treatment, recrystallized, equiaxed grains of similar size ($\sim 135\ \mu m$) together with insoluble particles most possibly made of $FeAl_3$ and Fe_3SiAl_{12}, were observed, regardless the heat treatment temperature or holding time, as can be observed in Figure 1.9.

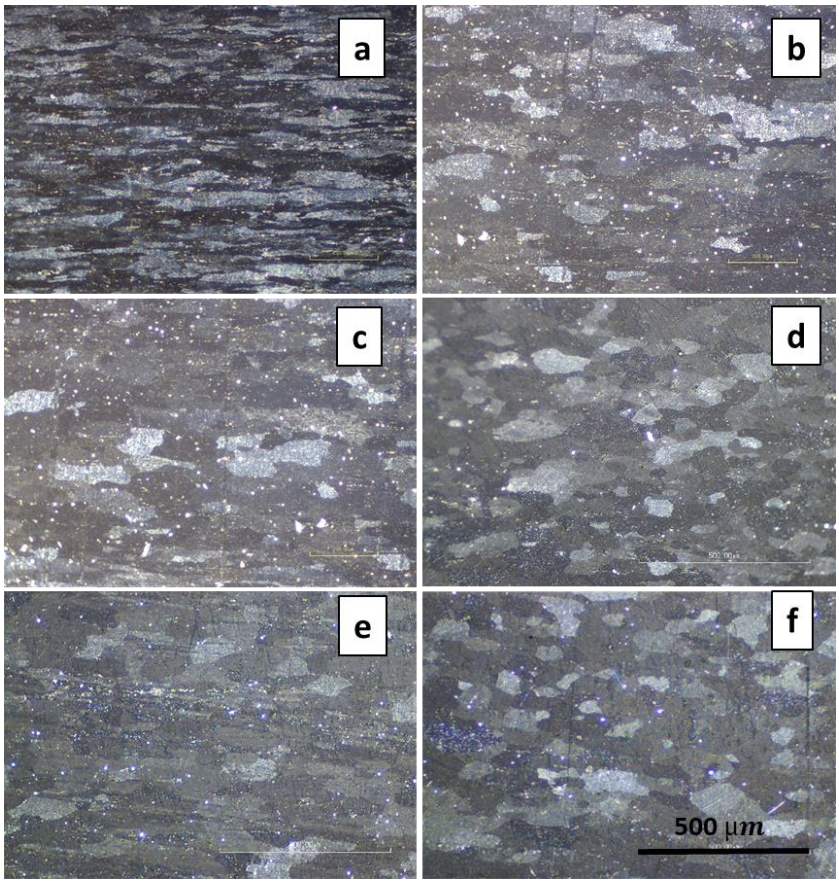

Figure 1.9 Optical microscopy of a transversal section of AA 1100 showing the microstructure evolution of aluminum with different heat treatments a) before (as delivered), b) 5 min 345 °C, c) 5 min 500°C, d) 1 h 500°C, e) 7,5 h 500°C f) 14 h 500°C.

Figure 1.10 shows reflectance curves for AA 1100 samples with different heat treatments and the pure aluminum previously heat-treated at 500 °C for 5 min electropolished with the modified Brytal electrolyte. These results reveal a clear increase in reflectance percentage of around 15% for heat-treated samples with respect to the untreated ones. It also can be noted that heat treatments either at lower temperature or with shorter holding times lead to higher reflectance of the aluminum surfaces after electropolishing. A possible explanation to this effect is as follows: The heat-treatment at 345 °C was enough to release the stresses in the samples and to recover the grains shape; however, higher temperatures and/or longer holding times might lead to increase the number of second phase particles per unit area mainly at the surface [60,64,65]. The amount of light scattered and absorbed by the surface is directly related to the number and size of those second-phase particles. Then, samples with more intermetallic compounds in the surface lead to light loses by scattered rays and consequently lower reflectance

percentages. It can be observed the effect of the alloy components and consequently of second-phases, in the reflective response of the aluminum when the Al 5N sample, free of second phases, was electropolished under the same conditions revealing higher reflectance percentages in the evaluated wavelengths, mainly in the UV zone.

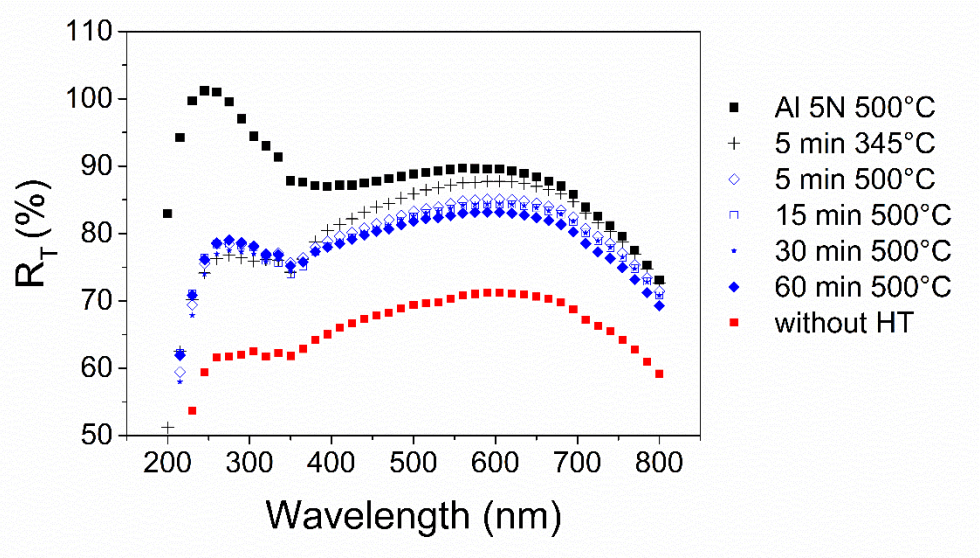

Figure 1.10 Total reflectance curves of AA 1100 samples with different heat treatments (HT) and electropolished using modified Brytal procedure. The filled black square corresponds to the reflectance spectrum of the pure aluminum previously heat-treated at 500 °C for 5 min.

The main aim of electropolishing the aluminum surface was to create a flat and smooth surface prone to be anodized and generate large grains to diminish the number of grain boundaries that limits the NAA domain sizes, producing in that way a prone surface to grow self-ordered NAA structures. The effect of HT was evaluated from transversal images to obtain a real bulk information of the metallurgical changes of AA 1100 and the generated grain sizes were similar. Then, an additional top observation was performed in pure aluminum samples to obtain more information about the surface grain size, which will have a direct effect on nanoporous anodic alumina domain sizes. Figure 1.11 shows top images of pure aluminum heat treated at 375 °C and 500 °C for 5 min. In average, the superficial grain size was similar, 170 ± 94 µm for 375 °C and 164 ± 62 for 500 °C. Nevertheless, a major amount of larger grains can be observed for the 500 °C, result that agrees with a lower standard deviation related to the 375 °C sample. It is common to find larger grains on metals surfaces than in their inner part due to heat distribution. Additionally, if the HT is an annealing process, the deformation and stresses concentration are higher at the surface than at the inside of the metal; those highly distorted microstructures are in a high-energy state and are thermodynamically unstable. When heat is applied, the

thermal activation energy needed to transform the material to a lower-energy state is provided. Then, in a stress concentrated area the grain growth stage is reached faster than in a less distorted zone [67]. It is also important to consider that the samples evaluated in Figure 1.9 were AA 1100 with reported grain sizes around 135 µm whilst those in Figure 1.11 were pure aluminum. During grain growth, the process of boundary migration can be delayed by dissolved iron atoms which explains the larger grains for pure aluminum compared to the aluminum alloy [88].

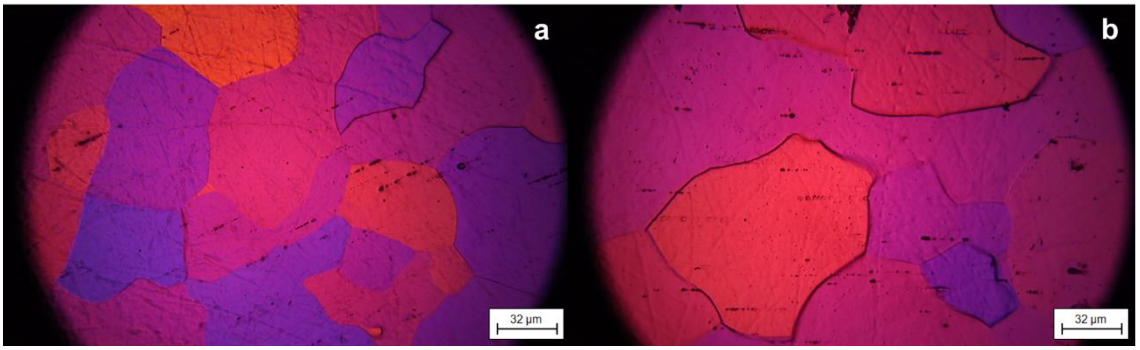

Figure 1.11 Optical microscopy of a transversal section showing the microstructure evolution of Al 5N aluminum previously heat-treated a) at 375 °C for 5 min and b) at 500 °C for 5 min

Since the Al 5N was 99.999% pure, the possibility to form second phases was negligible and the detrimental effects of using higher temperatures are discarded. Consequently, the 500 °C heat treatment was selected as pretreatment for anodizing due to the achieved low roughness, high reflectance and mainly due to the major amount of larger grains observed on the aluminum surface compared to the 375 °C heat treatment. Thus, generating an ideal surface to grow self-ordered nanoporous anodic alumina.

1.4 Conclusions

Three electropolishing electrolytes were successfully used in order to obtain highly reflective aluminum alloy surfaces and according to these results it is recommended replace the use of chromium containing electrolytes for chromium free solutions as the E2.

Despite the modified Brytal process generated higher reflectance in the aluminum surfaces than the acid solution E2, the basic process involves about three times more energy consumption than the acid one.

Second-phases caused uneven dissolution process in the acid electrolyte generating a scalloped surface for the non-heat-treated samples and superficial localized iron-rich defects in the heat-treated ones. These surface defects rise light scattering and therefore reduces the total reflectance of the aluminum alloy surface.

The effect of a previous heat treatment on surface reflectance was clearly observed. A short and low temperature heat treatment (i.e. at 345 °C during 5 min) is enough to release stresses and to eliminate rolling marks. Larger times or higher temperatures increase precipitation of second phase particles at the surface, resulting in light scattering and consequently diminishing total reflectance of the surface.

The AA 1100, properly electropolished using the modified Brytal electrolyte with a previous heat treatment, is suitable as a surface pretreatment for solar anodizing applications.

Pure aluminum (5N) could be correctly electropolished with any of the three evaluated electrolytes and any of the evaluated heat treatments using the proper conditions due to the lack of second phases.

2. INFLUENCE OF ANODIZING PARAMETERS ON MORPHOLOGICAL CHARACTERISTICS OF NAA

2.1 Introduction

Nanoporous anodic alumina (NAA) has become one of the most popular templates to produce various nano-structures such as magnetic, electronic, and optoelectronic devices [89–91]. Moreover, NAA itself is an adaptable platform for various purposes: to obtain chemical and optical sensors [92], biomedical applications [93,94], energy storage [95], photonic crystals [96] catalysis [97,98], Bragg reflectors [99], drug release systems [100], among others. The NAA is characterized by a honey comb structure with a close packed array of pores inscribed in columnar hexagonal cells [101–103]. Nonetheless, the most commonly obtained structures are not that organized, exhibiting polygonal cells of inhomogeneous sizes. Masuda and Fukuda [104] firstly proposed the two anodizing process to obtain highly organized NAA. During the first anodizing step the pores nucleate at random places and when the steady state was reached, the ordering of the NAA cell arrangement starts. In this way, the upper part of the pores was disordered, and the pore bottom was ordered. After conducting the first anodization, the NAA is removed, leaving an aluminum template on the surface. This templated structure serves as pore nucleation sites during the second anodization, making the NAA to grow in an organized way. Afterwards, Masuda and co-workers have stablished that there is a self-ordering regime which applies for each type of acid electrolyte [101,104,105]. The need of a completely flat surface in order to obtain highly ordered structures was claimed by Jessensky, O, et al. [106]. Nielsch, K. et al. [107] proposed the 10% porosity rule to obtain self-ordered pores independent of the specific anodization conditions. Nonetheless, porosity percentages different than 10 have been reported for self-ordered structures [108–110]. Ono et al. [41,110] found that a high electric field strength is the key controlling factor of self-ordering so a highly organized pore structure is achievable by choosing an adequate electrolyte and the appropriate formation voltage for maintaining a high current condition. Later, other researchers have fabricated highly ordered NAA structures by hard anodization process [111,112] or pulsed anodization process [52].

It is well known that morphological characteristics of NAA such as pore diameter, interpore distance, chemical composition and thickness are dependent on the anodizing conditions such as potential, time, temperature, current density, type of electrolyte and pH solution [52,59,102,113–115]. The applied potential mainly affects the interpore distance and pore diameter, the anodizing time of the second step mostly affects the NAA thickness and the temperature is directly related to NAA growth rate [113,116].

Since an efficient control of both size and ordering of the nanostructures is important in practical applications, a deep understanding of the NAA structures is required. A

Fast Fourier Transform (FFT) is commonly used to study periodic, self-organized structures, like nanoporous arrays. There have been proposed several ways to conduct the ordering studies, but they are mainly differentiated by the ordering level of the analyzed structure. Highly ordered structures plot profiles cross the dots presented in the ordered images and defined the regularity ratio as the relationship of the maximum intensity to the width of the peak at half-maximum [108,117,118]. Others observed that the number of pores have an influence on the regularity ratio values and proposed that to remove this effect, a value of the regularity ratio should be divided by the number of pores [119,120]. Some authors went further, they claimed that though the FFT-based regularity ratio has many advantages, the common approach has one major disadvantage, namely it takes into consideration only three major directions of the FFT, which are additionally manually selected. Then, they proposed that the plotted profiles should come from the FFT radial average, taking all the directions into the estimations [121,122]. Another analysis [123] revealed that the intensity and width at half height of FFT radial average were strongly influenced by surface area and number of pores [123–125]. Consequently, proposed that regularity ratio must be calculated with this expression:

$$RR^* = \frac{H}{W_{1/2}} \frac{\sqrt{n}}{S^{3/2}}$$

Where *H* is the intensity of the radial average, $W_{1/2}$ is the width of the radial average at half of its height, *n* is the number of pores on the analyzed image and *S* is the analyzed surface area.

The purpose of this chapter is to fully understand the effect of anodizing conditions by experimentation in order to control the morphological characteristics of the produced NAA. The effect of anodizing potential was evaluated in samples produced from an AA 1100 and from pure aluminum foils (Al 5N). The effect of potential and temperature on NAA ordering was determined by calculating the regularity ratio from the FFT images. The effect of the second anodization time on NAA thickness was determined as well.

2.2 Experimental procedure

An aluminum alloy AA 1100 and high purity aluminum foil (99.999% from Metalmen) were used as substrates for anodization. Prior to anodizing, the substrates were annealed at 500 °C for five minutes and then electropolished with the modified Brytal process specified in Chapter 1.

AA 1100 samples were anodized in 0.3 M oxalic acid electrolyte at a constant potential (between 40 and 75 V) for six hours. The temperature was not monitored or controlled during the process. Then, the aluminum oxide was removed in a mixture of phosphoric acid (H_3PO_4) 6.0 wt% and chromic acid (H_2CrO_7) 4.8 wt% at 60 ºC. As it is well known, the oxide removal after the first anodization step is performed in order to reveal the texturized structure created during the first anodization. Then, after the oxide removal step, texturized aluminum samples were obtained. To observe the influence of anodizing potential on morphological characteristics of the created templates, after the oxide removal the samples were studied by means of scanning electron microscopy (SEM).

Based on the morphological observations of the anodized AA 1100 samples, pure aluminum (Al 5N) samples were anodized at two potentials that generated ordered structures (40 V and 55 V) and at a potential that generated poorly organized arrangement (80 V). To determine the effect of temperature on the ordering of the texturized aluminum, two anodization temperatures were evaluated (5°C and 22°C). The ordering level was determined by calculating the regularity ratio (RR) defined as the ratio of the maximum intensity H_{max} to its full width at half-maximum (FWHM) $W_{1/2}$. RR was calculated by using the radial average profile from the Fast Fourier Transform (FFT) of the top SEM images.

Afterwards, the Al 5N was anodized using the two step anodization procedure [104] in 0.3 M oxalic acid electrolyte at 5 °C. The first anodization time was conducted for 6 h and the oxide removal was performed in the phosphoric and oxalic acids mixture at 60 °C. The oxide removal time and the second anodization time are listed in Table 2.1. Nanoporous anodic aluminum (NAA) thicknesses were determined by optical microscopy (OM) and SEM, results are also shown in Table 2.1. A rigorous characterization was performed to relate morphological features of the fabricated nanoporous anodic aluminum (NAA) with the applied potential. The ImageJ 1.51j8 [126] software was employed for estimation of pore diameter (d_p), interpore distance (d_{int}), porosity (%p) and number of pores (n) from top SEM images. A quantitative arrangement analysis of the pores ordering was done by calculating the average regularity ratio (RR*); in this case, the regularity ratio calculations included the effect of image size and number of pores as proposed in [123]. Fast Fourier Transforms (FFT) of the top SEM images were generated and analyzed with WSxM 5.0 software [127].

Table 2.1. Anodizing conditions used for the Al 5N substrate and corresponding measured thicknesses.

Potential (V)	Oxide removal time (min)	2nd anodizing time (min)	Thickness (μm)
40	40	78	3.7 ± 0.6
40	40	100	5.9 ± 0.8
40	40	120	5.5 ± 1.0
40	40	200	9.4 ± 0.6
40	40	300	14.2 ± 0.8
50	50	105	8.9 ± 0.5
55	55	80	9.2 ± 0.8
60	70	65	8.6 ± 0.7
75	75	15	8.6 ± 0.5

2.3 Results and discussion

2.3.1 Effect of anodizing potential on texturized AA 1100 morphology.

The effect of anodizing potential in AA 1100 texturization is observed in Figure 2.1. The evaluated potentials generated hexagonal cells randomly distributed in the sample, without domains. It can be noticed from Figure 2.1 the cell size (interpore distance) increases with anodizing potential. It is also observed that the sample anodized at 40 V (Figure 2.1a) appears to have more homogeneous cell sizes (hexagon with equal sides) than the other samples. In Figure 2.5 the influence of anodizing potential in texturized AA 1100 interpore distance (d_{int}) is observed from the blue stars in the graph. From Figure 2.5 it can be said that, statistically, all evaluated potentials generated similar interpore distances due to the overlapping of the standard deviations depicted as error bars. The measured interpore distances of samples anodized at 40 V and 75 V are statistically different, the higher the potential the larger the pore. The standard deviation bars were shorter for the samples anodized at 40 V than for the other anodizing conditions, supporting the homogeneous cell size observations from Figure 2.1a. The cell size distribution was less homogeneous for 45 V and 75 V samples, observed from larger standard deviations bars. The sample obtained at 75 V exhibited inhomogeneous cell sizes ranging from 76 nm to 200 nm.

The poorly organized structures generated after anodizing the AA 1100 can be related to roughness (~176 nm); it was studied in Chapter 1. Iron (Fe) and silicon (Si) are the main alloying elements of AA 1100, these elements are not soluble in

the aluminum matrix and form second-phases acting as cathodes for the aluminum matrix generating particle detachment during the electropolishing process, increasing the roughness values. Fratila-Apachitei, L. E. et al. [128,129], observed that that the iron bearing particles present in the aluminum substrate are either inert or undergo oxidation at a lower rate compared to the adjacent aluminum matrix as also observed in [130]. For insoluble particles composed by Al-Fe-Si, it was observed that an increasing volume fraction of particles were occluded into the aluminum oxide with anodizing potential [129]. The above findings indicate that the quality of anodic oxide layers formed on the pure aluminum substrate under the specified conditions will depend on the amount and distribution of insoluble impurities that have a different behavior relative to the matrix during anodizing. The alloying elements can generate second phases and cathodic spots causing inhomogeneities on the aluminum surface, these defects contribute to the poorly organized structures formed during anodization.

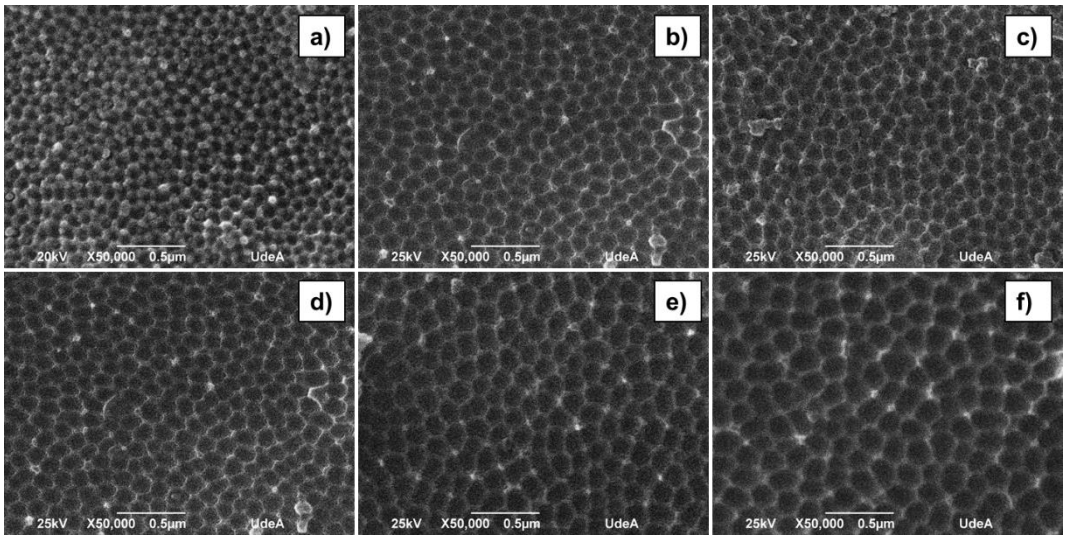

Figure 2.1 SEM micrographs of AA 1100 samples after anodization in oxalic acid and oxide removal in phosphoric and chromic acids. a) 40 V, b) 45 V, c) 50 V, d) 55 V, e) 60 V and f) 75 V. The anodization was carried out without temperature control.

2.3.2 Effect of anodizing temperature on texturized Al 5N morphology.

In Figure 2.2 the effect of anodizing temperature on ordering of samples anodized at 40 V, 55 V and 80 V at 5 °C and 22 °C is shown. On the left, top SEM micrographs of texturized Al 5N samples (after anodization in oxalic acid and oxide removal), images in the middle are their respective FFT, the plots on the right column represent the radial average profiles obtained from the FFT images. Figures 2.2a, b and c are the samples anodized at 5 °C and Figures 2.2a', b' and c' correspond to the samples

anodized at 22 °C. From visual inspection it can be said that the evaluated potentials produced hexagonal arrangements in most cases. It is also observed that ordering level decreases with the increase of anodizing potential. Samples anodized at 40 V and 55 V exhibit higher ordering of the structure, characterized by groups of cells forming domains. The FFT images present a bright ring that decreases in size with anodizing potential. The observed ring becomes blurred or diffuse with the increase of the anodizing potential. From the FFT image of Figure 2.2a, it can be observed that there are two concentric bright rings and that six bright spots (forming a hexagonal structure) are inscribed into the first ring. The bright spots are also seen in Figure 2.2b, corresponding to the sample anodized at 5 °C and 55 V.

The FFT of an image provides a lot information of its ordering level. Highly organized structures are characterized by bright spots located depending on the structure that is repeated in the analyzed image, in this case, hexagons. Poorly organized samples exhibit blurred FFT and semi-organized structures show a ring or several rings depending if the ordering is short or large range. The FFT of the analyzed samples reinforce the bare eye observations of the SEM images. The first ring diameter diminishes with anodizing potential probing that the cell size increases with potential as observed from Figure 2.2 and detected for the AA 1100 analysis of Figure 2.1. The spots observed in the FFT of Figure 2.2a and b indicate that the repeated structure is organized in a hexagonal lattice and the second ring exhibited only by Figure 2.2a is due to the long-range ordering level of the sample anodized at 5 °C and 40 V. The rings become blurred with increasing potential showing that ordering decreases with potential. The vertical bright line is not related to the ordering of the structure, it is an artifact generated by the horizontal white mark in the lower part of the images, containing the image magnification and size. From the regularity ratio values in the right part of each radial average graph of Figure 2.2, it can be said that samples anodized at lower temperatures exhibit more organized structures grouped in domains. Increasing the anodizing potential and increasing the temperature of the anodization generates poorly organized structures. Samples obtained at 40 V and 55 V at 5 °C present highly organized domains as reported by other authors [37,104].

There is an exponential relationship between temperature and current density, then the pore growth rate is increased with temperature and in some cases it was reported that high anodizing temperatures generated highly ordered structures [113]. Nonetheless, other researchers have compared samples anodized at temperatures ranging from 0 °C to 25 °C and concluded that highgly ordered structures were obtained at intermediate temperatures, between 15-17 °C [114]. Others, anodized aluminum in phosphoric acid solution and found that when the temperature is high enough, the strong chemical dissolution makes the surface turn into a “tip bundle” structure without segregated pores, concluding that temperature should be kept under 20 °C to preserve the regular porous structure [131,132].

The evaluated temperatures of this research were 5 °C and 22 °C, showing better ordering results for the lower anodizing temperature. Low pore growth rates are favorable for the process of self-organization [106].

Additionaly, it should be taken into account that temperatures in between the evaluated ones can probably generate more ordered structures (larger domains) than those produced at 5 °C. Increasing the temperature in the first anodization step increases the growth in the longitudinal direction, which in turn increases the self-ordering configuration due the local heating effect for pore growth [114], but increasing the temperature too much, increases local temperature at the bottoms of the pores generating local oxide dissolution [102] and introducing a large thermal stress in the barrier layer and at the metal/oxide interface making the porous structure with less ordering level [133].

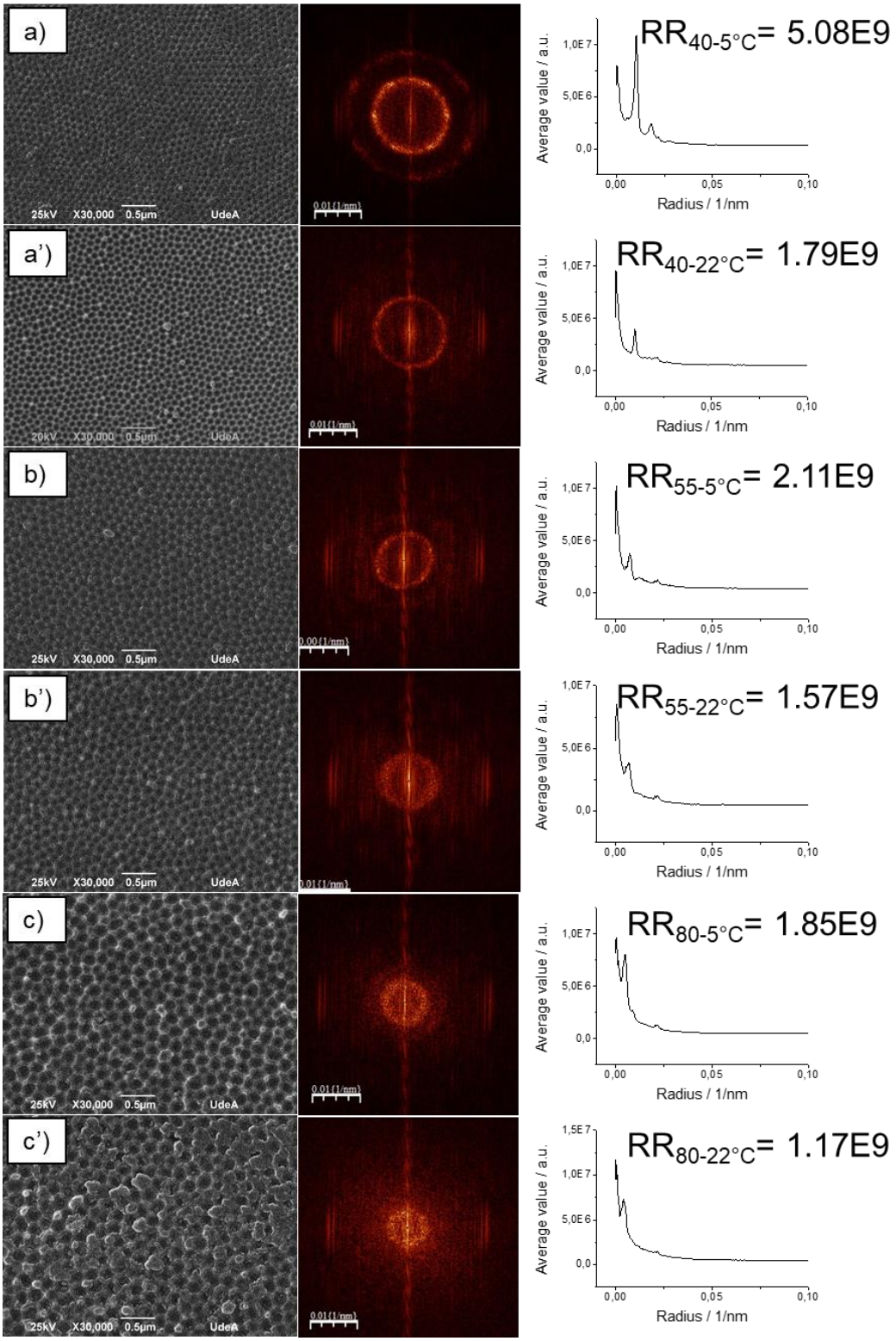

Figure 2.2 SEM micrographs of Al 5N samples after anodization in oxalic acid and oxide removal in phosphoric and chromic acids. a) 40 V: 22°C, a') 40 V: 5°C, b) 55 V: 22°C, b') 55 V: 5°C, c) 80 V: 22°C, and c') 80 V: 5°C.

2.3.3 Effect of anodizing potential on NAA ordering.

In Figure 2.3 the effect of anodizing potential on ordering of Al 5N samples anodized at 5 °C is shown. On the left, top SEM micrographs of nanoporous anodic alumina (NAA) obtained in oxalic acid at 40 V, 50 V, 55 V, 60 V and 75 V, images in the middle are their respective FFT, the plots on the right column represent the radial average profiles obtained from the FFT images and include the radial average with the correction parameters. The obtained structures appear to be highly organized with the characteristic hexagonal pore arrangement of self-ordered NAA, except for the 75 V sample. The first bright ring observed for all potentials decreases in size with anodizing potential. The FFT of samples anodized at 40 V and 50 V (Figure 2.3a and b) exhibit six bright spots inscribed in the first ring showing the hexagonal lattice of the analyzed structure. The FFT image of the sample anodized at 55 V (0 2.3c) shows eighteen bright spots inscribed in the first ring. The FFT corresponding to sample anodized at 60 V has a bight ring with a diffuse hexagonal halo and the 75 V sample FFT has a bright blurred ring.

The size of the first bright ring is related to the size of the analyzed structure. As the first ring diameter decreases with anodizing potential, it can be said that the pore diameter increases with anodizing potential. The number of bright spots determines the lattice arrangement of the analyzed structure, being hexagonal for samples produced at 40 V and 50 V characterized by the six-fold coordinated by neighboring pores. The number of bright spots observed for the 55 V sample is due to the three six-fold symmetry patterns which are related to the presence of three domains [114]. The bright ring with some (apparently four) spots surrounded by the blurred halo with the hexagonal shape observed in the FFT of the 60 V sample is related to the low ordering level of the hexagonal pore arrangement. The FFT image corresponding to the sample anodized at 75 V has the shorter ring diameter and the more blurred appearance accounting for the larger pore diameter and the less organized structure. Other authors observed similar changes in the FFT images for anodizations conducted between 40 V and 60 V at 40 °C [134] and at 20 °C [135]. The calculated regularity ratios are in agreement with the apperance observations of the FFT images and SEM samples, the lower the anodizing potential the higher the regularity ratio as reported previously [120,136]. It shoud be considered that this states only for the evaluated anodizing potential range (40 V to 75 V). Previous results are comparable for the 4.45 RR* value reported for samples anodized in oxalic acid at 20 °C and 40 V and also agrees wth the tendency reported in the same work that RR* decreases with the increase of anodizing potential between 50 and 65 V. Probably the lower RR* values reported for higher anodizing potentials (from 2.98 to 2.13) are related to the higher anodizing temperature used in that work [120]. Other authors anodized aluminum at temperatures between 35 and 50 °C for diferent times

from 30 min to 120 mn and have found that 40 V samples always ehibited higher RR* than 50 V samples but the values oscillate between 2.1-7.5 for 40 v and 1.5-4.5 for 50 V [121].

Figure 2.4a presents the effect of anodizing temperature on regularity ratio and Figure 2.4b shows the effect anodizing potential on RR. It should be considered thar RR corresponds to the values calculated from classic regularity ratio without correcting factors and RR* includes the corrections made by surface area and number of pores proposed in [123]. From Figures 2.2, 2.3 and 2.4 it can be said that temperature influences nanopore ordering but anodizing voltage is the major factor influencing the nanopore arrangement [137]. Low anodizing temperatures and lower potentials produce more organized structures for the evaluated values.

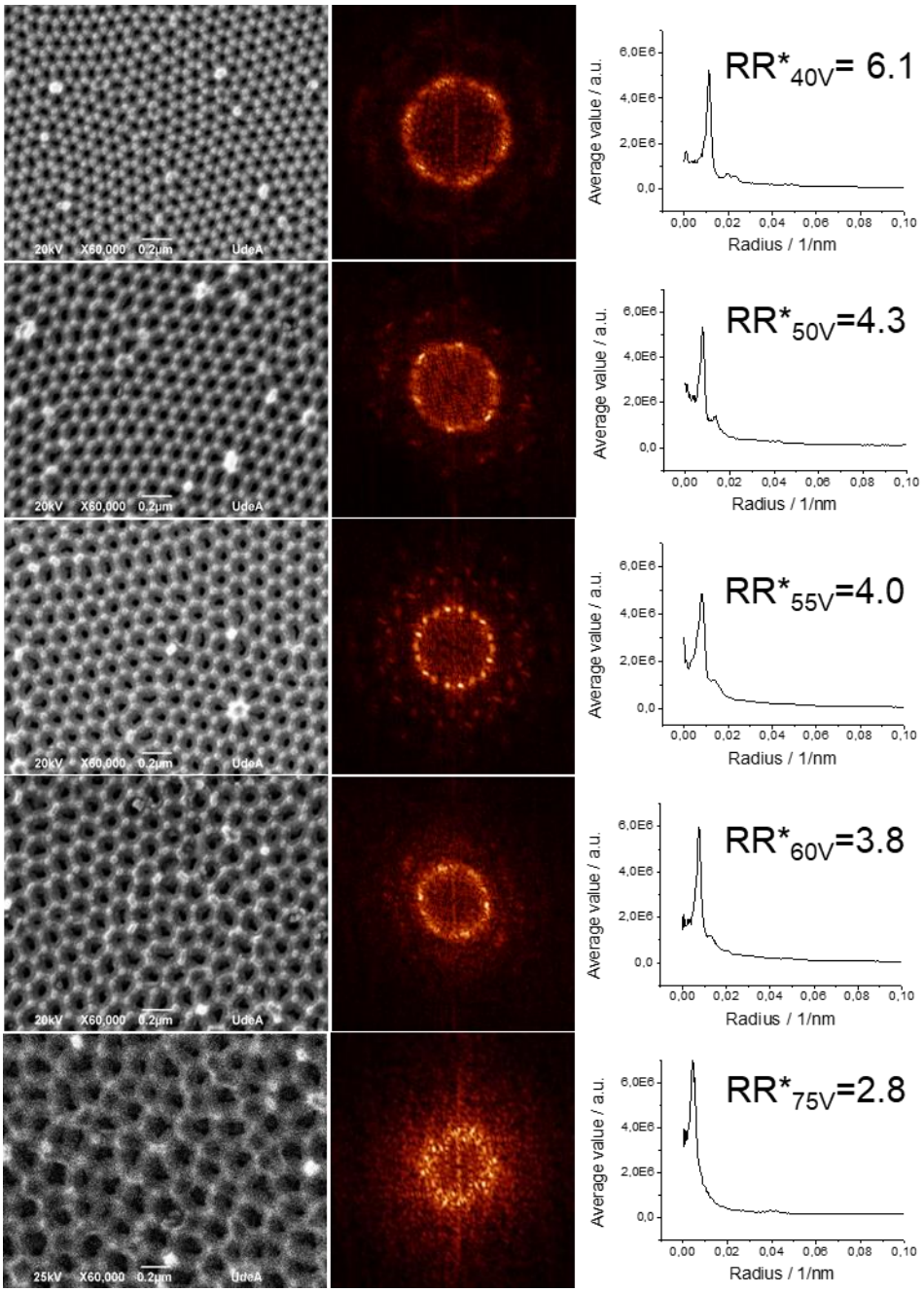

Figure 2.3. Top SEM images with 2D Fast Fourier Transforms (FFTs) and average profile of the FFT pattern radius for porous alumina formed in 0.3 M oxalic acid Al 5N at different anodizing potentials and 5 °C. The analyzed surface area was 3.48 μm^2.

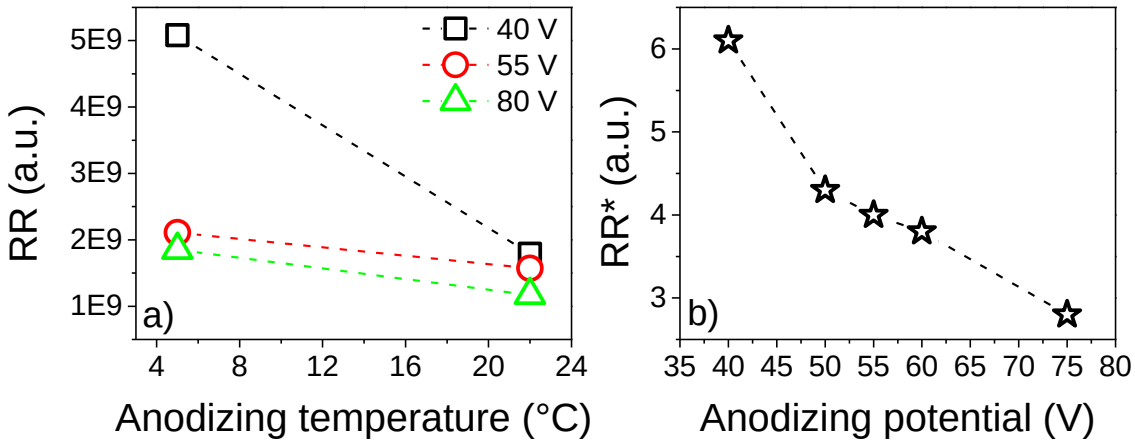

Figure 2.4. Effect of anodizing paramenters on regularity ratio (RR) of the texturized aluminum and NAA. a) effect of anodizing temperature on RR and b) effecto of anodizing potential on RR. RR does not include correction factors and RR* includes the corrections made by surface area and number of pores.

2.3.4 Effect of anodizing potential and second anodization time on morphological features of texturized AA 1100 and NAA produced from Al 5N.

Figure 2.5 shows the morphological characteristics of NAA obtained in 0.3 M oxalic acid. Figure 2.5a shows the effect of anodizing potential on pore diameter (d_p) of NAA obtained in Al 5N and interpore distance (d_{int}) of texturized AA 1100 and anodized Al 5N samples. Figure 2.5b exhibits the effect of second anodizing time on thickness of NAA samples obtained from anodizing Al 5N substrates. From Figure 2.5a, it is observed a clear tendency to increase both d_p and d_{int} with anodizing potential. It is also seen that samples anodized at 40 V produce the shortest error bars and samples obtained at 75 V generated the largest error bars. The blue stars in Figure 2.5 which correspond to the texturized AA 1100 cell diameters, are close to the values observed for the Al 5N sample (red circles), the error bars overlap for the evaluated potentials. The variations in d_p represented by the error bars sizes, increase with anodizing potential. Samples anodized from 40 V to 55 V show similar average values for d_p and d_{int}. From Figure 2.5b, it can be observed that thickness increases with the second anodizing time.

The size of the error bars is related to the homogeneity of the samples, in consequence, the samples obtained from both the AA 1100 and Al 5N substrates at 40 V are very homogeneous in d_p and d_{int}. These results are in agreement with the

self-ordering regime previously reported for samples anodized in oxalic acid [104,106]. The AA 1100 sample anodized at 45 V exhibited large error bars probably due to observation of a substrate zone rich in precipitates or with the presence of crevice that could generate defects in the surface and induce disorder during the first anodization step. The 75 V sample is far from the self-ordering potential as confirmed by the inhomogeneous and poorly organized structure. For the evaluated NAA it was found that the d_p, d_{int} and barrier layer thickness increase linearly with anodizing potential. Results that agrees with the measurements carried out by other authors, where the proportionality constants for NAA formed by mild anodization (MA) processes were reported as d_{int}: 2.5 nm V^{-1}, d_p: 1.29 nm V^{-1} and barrier layer thickness: 1.2 nm V^{-1} [138,139].

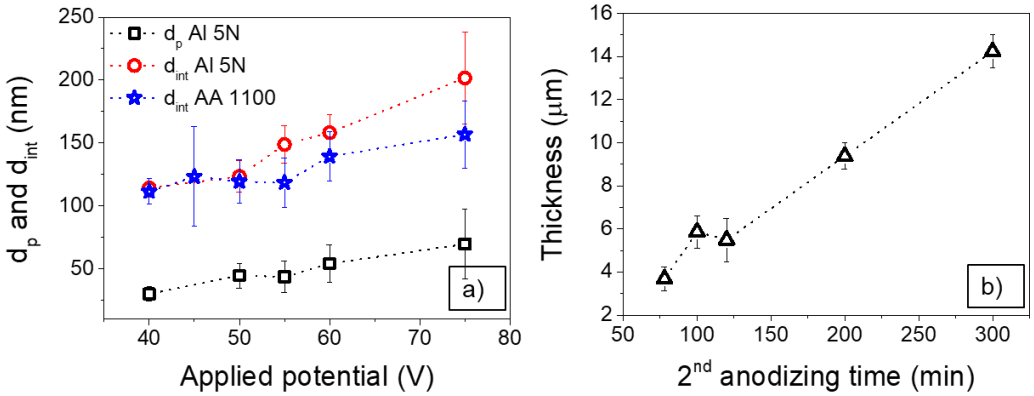

Figure 2.5 Morphological characteristics of NAA obtained in 0.3 m oxalic acid. a) Effect of anodizing potential on pore diameter (d_p) of NAA obtained in Al 5N (black squares) and interpore distance ($d_{int} = d_{cell}$) of texturized AA 1100 (blue stars) and anodized Al 5N (red circles) samples, b) effect of second anodizing time on thickness of NAA samples obtained from Al 5N substrates (black triangles).

2.4 Conclusions

In this chapter the effect of anodizing potential, anodizing temperature and anodizing time on texturized AA 1100, Al 5N and NAA was evaluated. Fast Fourier Transform was used as a tool to quantitatively analyze the effect of evaluated conditions on the ordering of produced structures.

Homogeneous cell sizes can be formed by anodizing AA 1100 in 0.3 M oxalic acid solution. Nonetheless, the alloying elements create defects at the aluminum surface decreasing dramatically the ordering for anodizing potentials out of the 40 V self-

ordering regime. The presence of alloying elements does not affect the interpore distance obtained for determined potential with AA 1100 and Al 5N alloys.

Lower anodizing temperatures induced low current densities and low pore growth rates that are favorable for the self-ordering process. Anodizing temperature affect domain sizes but does not affect the cell size.

Highly ordered structures can be obtained by anodizing pure aluminum in 0.3 M oxalic acid at 40 V, 50 V and 55 V but considering that when the potential increases the regularity ratio decreases.

Pore diameter and interpore distance increase with anodizing potential. Thickness increases linearly with second anodization time.

3. INFLUENCE OF PORE DIAMETER AND THICKNESS ON NAA AND NAA/TiO_2 OPTICAL PROPERTIES

3.1 Introduction

Nanoporous anodic alumina (NAA) is obtained by an electrochemical process involving the oxidation of aluminum in acid solution. Highly ordered structures can be formed under adequate anodizing conditions and generally using a template [116,138,140,141]. For instance, Masuda and Fukuda [104] first proposed the two-step anodization process in which the pore bases formed in the first anodization step serve as template and act as initial sites of pore growth in the second anodization step.

Over the last decade, NAA has been extensively used in a diverse range of applications including energy storage [142], drug delivery [100,102,143], sensing [45,54,92,144–151], catalysis [152] and template synthesis [113,153–157]. This increasing interest has been generated by the NAA outstanding characteristics, such as a cost-effective platform, its high aspect ratio, photoluminescence and the remarkable capability of controlling the geometric features by means of varying the anodization potential, time, electrolyte pH and temperature. The potential applications of NAA not only depend on its physical and chemical properties but also on its morphological characteristics. The optical response of NAA is highly influenced by its morphology generating changes in the refractive index, extinction coefficient and photoluminescent properties generating the need of fully understand the effect of anodizing parameters in NAA optical properties [158]. However, highly ordered NAA is restricted by the self-ordering regime [48,104,107,159] which generates specific pore diameter ranges, limiting the varieties of possible morphological modifications. Some researchers have addressed this problem through hard anodization [111,160] or NAA surface modifications obtaining a wider range of pore diameters [161]. The commonly used materials to modify the NAA surface includes, metal oxides such as TiO_2, $PbTiO_3$, SnO_2, SiO_2, metals as gold, silver, nickel, platinum, titanium and polymers like polymethyl metacrylate, polystyrene, polypyrrol, polythetrafluorethylene, nylon, carbon, among others [162]. This nanopore engineering broadens the NAA applications using the unique reflectance or photoluminescence properties of the material to obtain photonic barcodes or nanoporous rugate filters [163].

TiO_2 is a promising material to be used in an extensive field of applications due to its photocatalytic activity and high hydrophilic behavior under illumination together with its high refractive index and wide band gap. Nowadays, TiO_2 is used as optical coating [164–166], photonic crystal [167], in photocatalysis [168–171] and photoelectrochemical solar cells [172]. TiO_2 can be deposited using both physical and chemical methods. The physical methods comprise physical vapor deposition (PVD), sputtering, molecular beam epitaxy (MBE) and laser deposition. The chemical methods include polymerization, sol-gel, spin- and dip-coating, spray pyrolysis and chemical vapor deposition (CVD) [2,94,162,173–179]. Amongst them, spray pyrolysis represents a very simple and relatively cost-effective processing

method to prepare dense and porous films and powders [179]. The spray pyrolysis method uses a spray gun atomization way to turn microsized liquid droplets into solid particles on a heated substrate. This process involves generation of the precursor droplets, evaporation of the solvent, condensation of the solute, decomposition and reaction of the solute and finally the sintering of solid particles [180]. Spray pyrolysis also has the advantage that the heated substrate avoids the heat treatment often needed in TiO_2 to obtain the desired photocatalytic properties conferred by the anatase phase and obtained at temperatures around 500 °C [169,181–183].

Considering the outstanding characteristics of TiO_2 and the need to improve NAA properties to introduce new opportunities for advanced applications in biomedicine, chemistry and biology, in this work, TiO_2 was used as a surface modification of NAA. NAA films were prepared by anodizing aluminum in oxalic acid and Al/NAA/TiO_2 films were obtained afterwards by means of spray pyrolysis process of TiO_2 on top of the NAA surface. The influence of morphological features on the optical behavior of Al/NAA and Al/NAA/TiO_2 was evaluated. Moreover, the experimental results were supported by numerical simulations based on the Transfer Matrix Method [184–186] with an extinction coefficient of zero and by considering the absorption of incorporated oxalate ions and oxygen vacancies. A Bruggeman effective medium approximation (E.M.A) was used to model the porosity of both the NAA film and of the porous sprayed TiO_2 film.

3.2 Experimental procedure

Pure aluminum sheets (99.999% obtained from Metalmen), were annealed at 500°C for 5 minutes and then electropolished in a mixture of trisodium phosphate (150 g/l), aluminum sulfate (20 g/l) and sodium hydroxide (10 g/l) applying 3 V during 15 minutes at 80 °C as previously reported in [187]. The NAA was obtained using the two-step anodization process in oxalic acid 0.3 M at 5 °C and 40 V. The first anodizing step was carried out during 6 h, the formed NAA layers were then removed at 60 °C using a chromic acid 4.8% and phosphoric acid 6% mixture. Then, a second anodization was performed at 40 V and the time of the second anodization was modulated in order to obtain the desired thicknesses. The pore widening process was performed at 35 °C using H_3PO_4 5 % w/w for 10, 20, 30 and 40 min, producing pore diameters between 30 nm and 80 nm.

The titanium dioxide (TiO_2) coating was obtained by means of spray pyrolysis technique. A precursor solution of 0.2 M titanium diisopropoxide bis (acetylacetonate) was used. The Al/NAA substrates were in a hot plate at 500 °C during the spray process as described in [172]. It should be noticed that different samples of Al/NAA were used for each measurement but fabricated under the same

anodizing conditions. The coating thickness was between 87 nm and 438 nm, proportional to the number of TiO_2 deposited layers (1, 2, 4, 8, 16, 32, and 64 layers). The TiO_2 annealing was performed leaving the coated samples during 1 hour on the hot plate.

Total reflectance spectra were obtained by UV/VIS spectroscopy, using a Cary 100 Spectrophotometer with integration sphere with an 8° edge. The specular reflectance measurements were performed in a PerkinElmer Lambda 950 UV/VIS/NIR using the Universal Reflectance Accessory (URA).

The photoluminescence (PL) measurements were taken on a fluorescence spectrophotometer from Photon Technology International Inc. with a Xe lamp used as the excitation light source at room temperature and an excitation wavelength (λ_{ex}) of 360 nm. In some cases, a 400 nm cutoff filter was used.

The standard image-processing package (ImageJ, public domain program developed at the RSB of the NIH, USA) [188] was used to analyze the SEM images.

3.3 Numerical modeling procedure

In order to analyze the measured reflectance spectra, numerical simulation of the reflectance was carried out. The numerical simulations were based on the Transfer Matrix Method [184–186] considering a model composed of an aluminum substrate, a thin film corresponding to the nanoporous aluminum oxide and, in the case of the samples after the TiO_2 spraying, a second thin film on top, corresponding to the porous TiO_2. In the simulation, normally incident light was assumed, and specular reflectance was calculated.

The porosity of both the nanoporous aluminum oxide film and the porous sprayed TiO_2 film was modeled as a mixture of the corresponding oxide and air, using a Bruggeman effective medium approximation (E.M.A.). The E.M.A. considers the refractive index and the volume fraction of each constituent material (oxide and air), being the volume fraction of air equivalent to the porosity. Refractive indices of aluminum, aluminum oxide, and titanium dioxide have been taken from literature [189,190].

Pore radius and porosity were estimated from top-view SEM pictures of the samples according to the equation proposed in [107].

$$p = \frac{2\pi}{\sqrt{3}}\left(\frac{d_p}{d_{int}}\right)^2$$

It must be noted that pore diameter increased with time of application of the pore widening process. The corresponding porosity values are specified in Table 3.1.

Table 3.1 Corresponding porosity values used in the E.M.A model.

t_{PW} (min)	Porosity (%)
0	6.97
10	17.01
20	31.68
30	35.69
40	42.41

One important feature in the calculations is the introduction of absorption in the model for the aluminum oxide. It is well known that, even though aluminum oxide is transparent and the extinction coefficient is zero in the literature referenced tables, porous aluminum oxide obtained by electrochemical etching in acidic solutions exhibits optical absorption and photoluminescence due to the incorporation of conjugate base anions into the oxide matrix, as well as because of the presence of oxygen vacancies [44,191–196]. Furthermore, the concentration of the incorporated anions is not uniform but it decreases from the pore-oxide interface towards the inside of the oxide [42,196–199].

The absorption was considered into the model by assigning nonzero values to the extinction coefficient, which follows a Lorentzian curve as a function of the wavelength. The central wavelength and width of the Lorentzian curve was determined from literature [14,158,193,198,200–203] and specified in Table 3.2. The height of the Lorentzian determines the strength of the absorption. Such strength varies with the time of application of the pore widening process. Heights for the Lorentzian used in the simulations are also detailed in Table 3.2.

Table 3.2 Lorentzian values used to create an absorbing extinction coefficient.

t_{PW} (min)	Lorentzian Intensity	Lorentzian Width	Lorentzian Center
0	0.0020	0.1	0.22
10	0.0015	0.1	0.22
20	0.0010	0.1	0.22
30	0.0005	0.1	0.22
40	0.0001	0.1	0.22
Thickness (μm)			
3.7	0.0020	0.1	0.22
5.5	0.0020	0.1	0.22
5.9	0.0020	0.1	0.22
9.0	0.0020	0.1	0.22
14.2	0.0020	0.1	0.22

3.4 Results and discussion

3.4.1 Pore diameter and thickness effect on optical properties of Al/NAA systems

3.4.1.1 Reflectance

The effect of pore widening on reflectance was evaluated with samples obtained at 40 V in 0.3 M oxalic acid. A constant thickness of 9 µm was achieved after doing a second anodization process during 200 min. Figure 3.1 shows top SEM images of NAA before and after the pore widening process. Highly ordered structures were observed. The pore diameters (d_p) obtained for each pore widening time (t_{PW}) were 32 ± 6 nm, 50 ± 6 nm, 68 ± 6 nm, 72 ± 8 nm, 78 ± 13 nm, corresponding to 0, 10, 20, 30 and 40 minutes of t_{PW}, respectively. It can be observed that for t_{PW}=30 min, samples show some interconnected pores, caused by the excess of dissolution time. The t_{PW}=40 min samples exhibit collapsed nanotubes and most of the surface corresponds to texturized aluminum. The oxide detachment was generated by the complete dissolution of the pore bases after t_{PW}=40 min, then the value of 78 ± 13 nm corresponds to the pore base diameter in the textured surface.

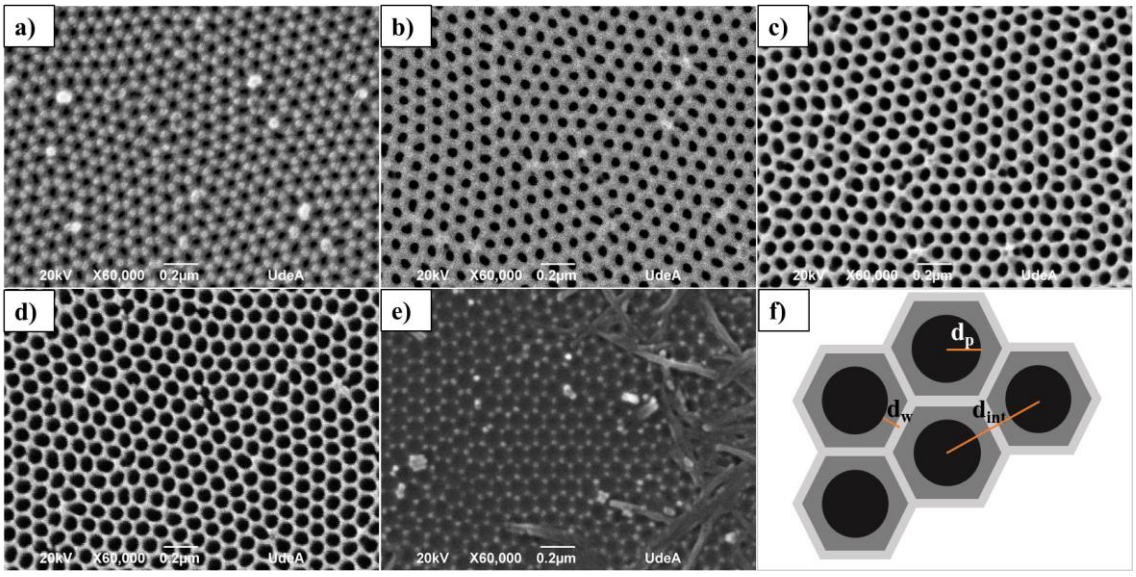

Figure 3.1 SEM images of NAA pores with different pore diameters prepared by the pore-widening process from 0 to 40 min:(a) 0 min, (b) 10 min, (c) 20 min, (d) 30 min, (e) 40 min and (f) schematics illustrating pore diameter d_p, interpore distance d_{int} and pore wall diameter d_w.

Figure 3.2a shows the measured reflectance spectra for samples with increasing t_{PW} (increasing d_p), and second anodization time of 200 min, corresponding to a porous oxide thickness of 9 µm. The spectra show an oscillating behavior in the wavelengths between 500 nm and 800 nm. It can be also observed that in the visible range, the

average reflectance was about the same for all samples. Nonetheless, in the UV range, the reflectance spectrum decreased between 500 nm and 200 nm. In this range, there is a smooth decrease between 500 nm and 350 nm and a strong drop between 350 nm and 200 nm. Such reflectance drop was stronger for the samples with shorter pore widening time. Figure 3.2a also reveals that as pore widening time increases, the drop in reflectance between 350 nm and 200 nm becomes less pronounced and for t_{PW} = 40 min (textured surface with collapsed nanopores) reflectance was close to that of the electropolished aluminum. The measurements put also in evidence that the amplitude of the oscillations decreased with the pore widening time and for the sample with t_{PW} = 40 min the reflectance spectra had no oscillations at all. The decrease in oscillation amplitude with t_{PW} agrees with the fact that the effective refractive index of the porous layer varies from a value close to the aluminum oxide (Al_2O_3) refractive index to the refractive index of air.

Figure 3.2b shows the simulations for increasing porosity of the NAA layer (corresponding to increasing t_{PW} and therefore d_p), assuming a zero extinction coefficient. Simulations are in good agreement with the measured spectra in the range between 500 nm and 800 nm: The oscillatory behavior and the approximately constant average reflectance are correctly reproduced. However, the observed experimental reflectance drop for wavelengths smaller than 500 nm is not reproduced by the simulation if zero absorption in the NAA layer is considered. Therefore, simulations incorporating absorption in the model were performed. Such absorption was introduced by considering a non-zero extinction coefficient which varies with the applied pore widening time. As described in the numerical details section, the strength of the absorption also decreases with the increase of t_{PW} to account for a non-uniform concentration of anion incorporated impurities and oxygen vacancies in the aluminum oxide matrix. Figure 3.2c shows the simulated specular reflectance spectra obtained under such assumption. In this case, there was a good agreement with the measured spectra: When pore widening time increases (d_p increases), the drop in reflectance becomes less pronounced. The simulation also agrees with the fact that the measured spectrum for t_{PW} = 40 min was similar to that typically obtained for electropolished aluminum [60].

Such good agreement permits to explain the behavior of the measured reflectance spectra: Oscillatory behavior in the range between 500 nm and 800 nm is due to thin-film multiple Fabry-Pérot interferences. The decrease in the amplitude of the oscillations and in the average reflectance in this range can be explained by changes in refractive index of the NAA layer caused by different proportions between alumina and air due to different porosity percentages. Porosity percentages were calculated and are specified in Table 3.1. On the other hand, the decrease in reflectance below 500 nm is caused by absorption. This is in agreement with the well-known fact that

during anodization in oxalic acid the O^{2-} ions can be easily substituted by oxalate anions, which concentration depends on the conditions of anodization [204] and also with the oxygen vacancies generated in the NAA during anodization [193,202]. In order to correctly reproduce the trend observed in the experimental measurements, consisting in the less pronounced decrease in reflectance below 400 nm for increasing pore widening time, it was necessary to consider a decreasing strength of the absorption with increasing t_{PW}. This supports the conclusion that oxalate anion incorporation is not uniform, being higher close to the pore-oxide interface and decreasing towards the inside of the pore walls [199].

Moreover, the differences in UV zone among the measured samples were consequence of the increasing dissolution time that dissolved the pore walls with the incorporated oxalate species, diminishing the absorption of the NAA layer. Consequently, longer PW times are equivalent to smaller pore wall diameter (d_w) and hence lesser amount of incorporated oxalate species whereby simulated curves considering a non-zero extinction coefficient, resemble better the measured spectra.

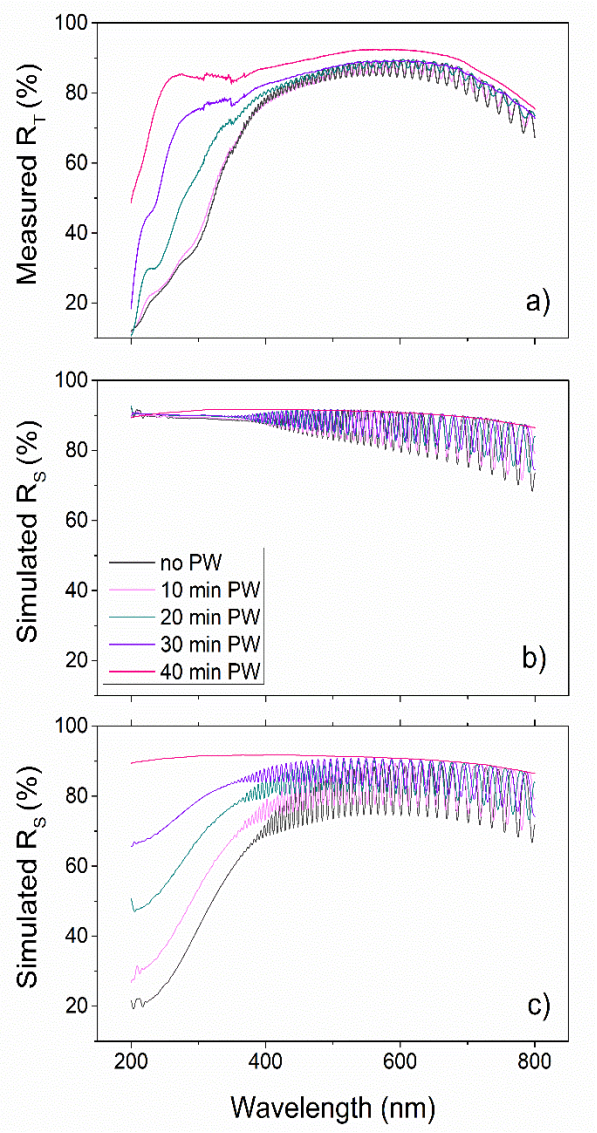

Figure 3.2 Measured and simulated UV-Vis reflectance spectra of Al/NAA samples with different t_{PW} (and d_p) a) measured, b) simulated assuming a zero extinction coefficient and c) simulated considering a non-zero extinction coefficient.

In order to further investigate the effect of the absorption caused by the incorporated oxalic anions, the influence of the NAA thickness on the total reflectance was also studied. For this aim, samples with the same porosity percentage (8.5 %, corresponding to as-produced samples) were fabricated varying the second anodization time between 78 min and 300 min. Samples with thicknesses 3.7 ± 0.6 µm, 5.5 ± 1.0 µm, 5.9 ± 0.7 µm, 9.4 ± 0.6 µm, 14,2 ± 0.8 µm were obtained and the total reflectance was measured. As the anodization conditions for all samples were kept the same, d_p of 32 ± 5 nm and d_{int} (interpore distance) of 114 ± 7 nm were also the same for all samples.

Figure 3.3a presents the measured total reflectance (R_T) spectra obtained from the NAA with different thicknesses. The spectra show an oscillating behavior in the wavelength range between 800 nm and 200 nm. Nonetheless, as thickness increases, the amplitude of the oscillations decreases, and the range of the spectrum where the oscillating behavior is observed, becomes smaller. Furthermore, in the UV zone the thickness effect is more perceptible, showing that thinner samples exhibited oscillations at lower wavelengths and the number of oscillations decreased as the thickness increases. In the visible and near-infrared ranges, the observed average reflectance was about the same. On the other hand, the reflectance spectra decreased in the region between 500 nm and 200 nm. Total reflectance at 200 nm was around 10% for all NAA thicknesses. As the thickness increased, the drop in reflectance became more pronounced at around 300 nm.

Figure 3.3b shows the simulated specular reflectance (R_S) for increasing second anodization time (corresponding to increasing thickness) including a nonzero extinction coefficient. Simulations reproduced the trends observed in the measured spectra. The oscillatory behavior is observed, and the average reflectance is similar in the visible zone for all NAA thicknesses. Furthermore, in the UV range, the number of fringes decreased with thickness and the amplitude of the oscillations decreased as the thickness increased. The observed experimental reflectance drop for wavelengths smaller than 500 nm was also reproduced by the simulation.

Including the absorption effect into the simulation, it was possible to reproduce the thickness effect on reflectance. The observed oscillations are due to Fabry-Pérot interference phenomenon. The intensity losses observed in thicker samples can be related to multiple reflections of the light combined with the fact that the material was slightly absorbing. In the same manner, the drop in reflectance below 500 nm must be generated by absorption. The reflectance drop started at lower wavelength as the sample was thinner, similarly to the experimental results. These results con^{f}irm that the model considered, including the effective medium approximation for the porous NAA layer and the nonzero extinction coefficient for the oxalic anions incorporated into aluminum oxide matrix, permits to predict the general trend of the actual total reflectance spectra of the Al/NAA systems.

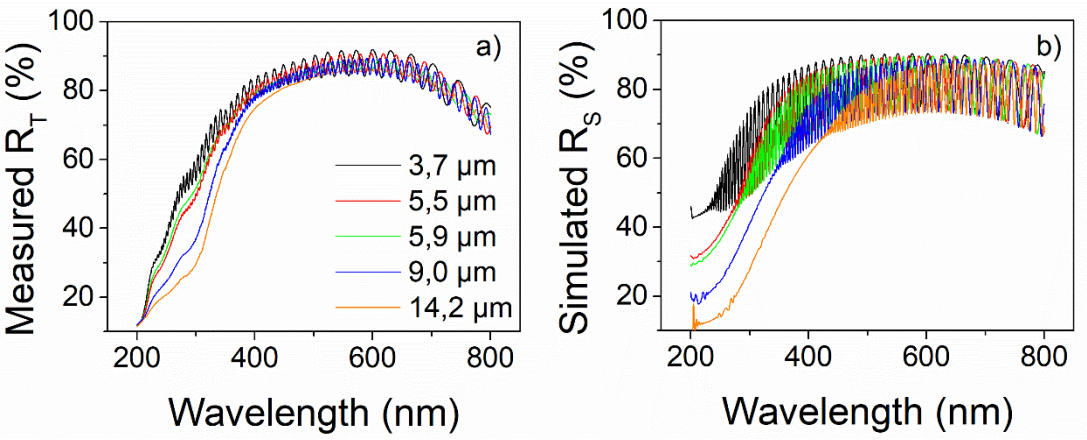

Figure 3.3 Measured and simulated UV-Vis reflectance spectra of Al/NAA samples with different thickness. a) Measured, b) simulated including absorption.

3.4.1.2 Photoluminescence

The PL spectra of samples 9 µm thick with increasing t_{PW} (increasing d_p) have been measured and shown in Figure 3.4a. At first glance, it is observed a wide band in the wavelength range of 400-600 nm which covers almost the whole visible waveband. It can also be observed a blue shift in the peak position with increasing t_{PW}. The samples corresponding to t_{PW} from 0 to 20 min show higher PL intensity compared to the t_{PW}=30 min and t_{PW}=40 min. The t_{PW}=30 min sample exhibits two visible peaks around 418 nm and 470 nm. The t_{PW}=40 min sample apparently presents three peaks at 423 nm, 471 nm conclusive and 544 nm. The t_{PW}=10 min sample exhibits oscillations corresponding to a Fabry-Perot interference, this phenomenon is better observed due to the effect of the d_p and NAA thickness as explain in [205].

A filter with cutoff wavelength below 400 nm was used to measure the PL spectra to suppress the light source effect, that generates the spectra start in a PL intensity different than zero and that can be taken for a peak in samples t_{PW}=30 min and t_{PW}=40 min. The measured spectra are shown in Figure 3.4b. The aluminum electropolished PL spectrum was also included in the figure. When using the filter, wide and asymmetric spectra were observed. In Figure 3.4b, the increase of t_{PW} resulted in a blue shift of the peak position as observed in Figure 3.4a and the oscillatory behavior of the t_{PW}=10 min sample is also observed. The observed spectrum for the t_{PW}=40 min sample also presented three peaks in almost the same positions of the Figure 3.4a; 429 nm, 473 nm and 544 nm. The electropolished aluminum PL properties were also measured revealing three PL peaks close to the observed for the t_{PW}=40 min sample.

The observed blue shift with t_{PW} from Figure 3.4a and b, is in good agreement with other authors observations [158,206] and this emission is usually attributed to single ionized oxygen vacancies F^+ formed during anodization. Nonetheless, further investigations have been carried out to understand the origin of luminescent centers in NAA and will be discussed afterwards. The low intensity of t_{PW}=30 min PL spectrum is the result of the dissolution of some of the luminescent centers. It is well known that pore wall composition is inhomogeneous, the defects density is higher at the outer part of the wall, the one that is in direct contact with the electrolyte [44,206]. Then, considering a concentration gradient from the outer pore wall to the inner and pristine part of the pore wall and according to the pore wall dissolution induced by pore widening process shown in Figure 3.1d, the low intensity of t_{PW}=30 PL is explained. The t_{PW}=40 min has similar PL spectra to the electropolished aluminum as observed in [207], these results are in agreement with the fact that the NAA was detached from the aluminum surface after t_{PW}=40 min as observed from Figure 3.1e. The low intensity emission can be attributed to the remaining alumina of some nanometers thick corresponding to the collapsed nanopores for the t_{PW}=40 min sample (Figure 3.1e) and to the natural oxide layer existing in the electropolished aluminum surface.

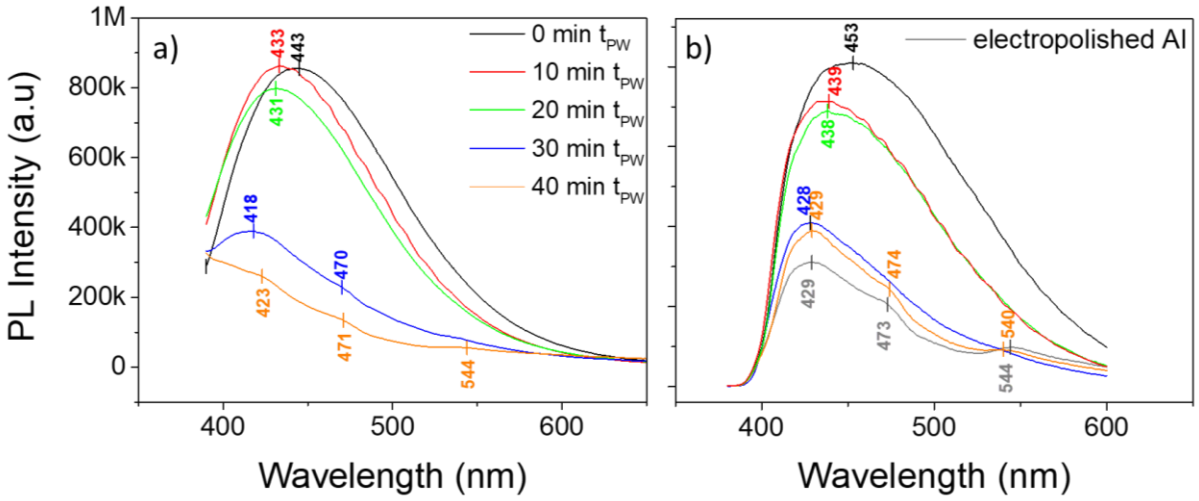

Figure 3.4 Photoluminescence spectra as function of t_{PW} (and d_p). (λ_{ex}=360 nm). a) Without using 400 nm filter and b) by passing through a filter with cutoff wavelength below 400 nm, including the electropolished (EP) aluminum spectrum.

Some authors [194,207–210] have decomposed the PL spectra in several Gaussian distributions, and it was found that deconvolution with a minimum of two components reproduced the measured spectra with a high fit accuracy. From Figure 3.5 it can be observed that for the emission PL spectra generated at an excitation wavelength of 360 nm have been deconvoluted by Gaussian functions into three emission bands for t_{PW}=0 min, t_{PW}=10 min and t_{PW}=0 min and into two emission bands for t_{PW}=30 min

and t_{PW}=40 min. The spectra parameters extracted from deconvolution of PL spectra of NAA are presented in Table 3.3.

From Figure 3.5 a-c it is observed a blue shift from 418 nm to 411 nm corresponding to the peak 1, a blue shift from 453 nm to 441 nm for peak 2 and a shift 495 nm to 476 nm for peak 3. The sample corresponding to t_{PW}=30 min (Figure 3.5d) keeps the blue shift tendency but the third peak is not observed. The spectrum corresponding to the t_{PW}=40 min sample was deconvoluted in two peaks like those presented for the electropolished aluminum but with no correlation to the peaks observed for samples from t_{PW}=0 min to t_{PW}=30 min.

The origin of the luminescent centers has been two main approaches, those who attributed the PL properties of NAA only to oxygen vacancies being single ionized F^{+}, double ionized F, or less likely unstable F^{++} centers (vacancies without electrons) [44,192–194,206,208,211] and those who concluded that not only oxygen defects are responsible for NAA fabricated in oxalic acid but also oxalate ions incorporated into the NAA that can turn into luminescent centers due to the presence of delocalized electrons of π bonds, responsible for excitation in the ultraviolet region [198,201,207,210,212–214]. The present results show three peaks corresponding to three luminescent centers. Emission peak 2 (453 nm) is the most intense emission band and might be attributed to F centers, whereas the second most intense peak (peak 1) might be attributed to F^{+} centers (418 nm) [44,208]. During anodization, anions will drift to the anode under the action of the electric field and then, some anions will gather on the surface of the NAA. The oxygen vacancies located on the surface can easily trap two electrons and become F centers. According to this, the F centers density decreases with the pore wall depth [44]. From Table 3.3 it can be observed that the intensity of the peak 2 (F) decreases as t_{PW} increases agreeing with the gradual elimination of F centers with t_{PW}.

From Table 3.3 it can also be observed that the intensity of peak 1 (F^{+}) increases and then decreases with t_{PW}; this result agrees with previously reported results [206,215] showing that F^{+} centers distribution is opposite to F; the density of F^{+} increases with pore wall depth until it reaches the pure alumina zone in the innermost part of the pore wall. The less intense peak band around 495 nm (peak 3) might be attributed to the incorporated oxalate ions [198]; this last conclusion is also based on the fact that oxalate impurities are located at the outer region of the pore [196] being firstly removed. As t_{PW} increases a decrease in peak intensity is expected, until the outer oxalate containing zone of the pore wall is completely dissolved and the peak disappears.

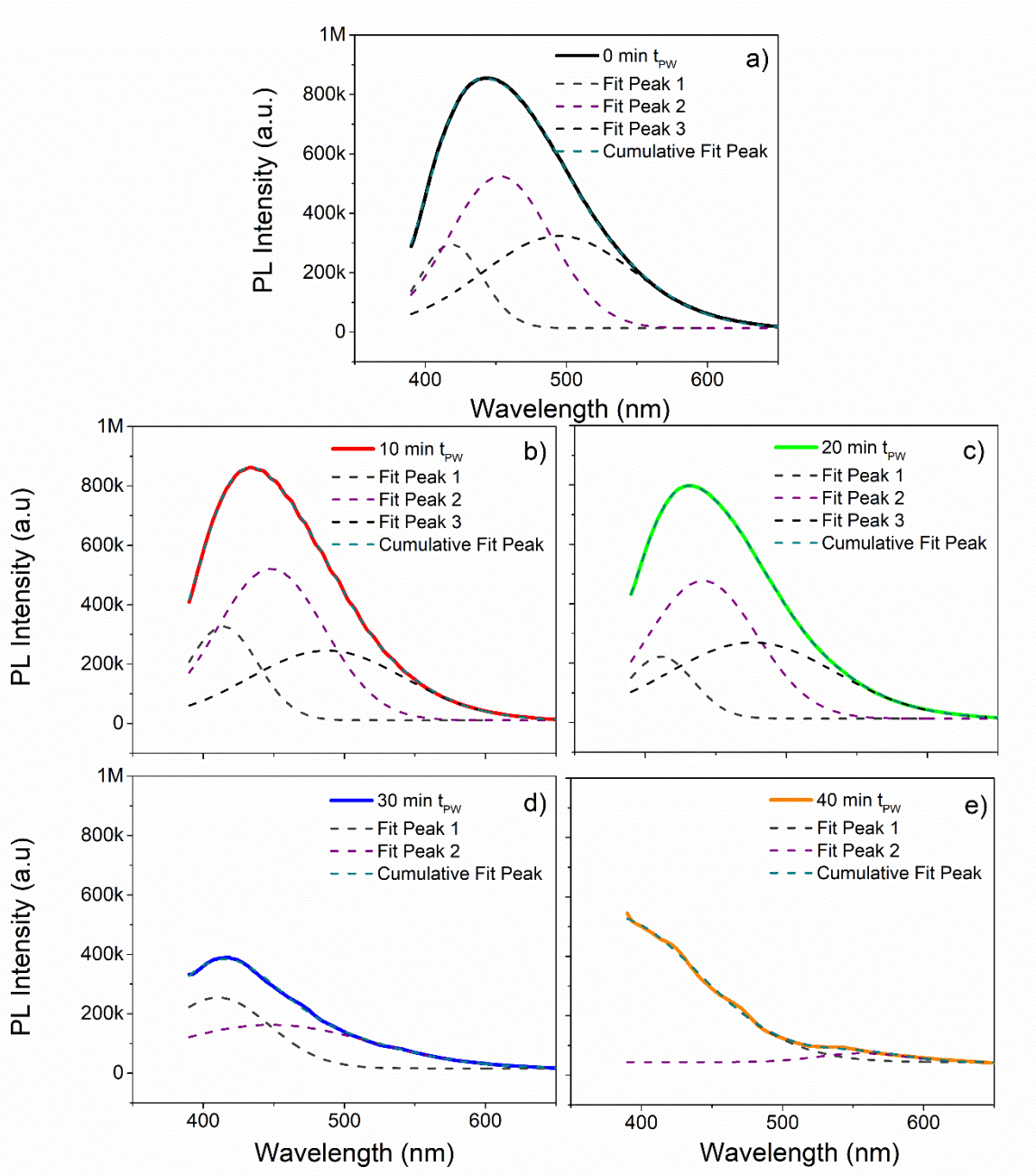

Figure 3.5 Deconvolution by Gaussian fitting of NAA PL spectra as function of t_{PW} (and d_p). (λ_{ex}=360 nm). a) t_{PW}=0 min, b) t_{PW}=10 min, c) t_{PW}=20 min, d) t_{PW}=30 min and e) t_{PW}=40 min.

Table 3.3 Spectra parameters extracted from direct PL spectra of NAA and from deconvolution of PL spectra of NAA evaluated at different t_{PW}.

40V t_{PW}=0 min					
Direct observation		Without filter			400 nm filter
		Fit accuracy (R^2) =0.99988			R^2=0.99324
	Center (nm)	Center (nm)	FWHM (nm)	Height (a.u.)	Center (nm)
Peak 1	443	418	52	282	425
Peak 2	-	453	85	511	459
Peak 3	-	495	127	310	516
40V t_{PW}=10 min					
Direct observation		Without filter			400 nm filter
		Fit accuracy (R^2) =0.99992			R^2=0.99324
	Center (nm)	Center (nm)	FWHM (nm)	Height (a.u.)	Center (nm)
Peak 1	433	414	51	315	423
Peak 2	-	448	89	510	456
Peak 3	-	488	130	235	515
40V t_{PW}=20 min					
Direct observation		Without filter			400 nm filter
		Fit accuracy (R^2) =0.99998			R^2=0.99362
	Center (nm)	Center (nm)	FWHM (nm)	Height (a.u.)	Center (nm)
Peak 1	431	411	54	209	424
Peak 2	-	441	91	464	457
Peak 3	-	476	139	256	514
40V t_{PW}=30 min					
Direct observation		Without filter			400 nm filter
		Fit accuracy (R^2) =0.99942			R^2=0.99509
	Center (nm)	Center (nm)	FWHM (nm)	Height (a.u.)	Center (nm)
Peak 1	418	410	87	239	422
Peak 2	470	448	167	147	453
Peak 3	-	-	-	-	515
40V t_{PW}=40 min					
Direct observation		Without filter			400 nm filter
		Fit accuracy (R^2) =0.99898			R^2=0.99786
	Center (nm)	Center (nm)	FWHM (nm)	Height (a.u.)	Center (nm)
Peak 1	423	376	151	494	422
Peak 2	471	-	-	-	452
Peak 3	544	556	75	30	524

The effect of NAA thickness on its PL properties can be observed in Figure 3.6. The PL spectra were measured by passing through a filter with cutoff wavelength below 400 nm (λ_{ex}=360 nm). Form Figure 3.6a, it can be noticed a wide PL spectra in the visible zone. It is also evident for the thinner samples, 3.7 to 5.9 µm, spectra interference corresponding to Fabry-Perot oscillations while thicker samples

suppressed this behavior in the evaluated wavelengths. In terms of the peak position the effect is not clear due to the fringes. Gaussian deconvolution was performed, and the results are shown in Figure 3.6 b-e. The spectral deconvolution of the emission band in the NAA with different thicknesses spectra revealed three main emission peaks (Table 3.4). The three peaks are located near the same values 425 nm, 457 nm and 514 nm for all thicknesses. There is a red shift compared to the peaks observed in Figure 3.5a, but the values correspond to the calculated for the Figure 3.5b. The peak location can only be compared to samples measured under the same excitation wavelength and using a 400 nm filter. Nonetheless, the measured spectra and deconvoluted peaks can be used to evaluate the thickness effect on the peak location. NAA thickness was expected to have an influence in the PL intensity, nevertheless, it was only perceptible amongst thinner and thicker samples, but a constant PL intensity increase was not detected with the increase in thickness.

The results shown in Figure 3.6 and Table 3.4 support the previous conclusion. The most intense peak was peak 2 located at ~455 nm and attributed to F centers, the less intense peak 1, situated at ~423 nm is due to F^+ luminescent centers and peak 3 with a maximum around 512 nm is attributed to oxalate species. It is observed an intensity increase of peak 3 with thickness, corresponding to more anions incorporated into the anodic layer due to longer anodization time.

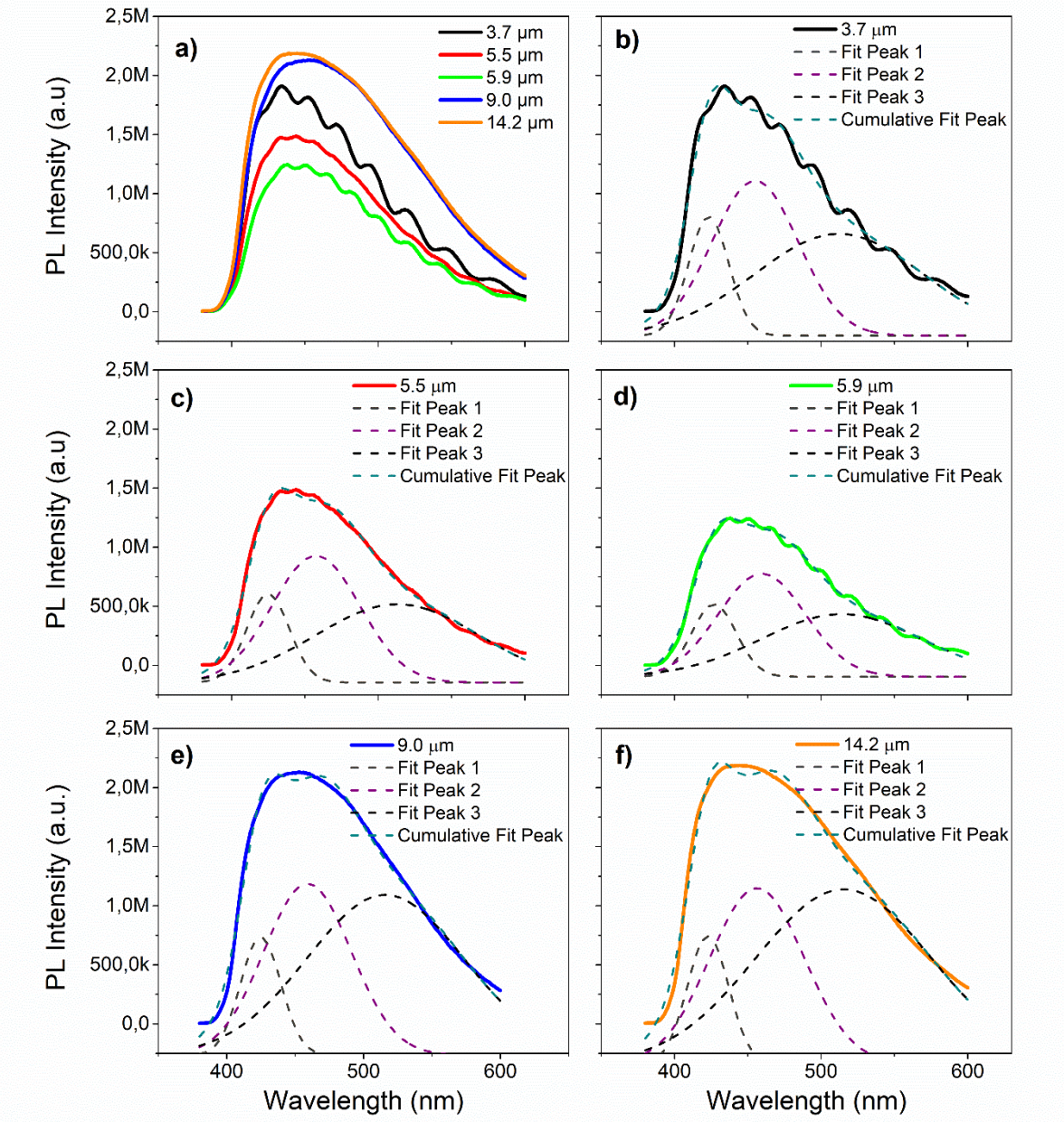

Figure 3.6 Deconvolution by Gaussian fitting of NAA PL spectra as function of NAA thickness by passing through a filter with cutoff wavelength below 400 nm (λ_{ex}=360 nm).

Table 3.4 Spectra parameters extracted from deconvolution of PL spectra of NAA with different thicknesses.

	Thickness (µm)				
	3.7	**5.5**	**5.9**	**9.0**	**14.2**
Peak 1 center	423	425	427	425	423
Peak 2 center	455	457	460	459	456
Peak 3 center	512	513	514	516	515
Fit accuracy R^2	0.98903	0.99475	0.99462	0.99395	0.99223

3.4.2 Influence of TiO_2 thickness on optical properties of Al/NAA/TiO_2 systems.

The effect of the TiO_2 thickness on reflectance was evaluated by depositing different number of TiO_2 layers on the top of NAA 9 µm thick. The measured TiO_2 thicknesses were 88 ± 13 nm, 196 ± 16 nm and 438 ± 34 nm obtained by 16, 32 and 64 sprayed TiO_2 layers, respectively. Thinner TiO_2 thicknesses could not be properly measured from cross-section SEM images due to the TiO_2 layers copied the NAA morphology making them indistinguishable. Therefore, the thinner TiO_2 thicknesses were found by extrapolation. The values obtained were 3.5 nm, 7.9 nm, 17.6 nm, 39.3 nm for 1, 2, 4 and 8 TiO_2 layers, respectively. Figure 3.7 shows top-view and cross-section SEM images of NAA after TiO_2 deposition. The number of sprayed layers is indicated in each case. It can be observed that for TiO_2 thicknesses between 3.5 nm and 40 nm, the TiO_2 deposited mainly on the aluminum oxide and at the pore opening boundaries. The pores are increasingly occluded for increasing number of sprayed TiO_2 layers. In the samples sprayed with 1 to 4 TiO_2 layers, the NAA morphology is still observed. For the sample with 16 sprayed TiO_2 layers, despite the NAA underlying structure is almost completed occluded, a periodic nanoporous morphology remains apparent. Otherwise, the surface of the sample with 64 TiO_2 layers consists of packed grains without any voids or cracks, similar to other reports [216].

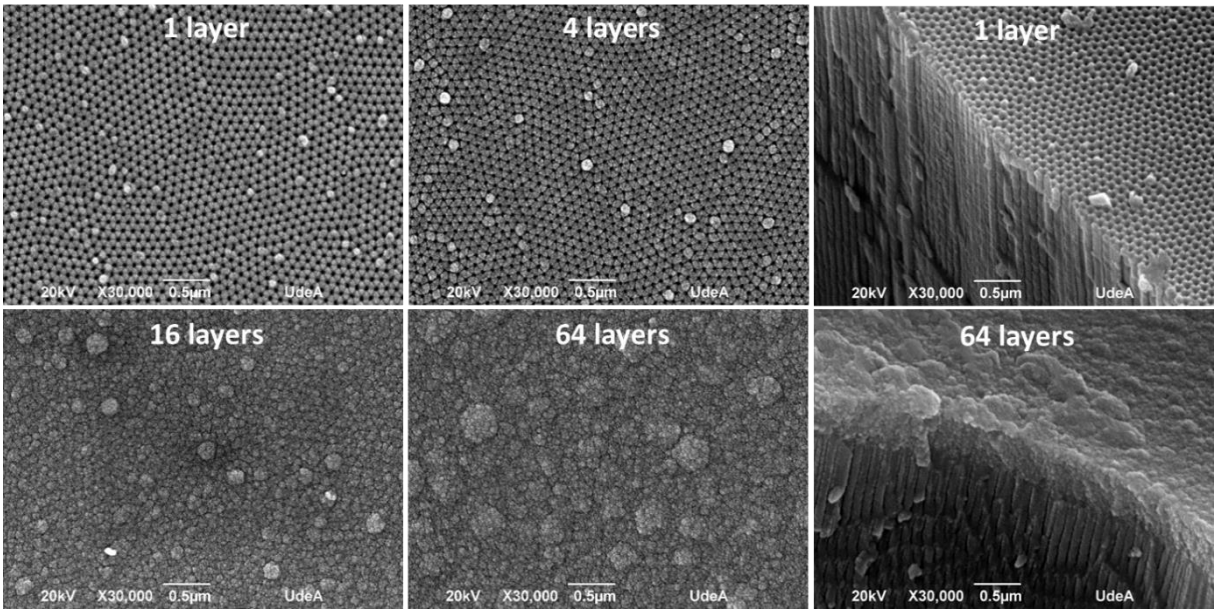

Figure 3.7 Top and cross section SEM images of Al/NAA/TiO_2 with different thicknesses of TiO_2 obtained by spray pyrolysis. 1, 4, 16 and 64 with TiO_2 of 3.5 ± 0.5, 18 ± 3, 88 ± 14 and 438 ± 68 nm thick respectively. The NAA thickness was constant (around 9 µm).

Figure 3.8 shows the measured total reflectance spectra of Al/9 µm NAA compared to Al/9 µm NAA/TiO_2 samples with increasing number of sprayed TiO_2 layers. The Al/NAA spectra (black curves) were previously described (see blue curve in Figure 3.3a). As expected, the Al/NAA/TiO_2 spectra exhibits a more complex fringe pattern than the Al/NAA systems with an oscillatory modulated behavior in the visible and NIR ranges (see Figure 3.8d). In the UV zone there is a strong R_T drop between 400 nm and 300 nm accompanied by a slight increase on reflectance around 260 nm as TiO_2 thickness increases. It is also observed a shift to the right of the minimum reflectance (between 250 nm and 350 nm) with the increase of TiO_2 thickness. Additionally, the intensity of the Fabry-Perot oscillations corresponding to the former NAA structure, augmented for TiO_2 thicknesses between 3.5 nm and 40 nm (corresponding to 1-16 TiO_2 layers). This enlarged R_T intensity is observed in Figures 3.8a and b. The frequency of the exhibited modulations in the reflectance spectra appears to raise with TiO_2 thickness, as disclosed in Figures 3.8c and d; higher frequencies are reached as TiO_2 thickness increases. The drop in reflectance observed for the Al/NAA samples starts closer to the NIR as TiO_2 thickness increases.

The sprayed TiO_2 layers effect, characterized mainly by the modulation in the reflectance spectra of the Al/NAA samples, is a phenomenon that occurs gradually as TiO_2 becomes thicker. This modulated oscillating behavior is characteristic of bi-layer films and is caused by differences in the refractive index of the layers [184,217]. Form Figures 3.8c and d, corresponding to TiO_2 thicknesses between 87 nm and 438 nm (16-64 TiO_2 layers) it is easy to observe these typical bi-layer behavior where the oscillations corresponding to the NAA and TiO_2 layers are superimposed, generating that the Fabry-Pérot oscillations corresponding to the NAA layer present modulations in the evaluated wavelengths range. The differences in the UV zone are caused by the combined effects of the absorption and thickness of TiO_2 coatings.

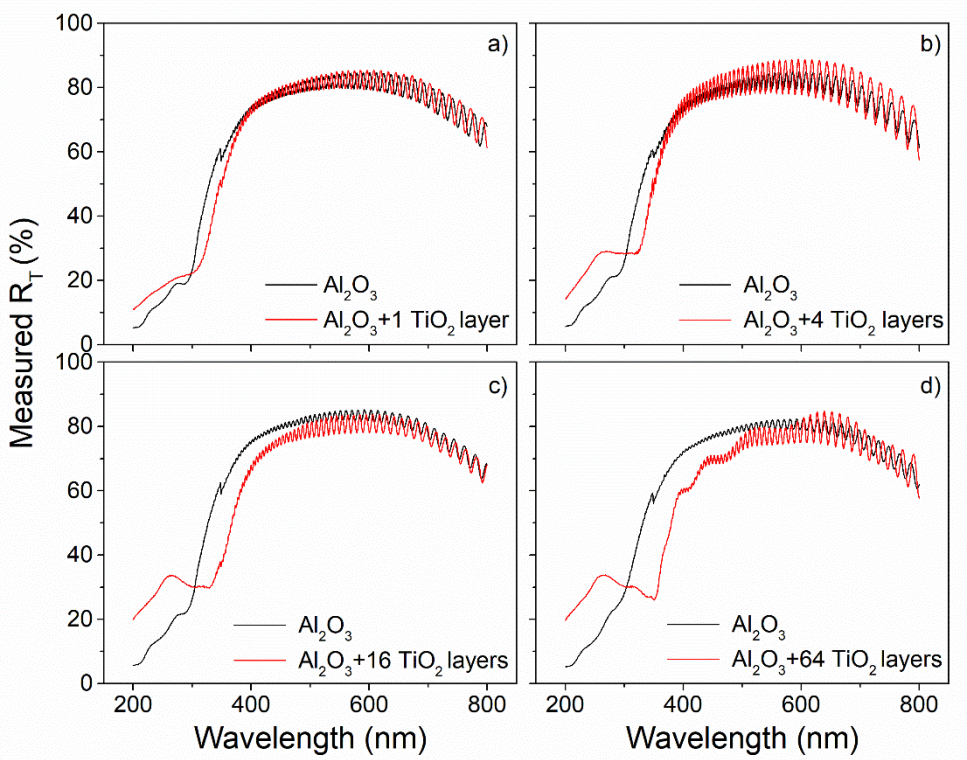

Figure 3.8. Measured UV-Vis total reflectance spectra of Al/NAA and Al/NAA/TiO_2 samples with different TiO_2 thicknesses. Black lines represent samples without TiO_2 and red lines represent samples with TiO_2 coating. (a) 3.5, (b) 17.6, (c) 87.7 and (d) 438.0 nm. The NAA thickness was constant (around 9 µm).

Figure 3.9 shows measured (total and specular) and simulated UV-Vis reflectance spectra of Al/NAA/TiO_2 samples with 32 and 64 TiO_2 layers. All the spectra show similar characteristics, which are clearly related to the number of TiO_2 layers deposited. The simulations reproduced the observed modulated oscillatory behavior. Although the amplitude of the oscillations resulted to be higher than in the experimental spectra, the simulated spectra are a close resemblance of the measured data. The number of modulations maxima and minima is well reproduced by the simulations. The good agreement between measurements and simulations permit to obtain information about the causes of the different features in the spectra. The strong reflectance drop between 400 nm and 300 nm is caused by the absorption in the TiO_2 layer, while the increase in reflectance below 300 nm agrees with the model of Al/thick NAA and thin layer of TiO_2. Simulations of the Al/NAA/TiO_2 systems can be used to determine the TiO_2 thickness by adjusting its thickness fitting the maximum points of the modulated spectra with the measured curves.

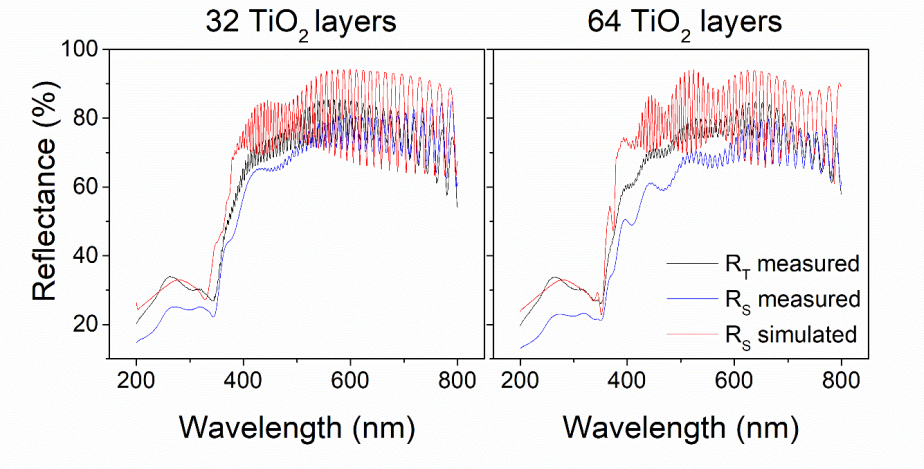

Figure 3.9 Measured and simulated UV-Vis reflectance spectra of Al/NAA/TiO_2. Red lines represent modeled specular reflectance with effective medium approximation (E.M.A.) using NKDGen software.

3.5 Conclusions

The evaluation of the influence of morphological features on the optical behavior of Al/NAA and Al/NAA/TiO_2 was presented. The reflectance of Al/NAA and Al/NAA/TiO_2 samples was modeled by using E.M.A. approximation without extinction coefficient and by considering the absorption of the incorporated oxalate ions and oxygen vacancies into the model.

The number and intensity of the Fabry-Perot fringes observed in the reflectance spectra were highly influenced by the pore diameter (d_p) and thickness of both the NAA and TiO_2 layers. A minor effect on the average reflectance was observed by modifications in the evaluated morphological features but this influenced the oscillating behavior. It was found that the pore widening process (therefore the d_p) had a major effect in the UV zone of the reflectance spectra.

Thin TiO_2 coatings increased the intensity of the oscillations produced by NAA, whereas, thicker TiO_2 layers generated a modulated oscillating behavior in the evaluated range. Simulations without considering the absorption of the NAA layer reproduced the pore widening and thickness effects in the visible region. On the other hand, the method fails to predict the decrease in reflectance in the UV range, leading to the assumption that non-absorbing NAA was not pertinent to describe the real behavior of the samples. When variations in absorption were considered, the drop in reflectance and the overall spectra shape observed in the measured reflectance were well reproduced by the simulations. The Al/NAA/TiO_2 systems were successfully simulated and it appears to be a method to determine the TiO_2

thickness by fitting the maximum points of the modulated spectra. According to the reported results, it was shown that it is critical to consider the absorption of the incorporated oxalate species and oxygen vacancies to obtain accurate predictions of the optical behavior of NAA in the UV range.

The results showed that the photoluminescence (PL) emission of NAA might be associated with the presence of recombination centers from oxygen defects and oxalate ions inside the oxide structure. Gaussian deconvolution of NAA PL spectra gives three main bands located around 420 nm, 455 nm and 490 nm; the first two peaks corresponding to F^+ and F oxygen vacancies respectively, and the last one to incorporated oxalate impurities. It was found that the PW process has a major influence in the PL spectra generating a blue shift with the increment of t_{PW}. Meanwhile, the NAA thickness does not affect the PL peak position.

4. INFLUENCE OF ANODIZING POTENTIAL ON NAA AND NAA/TiO_2 OPTICAL PROPERTIES

4.1 Introduction

Nanoporous anodic alumina (NAA) has been receiving increasing attention due to its excellent electronic and optical properties and self-ordering characteristics, exhibiting a wide range of applications in sensing, energy and photonics [116,163].

The optical properties of NAA have been studied by many researchers focusing in the interesting photoluminescent (PL) response of NAA produced in phosphoric, sulfuric, malonic and oxalic acids [192,195,213,218–221]. The PL emission of NAA produced in oxalic acid has been reported as the strongest and many efforts have been carried out in order to understand the origin of this PL response. Some researchers observed that the PL position of the emission and excitation bands depends on the monitored wavelength [222,223]. Other authors evaluated the influence of annealing temperature on emission peak position and intensity, founding that with rising annealing temperature, the intensity of emission band peaking around 470 nm increases first, reaches a maximum when temperature is close to 500 °C, and then decreases [193,224]. The origin of the PL bands observed in NAA obtained in oxalic acid has been attributed to two main centers being oxygen defects and oxalate impurities incorporated into the NAA during anodization. Comparisons with PL emissions obtained from samples anodized in sulfuric acid revealed the samples obtained in oxalic acid showed a different band around 410 nm attributed to oxalate impurities [213]. Nonetheless, a quantitative investigation in the influence of oxalic impurities on photoluminescence properties of NAA showed that the carboxylate ions are not the direct reason for the PL of oxalic NAA, the authors compared the oxalate ions content and PL intensity of NAA to reach that conclusion [212,224]. Other researchers defined the PL spectra of NAA films as asymmetrical and divided it using two Gaussian functions, each band was attributed to one kind of oxygen defect centers, namely, F^+ (oxygen vacancy with only one electron) and F (oxygen vacancy with two electrons) centers [43,44,211]. The broad emission band peaking at around 452 nm observed by Li, Y. [212] was also divided in two sub-peaks located at 443 nm and 470 nm; they attributed those peaks to two luminescence centers in porous alumina membranes, namely, oxygen defects and oxalic impurities. Ghrib, M. et al., [222] and Huang, G. et al. [223] measured de PL of NAA obtained in sulfuric acid and identified two bands, the high energy band centered at 460 nm was associated with oxygen adsorption at the pore wall and oxygen vacancies positioned inside the oxide barrier layer and the second band around 500 nm was associated to the adsorption of water and/or OH groups at the surface of the pore wall and to structure defects and sulfur inclusion inside the oxide barrier layer.

Besides PL, other optical properties like transmittance, absorptance, reflectance and optical constants have been measured and simulated. These optical properties are usually evaluated in the visible (Vis) range and NAA has been known as transparent [94,111,173,201,224,225]. Nonetheless, NAA produced in oxalic acid presents an interesting behavior in the ultraviolet (UV) range exhibiting a heavy absorption. A

strong ultraviolet (UV) band gap absorption region around 3.5–4.2 eV has been reported [201] even though the theoretical band gap of Al_2O_3 was reported around 6.242 eV (200 nm) [226]. Optical absorption in the 1 to 5.8 eV range indicates that absorption mainly occurs by the energy levels located within the band gap of NAA. However, the effective absorption within the band gap is related to the oxygen defect density or to the amount of incorporated species from electrolyte [227]. Some authors have measured absorption and reported peaks located within the band-gap but at different positions. Efeoğlu et al. [227], described the absorption as a tail of the main absorption band at 200 nm, Gao et al. [198] reported two absorption peaks at 250 nm and 300 nm, Li el al. [193] observed four absorption bands located at 204 nm, 220 nm, 254 nm and 294 nm, Wang et al. [228] derived the optical energy gap (E_g) from Tauc's extrapolation, and determined that E_g increases from 4.178 to 4.256 eV with the anodizing voltage. Yan [203], showed spectra for samples annealed at 600 °C and 900 °C together with a spectrum deconvolution using four absorption sub-bands at 3.8 eV (326.3 nm), 4.3 eV (288.3 nm), 4.9 eV (253.0 nm), 5.4 eV (229.6 nm) and 6.1 eV (203.2 nm). Ealet et al. [229] stated that the reduction of the stoichiometry in γ-alumina induces the presence of defect levels located in the band gap decreasing the band gap from 8.7 eV (142.5 nm) to 2.5 eV (495.9 nm) at the surface. It has been well stablished that NAA exhibits a wide band-gap in the UV range and it is also clear that there are some absorption bands located within that band-gap. The number of absorption bands oscillated between two and five mainly attributed to oxygen defects and anion incorporated species depending on the research group. In this work, PL measurements have been carried out to identify the PL centers in NAA obtained in oxalic acid solution. Moreover, to reproduce the reflectance response of NAA obtained in oxalic acid electrolyte, numerical simulations based on the Transfer Matrix Method [184–186] including three absorption centers into the extinction coefficient were used. A Bruggeman effective medium approximation (E.M.A) is used to model the porosity of both the NAA film and of the porous sprayed TiO_2 film.

4.2 Experimental procedure

Nanoporous anodic alumina membranes were obtained from pure aluminum substrates (99.999% from Metalmen) using the two-step anodization process in oxalic acid 0.3 M at 5 °C. Prior to anodizing the aluminum was heat treated at 500 °C for five minutes and then electropolished using the modified Brytal process as described in [187]. The applied potentials were 40 V, 50 V, 55 V, 60 V and 75 V the second anodization times were 200 min, 105 min, 80 min, 65 min and 15 min respectively in order to obtain oxide films 9 µm thick.

The titanium dioxide (TiO_2) coatings were obtained by means of spray pyrolysis technique. A precursor solution of 0.2 M titanium diisopropoxide bis

(acetylacetonate) was used. The coated samples correspond to those obtained at 40 V, 50 V, 55 V and 60 V. The Al/NAA substrates were placed on a hot plate at 500 °C during the spray process as described in [172]. The evaluated TiO_2 thicknesses were 18 µm, 88 µm and 196 µm obtained by spraying 4, 16 and 32 layers of TiO_2 respectively. The TiO_2 annealing was performed by leaving the coated samples during 1 hour on the hot plate at 500°C.

The samples were characterized by Scanning Electron Microscopy (SEM), total reflectance spectra were obtained by UV/VIS spectroscopy, using a Cary 100 Spectrophotometer with integration sphere with an 8° edge. The specular reflectance measurements were performed in a PerkinElmer Lambda 950 UV/VIS/NIR using the Universal Reflectance Accessory (URA). The photoluminescence (PL) measurements were taken on a fluorescence spectrophotometer from Photon Technology International Inc. with a Xe lamp used as the excitation light source at room temperature and an excitation wavelength (λ_{ex}) of 360 nm and the spectra were normalized. The standard image-processing package (ImageJ, public domain program developed at the RSB of the NIH, USA) [188] was used to analyze the SEM images.

4.3 Numerical modeling procedure

Numerical simulations of the reflectance based on the Transfer Matrix Method [184–186] were carried out to better understand the measured reflectance spectra. The numerical simulations considered a model composed of an aluminum substrate and a thin film corresponding to the nanoporous anodic alumina (NAA). In the case of the Al/NAA/TiO_2 samples, the system was designed as an aluminum substrate with two thin films on top corresponding to NAA and porous TiO_2. In the simulation, normally incident light was assumed and specular reflectance was calculated.

The porosity of both the nanoporous aluminum oxide film and the porous sprayed TiO_2 film was modeled as a mixture of the corresponding oxide and air, using a Bruggeman effective medium approximation (E.M.A.). The E.M.A. considers the refractive index and the volume fraction of each constituent material (oxide and air), being the volume fraction of air equivalent to the porosity. Refractive indices of aluminum, aluminum oxide, and titanium dioxide have been taken from literature [189,190]. Pore diameter (d_p) and porosity (P) were estimated from top-view SEM pictures of the samples.

As observed from Chapter 3, the model with zero extinction coefficient do not reproduce the reflectance behavior of NAA in the UV range and that was the reason to model the extinction coefficient including non-zero absorption. Bertó-Roselló, F.,

et al. [230] used finite difference time domain (FDTD) method to include texturization into the numerical modelling and obtained good agreement with the measurements. Kuang, D., et al. [231] introduced small nanopores into the simulation model and observed that the oscillations of the reflectance were reduced in the blue region while the amplitude of the reflectance in the red region also decreases because the small nanopores scatter more incident energy, achieving good fit between modeled and measured reflectance.

The diffraction of light due to texturization of the aluminum substrate or due to the ordering level of the NAA structures was considered as a possible cause to explain the differences in reflectance in the UV range between the evaluated potentials. Total (R_T) and specular (R_S) reflectance were measured for texturized aluminum (Al surface after anodizing and oxide removal), for NAA obtained at 40 V and for NAA obtained at 60 V (See Figure 4.1). From Figure 4.1 it can be noticed that the drop in reflectance in the UV region is observed in both R_T and R_S spectra of the anodized samples and the differences between R_T and R_S are constant in the whole evaluated wavelength range. Then, the drop in reflectance was not generated by diffraction. The difference between R_T and the R_S increased with anodization potential. The reflectance of the texturized aluminum was 1% to 2% lower than the exhibited for the electropolished aluminum. The difference between R_T and R_S was higher for NAA sample obtained at 60 V than the difference between R_T and R_S observed for NAA samples obtained at 40 V. The latter can be related to scattered light rays by the more irregular and rough structure of the NAA obtained at 60 V.

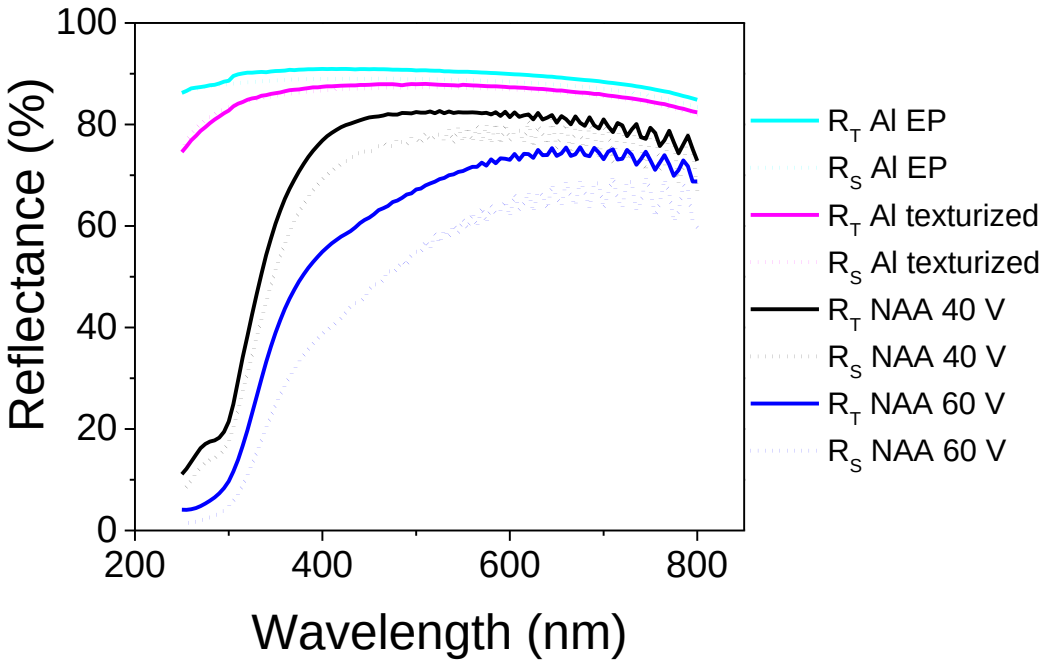

Figure 4.1 Measured total reflectance (R_T) and specular reflectance (R_S) for electropolished aluminum (Al EP), texturized aluminum, NAA obtained at 40 v and NAA obtained at 60 V.

Discarding the effect of loses due to diffuse reflectance, absorption was introduced in the model for the aluminum oxide. The first approximation to reproduce the measured reflectance of NAA was developed in chapter 3, nonetheless, the current approach considers three absorption centers instead of one. The absorption centers are related to the presence of oxygen vacancies [44,191–196] and incorporated anions [201,207,210,212,214]. Absorption was considered into the model by assigning nonzero values to the extinction coefficient. These values follow the envelope created from three Lorentzian curves, each one corresponding to an absorption center according to literature and measured samples [232,233]. The central wavelength of each absorption center, its width and height (intensity) are specified in Table 4.1. The height of the Lorentzian determines the strength of the absorption, such strength increases with the applied potential [228].

Table 4.1 Values used to model and simulate the NAA reflectance with the proposed absorbing extinction coefficient.

Potential	Center (nm)	Intensity	Width	Thickness (µm)	Porosity (%)	Smoothened points
40V	200	0,0030	0,007	9	7.997	3

	250	0,0019	0,006			
	295	0,0015	0,006			
50V	200	0,0050	0,007	9	9.677	3
	250	0,0027	0,006			
	295	0,0016	0,006			
55V	200	0,0055	0,007	9	12.114	4
	250	0,0038	0,006			
	295	0,0026	0,006			
60V	200	0,0055	0,007	9	9.953	5
	250	0,0045	0,006			
	295	0,0031	0,006			

4.4 Results and discussion

4.4.1 Optical properties of Al/NAA

Figure 4.3 shows the typical PL emission spectra of NAA prepared in oxalic acid as a function of anodizing potential. The excitation wavelength was 360 nm. The spectra have a wide shape in the visible zone. A clear trend was not observed for the peak position with the applied voltage (See Figure 4.3a). To better understand the origin of the PL response of NAA, the spectra were deconvoluted in three Gaussian functions with peaks around 420 nm, 450 nm and 490 nm as shown in Figure 4.3b-f. It should be noticed that for samples anodized from 40 V to 60 V the higher peak was the one located around 450 nm but for the 75 V sample was the blue one located around 470 nm.

Peaks position were analyzed with anodizing potential and shown in Figure 4.4a. Error bars corresponding to standard deviation of the data were included. It was observed that error bars were larger for peak 3 and almost imperceptible for peak 1 for all samples but 75 V one. Peak one was located around 420 nm for 40 V, 50 V and 60 V samples, it shows a blue shift of a few nanometers for the sample anodized at 55 V and then a red shift for the 75 V sample. Peak two was centered around 450 nm for the samples anodized at 40 V, 50 V and 55 V, it presents a small blue shift for the 60 V sample and a red shift to 465 nm for the sample anodized a higher potential (75 V). The more pronounced differences were observed in the position of peak three. It was located around 490 nm for 40 V, 50 V and 55 V. There was a blue shift for both the 60 V and 75 V samples, albeit the error bars of the 60 V sample overlap with the error bars obtained for lower potential samples it is still observed a trend.

Peaks intensity vs anodizing potential are depicted in Figure 4.4b. Error bars are included. The intensity of peaks one (420 nm) and three (490 nm) was the same for

samples anodized at 40 V, 50 V and 55 V and it was lower to the intensity of peak 2. Even though, intensity of peak one is constant for lower potentials, it starts to increase as potential reaches 60 V and increases even more for the 75 V sample. The intensity of peak two is constant for samples from 40 V to 60 V but it drastically decreases for the 75 V sample. Peak three exhibits a small intensity increment for samples obtained at 55 V and 60 V and a dramatic increase for 75 V sample.

The observed PL spectra agrees with the previously reported [158] for NAA samples anodized in oxalic acid. PL spectra were successfully decomposed in three Gaussian distributions with a fitting accuracy higher than 0.999. Some authors have found that NAA PL emerge from two [43,44,191,194,198,219] or three [215,227,234] excitation centers corresponding mainly to oxygen vacancies (F and F^{+}) and oxalate impurities incorporated into the NAA pore walls. The incorporation of oxalic impurities is generated during the competition between the water splitting reaction and the dissociation of acid into conjugate base anions that can partially replace O^{2-} ions in the aluminum oxide. Yamamoto [195], firstly proposed a model where the oxalate species incorporated during aluminum anodization in oxalic acid were mostly located in the outer region of the cell walls. The electric field distributions are higher in the pore base than in the cell base (See Figure 4.2) generating an electric charge concentration and admitting more electrolyte anions in the outer part of the pore wall.

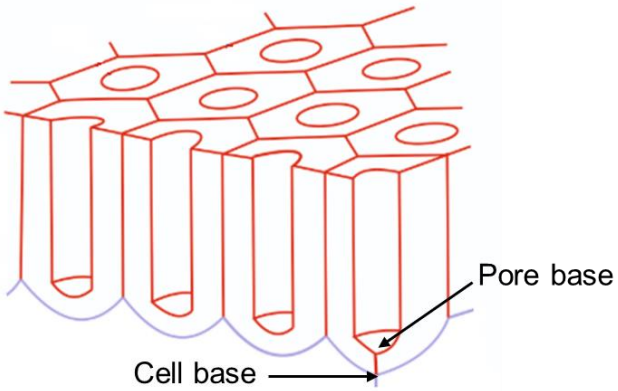

Figure 4.2 Graphic representation of the pore base and cell base.

From Figures 4.3 and 4.4 it can be observed the dependence of the PL properties of NAA on the anodizing potential. With the increase of anodization potential there is an increase in the current density involved in the process as shown in the inset of Figure 4.5a and it is expected that at higher current densities the larger the number of incorporated ions into the oxide. In chapter 3, each peak was assigned to an optical center based on pore widening and thickness evaluations. The peak of higher energy (420 nm) was assigned to the F^{+} center, the peak around 450 nm to the F center and the peak positioned at 490 nm to the incorporated oxalate impurities. The diminution of the intensity of peaks centered around 420 nm and 450 nm with potential and the intensity increment of the peak located around 490 nm with applied

anodization voltage agree with the peak assignment of chapter 3. Higher potential produces thicker barrier layer and thicker pore walls generating larger volume of NAA with incorporated impurities acting as optical centers and making the low energy peak to become more pronounced.

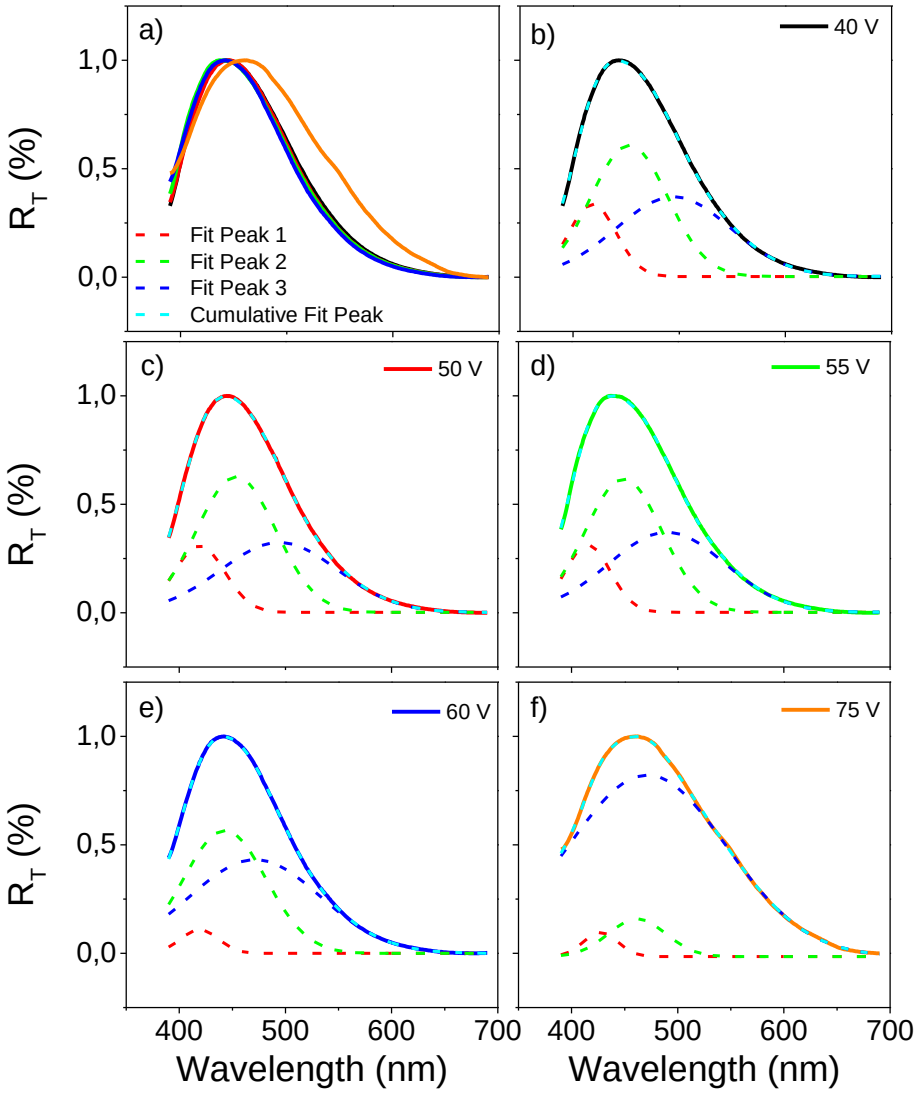

Figure 4.3 Deconvolution by Gaussian fitting of NAA PL spectra as function of anodizing potential (λ_{ex}=360 nm). a) all potentials, b) 40 V, c) 50 V, d) 55 V, e) 60 V and f) 75 V.

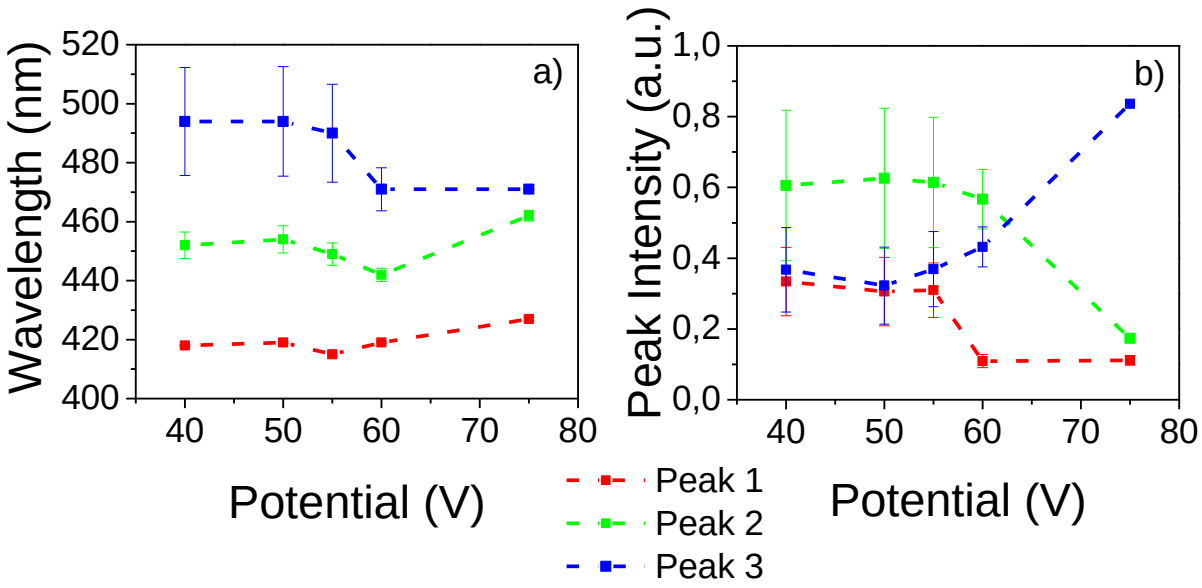

Figure 4.4 Effect of applied potential on PL peak position and intensity. a) Position of each deconvoluted PL peak vs anodizing potential and b) intensity of each deconvoluted PL peak anodizing potential.

The measured and simulated reflectance spectra of NAA anodized at different potentials are presented in Figure 4.5. The measured total reflectance (R_T) spectra from Figure 4.5a indicate that the Al/NAA behaves as a Fabry-Perot cavity where multiple reflections occur at two interfaces: The air/NAA and NAA/Al. The 40 V sample appears to have more fringes than the other samples. A reflectance drop is observed in the UV zone for all samples. The minimum reflectance is located around 300 nm and exhibits a red shift with anodizing potential. The 40 V sample appears to have one minimum around 300 nm and another one around 250 nm. The average reflectance diminishes as potential increases for the evaluated wavelengths. It is observed a pronunced absorption tail for the 60 V sample, starting around 600 nm. The amplitude of the fringes intensity diminishes with applied potential and is higher at longer wavelengths.

Figure 4.5b shows the simulated NAA reflectance spectra for samples anodized at distinct potentials. Simulations reproduced the behavior observed in the measured spectra; the spectra exhibit the Fabry-Pérot oscillations and the drop in reflectance is observed for shorter wavalengths. As anodized potential increases, the amplitude of the oscillations decreases, and the range of the spectrum where the oscillating behavior is observed, becomes smaller. It is also observed a red shift in the minimum reflectance with anodizing potential. Total reflectance at 200 nm is around 10% for all NAA evaluated potentials. The observed number of fringes is the same for all simulated conditions. The average reflectance is constant in the visible zone.

Including the absorption originated by three centers located at 200 nm, 250 nm and 295 nm and considering an increment in the intensity of the absorption centers with anodizing potential, it was possible to reproduce the anodizing potential effect observed in the measured reflectance. In the simulated spectra, the number of fringes is the same for all samples due to the samples were considered with equal thicknesses [13,235]. The higher number of fringes observed for the measured 40 V sample is caused due to the sample was probably thicker than the others increasing the number of reflected light inside of pores and the simultaneous decrease in light intensity governed by multiple reflections of the light [205]. The measured reflectance bahavor is reproduced in the UV zone with a red shif of the second munimum reflectance wavelength with anodizing potentital and 10% of reflectance at 200 nm. The simulated samples present almost the same average reflectance in the visible zone although the measured spectra exhibit lower reflectaneces for higher anodizing potentials apparently, the absorption tail becomes more pronunced with potential. This can be explained due to the lack of inclusion of absorption tails in the extintion coefficient model. Some authors have observed the appearance of band tails in NAA compared to the pure alumina are attributed to the existence of unoccupied defect states in the band gaps, which can be originated from the oxygen vacancies and oxalic impurities [201].

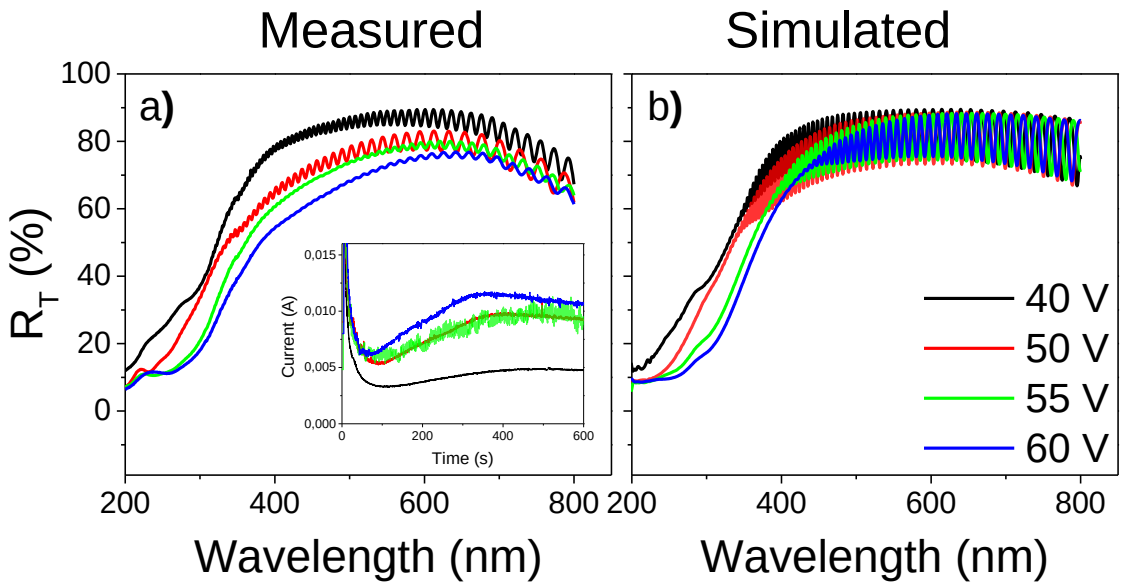

Figure 4.5 Measured and simulated UV-Vis reflectance spectra of Al/NAA. The NAA was obtained by anodization at 40 V, 50 V, 55 V and 60 V in 0.3 M oxalic acid. a) measured total reflectance (R_T) and b) modeled specular reflectance with effective medium approximation (E.M.A.) using NKDGen software. The inset corresponds to the anodization current vs time plot for each potential.

4.4.2 Optical properties of Al/NAA/TiO_2

Figure 4.6 shows top SEM images of NAA obtained by anodization at different potentials with 0, 4, 16 and 32 spayed TiO_2 layers corresponding to 18 nm, 88 nm and 196 nm of TiO_2 respectively. A zoom-in of the hexagonal pore cell is shown at the lower right of each image. From the SEM images on the left hand side of Figure 4.6 and Table 4.2 it is observed that pore diameter (d_p) and interpore distance (d_{int}) increase with anodization potential. The dependence of d_{int} with anodizing potential was studied before, indicating that d_{int} anodized in oxalic acid under mild anodization conditions is linearly dependent on the applied voltage [102,103] as well as d_p is directly proportional to voltage [103] supporting the observations of the increasing cell size (d_{int}) and d_p from the left images of Figure 4.6 and according to the reported values in Table 4.2.

It is also observed that pore diameter decreases with the number of TiO_2 layers until the NAA structure is completely occluded by the TiO_2. The TiO_2 is initially deposited at the most prominent parts of the pore wall (hexagon corners), then enters a few nanometers into the inner part of the pore wall until the TiO_2 completely coated the NAA pore. After coating the evaluated NAA samples with 18 nm of TiO_2 (4 layers) the ordered and porous structure is still observed for all NAA produced at different potentials and a smooth petal-like morphology is created by the TiO_2 [236]. After spraying 88 nm of TiO_2 a granular structure composed of small grains aggregated forming the petal-like morphology is observed. Thicker TiO_2 layers generate compact layers with some TiO_2 spherical aggregates forming bigger spheres of around 250 nm diameter for the 40V sample and 300 nm diameter for the 60 V sample. The 40V NAA sample with 4 TiO_2 layers has the same porosity than uncovered NAA, while for the 50 V NAA sample with 4 TiO_2 layers, this factor was reduced by one third as compared to the uncoated NAA. The porosity of samples produced at 55 V and 60 V with 4 TiO_2 layers was reduced by a half as compared to the uncoated ones.

The smooth morphology observed for the NAA samples coated with 4 TiO_2 layers is the product of having a thin TiO_2 layer, agreeing with Oja, I., et al. [237] whom observed that between spray pulses the film roughness increases with the number of spray pulses. The porosity reduction observed for samples anodized at 50 V or more is related to the d_p reduction and progressive occlusion. When the d_p of NAA is 33 nm (40 V sample) the droplet of TiO_2 is not able to enter into the pore and then it is located at the pore surroundings being the most prominent points of the NAA surface. On the contrary, $d_p \geq 43$ nm allows the TiO_2 to go inside the pore and spreads on its entrance; the droplet splashes onto the substrate and decomposes while the solvent is evaporated due to the sample is heated at 500 °C [179].

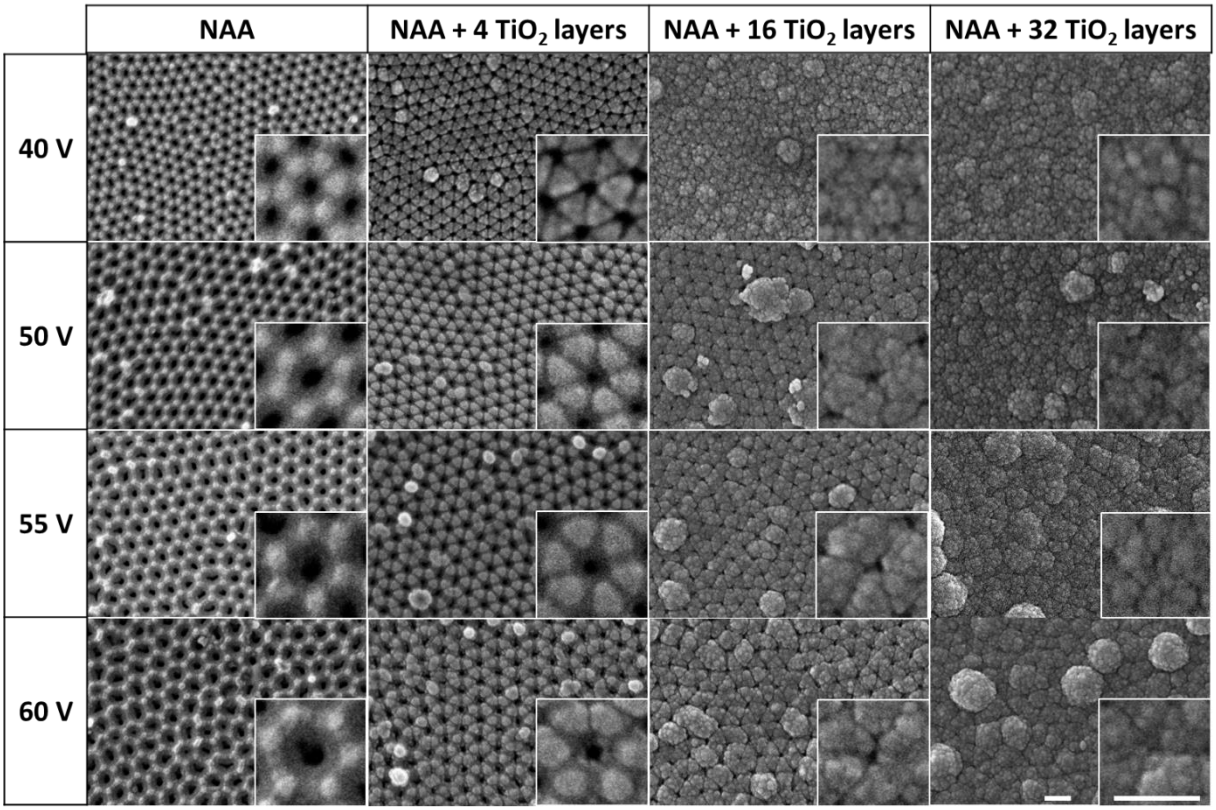

Figure 4.6 Top SEM images of 9 µm NAA obtained by anodization at 40 V, 50 V, 55 V and 60 V in 0.3 M oxalic acid with 0, 4, 16 and 32 spayed TiO_2 layers corresponding to an 18 nm, 88 nm and 196 nm of TiO_2. *The white bars in the lower right corresponds to 200 nm.*

Table 4.2 Pore diameter d_p, interpore distance d_{int} of NAA samples obtained at different anodization potentials.

Potential (V)	d_p (nm)	d_{int} (nm)	p_{NAA} calculated (%)	p_{NAA} measured (%)	Average p_{NAA} (%)
40	33 ± 6	112 ± 8	7.94	8.51	8.23
50	44 ± 11	130 ± 6	9.68	10.24	9.96
55	51 ± 17	140 ± 9	12.11	10.15	11.13
60	51 ± 17	154 ± 15	9.95	9.50	9.73

Figure 4.7 shows the measured and simulated reflectance for samples anodized at 40 V, 50 V, 55 V and 60 V, and coated with 18 nm (4 layers), 88 nm (16 layers) and 196 nm (32 layers) of TiO_2. It can be observed an oscillatory modulated behavior in the visible (Vis) and near infrared (NIR) ranges. The oscillations disappear in the ultraviolet (UV) range. The frequency of the modulations increases with TiO_2

thickness. The amplitude of the Fabry-Pérot oscillations is higher for samples with thicker TiO_2 coatings. A high and almost constant average reflectance is exhibited in the Vis and NIR ranges. In the UV range there is a drop in reflectance around 350 nm and the minimum point show a red shift with TiO_2 thickness. There is a slight increase in reflectance around 280 nm for all samples. From Figure 4.7a, c and g it is shown a small decrease in average reflectance in the Vis-NIR range with the increase of TiO_2 thickness for all samples except the 55 V sample (Figure 4.7e) where the 55 V sample with 32 TiO_2 layers was slightly more reflective than the sample 55 V with 16 TiO_2 layers.

The simulations on the right of Figure 4.7, reproduced the observed modulated oscillatory behavior. The simulated spectra follow the drop in reflectance around 350 nm and the red shift of that minimum point. The slight increase in reflectance observed around 270 nm for the measured spectra is also well reproduced. The number of modulations maxima and minima and the location is also properly replicated by the simulations. Although the amplitude of the oscillations is higher than in the measured spectra the other characteristics of the experimental data were correctly imitated by the simulations.

The observed modulations in the interference spectra of NAA correspond to a bi-layer system [217] where the interference is due to the air/TiO_2, TiO_2/NAA and NAA/Al interfaces and the increase in modulated behavior with TiO_2 thickness responds to the augmented number of possible reflections across TiO_2 thickness. The observed variation of the minimum reflectance value around 350 nm (3.44 eV) with thickness is related to the reported band-gap for sprayed TiO_2 thin films going from 3.37 to 3.75 eV depending on grain size and annealing temperature [30,182]. The differences between measured and simulated average R_T and amplitude of fringes are explained as simulations are performed considering ideal coatings but the fabricated samples present inhomogeneities and defects. The diminution in average reflectance with TiO_2 thickness observed for measured spectra can be associated with the fact that the thicker the film the higher the number of defects that serve as absorption centers and the lower amplitude of the fringes can be related to loses related to intrinsic defects in the fabricated samples. Additionally, from Figure 4.6 it can be observed the presence of clusters of TiO_2 particle agglomerates on top of NAA that increase in size with anodizing potential, these clusters can also act as absorption defects decreasing the measured reflectance.

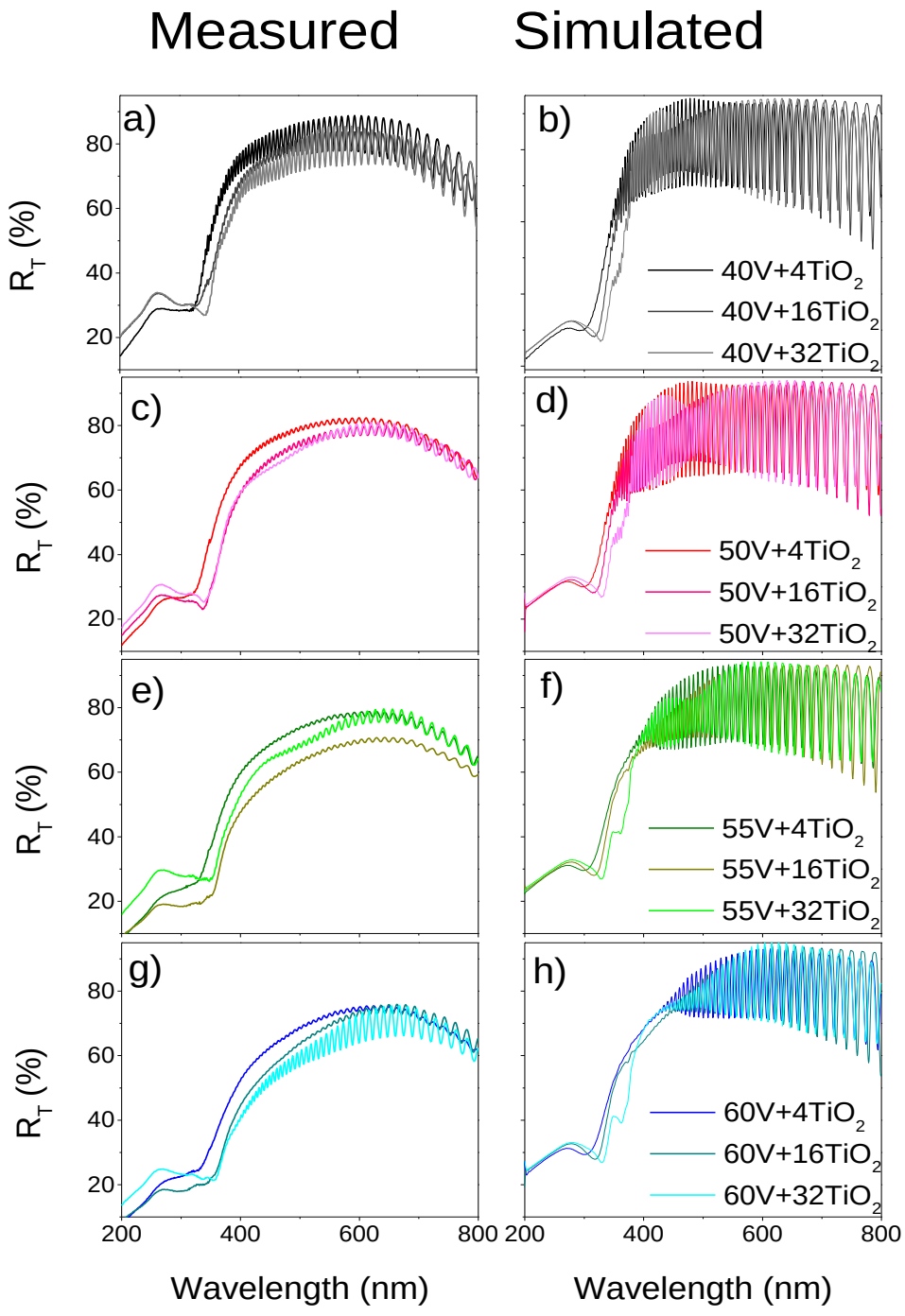

Figure 4.7 Measured and simulated UV-Vis reflectance spectra of Al/NAA/TiO_2. Images a, c, e and g correspond to the measured spectra, Images b, d, f and h represent modeled specular reflectance with E.M.A. including three absorption centers using NKDGen software.

4.5 Conclusions

The evaluation of the influence of anodizing potential on the optical behavior of Al/NAA was presented. Photoluminescence and reflectance measurements were carried out to understand the origin of absorption in NAA produced in oxalic acid. The reflectance of Al/NAA and Al/NAA/TiO_2 samples was modeled by using E.M.A. approximation considering three absorption centers into the model of the extinction coefficient.

It was found that the PL of NAA produced in oxalic acid originates from three absorption centers. Then, the PL spectra were deconvoluted in three Gaussian functions. Based on observations of PL spectra reported in chapter 3 and supported by the anodizing potential effect on PL peaks the three absorption centers were named. Higher potentials produce thicker barrier layers and thicker pore walls generating larger volume of NAA with incorporated impurities acting as optical centers and making the low energy peak to become more pronounced. The peak of higher energy (420 nm) was assigned to the F^+ center, the peak around 450 nm to the F center and the peak positioned at 490 nm to the incorporated oxalate impurities.

The UV absorption observed in NAA structures produced in oxalic acid was a key point to successfully reproduce the reflectance spectra with simulations. Including three absorptions centers into the extinction coefficient model (designated as F^+ center at 200 nm, F center at 250 nm and incorporated oxalate species at 295 nm) and considering an increment in the intensity of the absorption centers with anodizing potential the measured reflectance of NAA was correctly reproduced.

TiO_2 was successfully deposited on top of NAA using spray pyrolysis technique. It was observed that thinner TiO_2 coatings grew up preferentially on top of the hexagon edges creating a petal-like morphology and allowing pore diameter modulation. Thicker TiO_2 coatings completely occluded the NAA structure generating compact coatings with spherical morphology and the presence of particles agglomerates.

The spray of TiO_2 on top of NAA generated a modulated behavior in the Fabry-Pérot oscillations that can serve as amplifier of the fringes for sensing purposes. The simulations of Al/NAA/TiO_2 correctly reproduce the reflectance measurement in the evaluated UV/Vis/NIR range.

5. SUMMARY AND CONCLUSIONS

It was possible to modify and control the optical response of multilayer systems Al/NAA/TiO_2 by tuning the morphological characteristics of the NAA layer in the course of this research.

During this PhD thesis, some electropolishing conditions have been evaluated to find the most suitable pretreatment process for anodizing. Afterwards, several anodization conditions have been carried out in order to control the morphological characteristics of produced nanoporous anodic alumina (NAA) and relate them to the optical properties of NAA. Subsequently, bi-layered structures have been created by spraying titanium dioxide (TiO_2) on top of NAA, and the optical behavior has been studied as well.

First, several electropolishing processes were evaluated in order to obtain flat surfaces with low roughness values to be used as proper substrates to grow ordered NAA layers:

- Among the three evaluated electropolishing electrolytes and processes, the modified Brytal process generated smooth and flat surfaces.

- The electropolishing process should be preceded by an annealing treatment to increase the homogeneity of the surface.

Second, the effect of anodizing parameters on NAA morphology was studied:

- The anodization potential has a major effect on interpore distance (d_{int}) and NAA organization. The higher the potential the larger the d_{int}. As potential increases the well-organized NAA structure decreases, the potentials range studied was between 40 V and 75 V.

- Between the evaluated temperatures the lower one (5 °C) generated more organized NAA structures characterized by larger domains.

- The second anodization time controls the NAA thickness. Longer times produces thicker NAA samples, as it is well known.

Third, the effect of NAA thickness, pore diameter (d_p) and potential on optical properties of NAA and NAA/TiO_2 was evaluated:

- Pore diameter and anodizing potential had a major effect on reflectance (R) and photoluminescence (PL) spectra whereas thickness only had effect on R. Regarding to reflectance, increasing d_p decreases the number of fringes and their amplitude. Increasing the NAA thickness increases the number of fringes but decrease their amplitude. Increasing anodizing potential decreases the average reflectance, mainly in the UV range. Regarding to PL, increasing d_p (increasing the pore widening process) generated a blue shift in the PL peak position and increasing potential generated a slight red shift in the PL position.

- It was observed that thin TiO_2 layers increase the amplitude of the Fabry-Pérot fringes improving the possibilities to use this structures as sensing platforms. Thick TiO_2 layers generated a modulated oscillating behavior serving as interference coatings. The modulations can be controlled by TiO_2 thickness control. Thin TiO_2 coatings can be employed to modulate the range of NAA d_p.

- PL emission of NAA samples produced in oxalic acid was successfully deconvoluted into three Gaussian spectra. The location of the three peaks was around 420 nm, 455 nm and 490 nm attributed to doubly ionized oxygen vacancies F, singly ionized oxygen vacancies F^+ and oxalate impurities incorporated into the oxide layer respectively.

Fourth, the optical properties of NAA and NAA/TiO_2 were simulated:

- The NAA reflectance spectra were well reproduced by simulations when a non-zero extinction coefficient was introduced in the model. Consequently, the absorption in the ultra violet range observed in NAA produced in oxalic acid solutions is an important characteristic that should be considered for future simulations.

- Considering the effect of the three absorption centers in the model of the extinction coefficient a better fitting was achieved for all evaluated reflectance spectra of NAA.

- Based on PL and R measurements and R simulations it was observed that increasing NAA thickness increases the amount of absorption centers

decreasing the average R in the UV range. Increasing the d_p by pore widening processes dissolves the outer pore wall decreasing the luminescent centers and increasing the average R in the UV range. Increasing the anodizing potential increases d_p, and pore walls, decreasing the reflectance and enhancing the third peak of the PL spectra (490 nm).

The results presented on this thesis provide a starting point to fully understand the optical bahavior of nanoporous anodic alumina obtained in oxalic acid electrolyte. The identification of absorption centers and photoluminescent sites withdraw a path for developing new nanodevices for NAA use in optical and optoelectronic applications. Unveiling the absorption sites in NAA obtained in oxalic acid also gives valuable information to model and simulate more accurate multilayer structures including NAA.

Futhermore, the NAA surface modification by means of spraying titanium dioxide on top of it will be a starting point to create optical coatings considering what has been mentioned here regarding NAA morphological and optical changes obtained with each titanium dioxide coating layer. Bearing in mind the remarkable optical and electrical properties of TiO_2, the results reported here lead to explore the hydrophobic, hydrophilic, self-cleaning properties of the NAA/TiO_2 systems to improve and fabricate more precise and effective nanodevices.

References

[1] I.R. Durán, G. Laroche, Current trends, challenges, and perspectives of anti-fogging technology: Surface and material design, fabrication strategies, and beyond, Prog. Mater. Sci. 99 (2019) 106–186. doi:10.1016/j.pmatsci.2018.09.001.

[2] R.J. Martín-Palma, M. Kolle, Biomimetic photonic structures for optical sensing, Opt. Laser Technol. 109 (2019) 270–277. doi:https://doi.org/10.1016/j.optlastec.2018.07.079.

[3] A. Santos, J.H. Yoo, C.V. Rohatgi, T. Kumeria, Y. Wang, D. Losic, Realisation and advanced engineering of true optical rugate filters based on nanoporous anodic alumina by sinusoidal pulse anodisation, Nanoscale. 8 (2016) 1360–1373. doi:10.1039/C5NR05462A.

[4] Y. Fan, Dual-band perfect light absorber in visible region based on cylinder silicon resonator, Opt. - Int. J. Light Electron Opt. 179 (2019) 1084–1090. doi:10.1016/j.ijleo.2018.10.023.

[5] Qiang-Ma, W.J. Zhang, D.H. Ma, Z.Q. Fan, X.B. Ma, Z. Jiang, Optimal design of quadruple-layer antireflection coating structure for conversion efficiency enhancement in crystalline silicon solar cells, Optik (Stuttg). 177 (2018) 123–

130. doi:10.1016/j.ijleo.2017.12.024.

[6] G. Palai, A. Nayyar, R. Manikandan, B. Singh, Metamaterial based photonic structure: An alternate high performance antireflection coating for solar cell, Optik (Stuttg). 179 (2019) 740–743. doi:10.1016/j.ijleo.2018.10.216.

[7] C. Lin, S. Chen, Analysis of temporal broadening of isolated attosecond pulses induced by periodic Mo/Si multilayer mirrors reflection, Optik (Stuttg). 174 (2018) 489–496. doi:10.1016/j.ijleo.2018.08.076.

[8] K. Luo, S. Niu, D. Shah, A. Lonkar, Y. Liu, J. Ravichandran, Prediction of perovskite and other ternary oxide multilayers as mirrors for soft X-rays, Mater. Res. Bull. 98 (2018) 206–212. doi:10.1016/j.materresbull.2017.10.018.

[9] Z. Zhai, L. Zhang, X. Li, S. Xiao, Tunable terahertz broadband absorber based on a composite structure of graphene multilayer and silicon strip array, Opt. Commun. 431 (2019) 199–202. doi:10.1016/j.optcom.2018.09.017.

[10] F. Bertó-Roselló, E. Xifré-Pérez, J. Ferré-Borrull, L.F. Marsal, 3D-FDTD modelling of optical biosensing based on gold-coated nanoporous anodic alumina, Results Phys. 11 (2018) 1008–1014. doi:10.1016/j.rinp.2018.10.067.

[11] X. Yan, H. Li, X. Su, Review of optical sensors for pesticides, TrAC - Trends Anal. Chem. 103 (2018) 1–20. doi:10.1016/j.trac.2018.03.004.

[12] O.S. Heavens, Optical Properties of Thin Films, Reports Prog. Phys. 1 (2006) 297–323. doi:10.1002/0470021942.ch13.

[13] J.J. Ruíz-Pérez, G.-L. J M, M.D. A, M. E, Method for determining the optical constants of thin dielectric films with variable thickness using only their shrunk, J. Phys. D. Appl. Phys. 34 (2001) 2489–2496.

[14] J. Wang, C.-W. Wang, Y. Li, W.-M. Liu, Optical constants of anodic aluminum oxide films formed in oxalic acid solution, Thin Solid Films. 516 (2008) 7689–7694. doi:10.1016/j.tsf.2008.03.023.

[15] R.M. Bueno, Study of the optical constants determination of thin films: Dependence on theoretical assumptions, J. Vac. Sci. Technol. A Vacuum, Surfaces, Film. 13 (1995) 2378. doi:10.1116/1.579477.

[16] S.G. Tomlin, Optical reflection and transmission formulae for thin films, J. Phys. D. Appl. Phys. 1 (2002) 1667–1671. doi:10.1088/0022-3727/1/12/312.

[17] F. Francois, E. Ludovic, Optical properties of nanostructured thin films, Prog. Quantum Electron. 28 (2004) 89–112. doi:10.1016/j.optcom.2011.11.031.

[18] W. Huang, M. Yu, S. Cao, L. Wu, X. Shen, Y. Song, Fabrication of highly ordered porous anodic alumina films in 0.75 M oxalic acid solution without using nanoimprinting, Mater. Res. Bull. 111 (2019) 24–33. doi:10.1016/j.materresbull.2018.11.002.

[19] S.Y. Li, X.G. Xiang, B.H. Ma, X.D. Meng, Facile preparation of diverse alumina surface structures by anodization and superhydrophobic surfaces with tunable water droplet adhesion, J. Alloys Compd. 779 (2019) 219–228. doi:10.1016/j.jallcom.2018.11.222.

[20] S. Ateş, E. Baran, B. Yazıcı, The nanoporous anodic alumina oxide formed by two-step anodization, Thin Solid Films. 648 (2018) 94–102. doi:10.1016/j.tsf.2018.01.013.

[21] G. Rajeev, E. Xifre-Perez, B. Prieto Simon, A.J. Cowin, L.F. Marsal, N.H. Voelcker, A label-free optical biosensor based on nanoporous anodic alumina for tumour necrosis factor-alpha detection in chronic wounds, Sensors Actuators, B Chem. 257 (2018) 116–123. doi:10.1016/j.snb.2017.10.156.

[22] S. Abbasimofrad, M. Almasi Kashi, M. Noormohammadi, A. Ramazani, Tuning the optical properties of nanoporous anodic alumina photonic crystals by control of allowed voltage range via mixed acid concentration, J. Phys. Chem. Solids. (2018). doi:10.1016/j.jpcs.2018.01.022.

[23] U.K. Chime, F.I. Ezema, J. Marques-Hueso, Porosity and hole diameter tuning on nanoporous anodic aluminium oxide membranes by one-step anodization, Optik (Stuttg). 174 (2018) 558–562. doi:10.1016/j.ijleo.2018.08.109.

[24] L. Ye, Z. Wei-wei, D. Kai-ning, J. Zhe-jun-yu, L. Zong-xiao, L. Fei-zhou, Synthesis of “lotus root”-like mesoporous titanium dioxide and its effects on UV response to aconitine release, J. Alloys Compd. 777 (2019) 285–293.

[25] W. Wang, W. Zhao, K. Wang, L. Wang, X. Wang, S. Wang, C. Zhang, J. Bai, On hydrophilicity improvement of the porous anodic alumina film by hybrid nano/micro structuring, Appl. Surf. Sci. 416 (2017) 710–715. doi:10.1016/j.apsusc.2017.04.175.

[26] A. Bertuna, E. Comini, N. Poli, D. Zappa, G. Sberveglieri, Titanium Dioxide Nanostructures Chemical Sensor, Procedia Eng. 168 (2016) 313–316. doi:10.1016/j.proeng.2016.11.204.

[27] D. Li, S. Bulou, N. Gautier, S. Elisabeth, A. Goullet, M. Richard-plouet, P. Choquet, Nanostructure and photocatalytic properties of TiO 2 fi lms deposited at low temperature by pulsed PECVD, Appl. Surf. Sci. J. 466 (2019) 63–69. doi:10.1016/j.apsusc.2018.09.230.

[28] Y. Sheng, J. Yang, F. Wang, L. Liu, H. Liu, C. Yan, Z. Guo, Sol-gel synthesized hexagonal boron nitride / titania nanocomposites with enhanced photocatalytic activity, Appl. Surf. Sci. 465 (2019) 154–163. doi:10.1016/j.apsusc.2018.09.137.

[29] A.S. Mokrushin, E.P. Simonenko, N.P. Simonenko, K.T. Akkuleva, V. V Antipov, N. V Zaharova, A.A. Malygin, K.A. Bukunov, V.G. Sevastyanov, N.T. Kuznetsov, Nanostructure and photocatalytic properties of TiO2 films deposited at lowtemperature by pulsed PECVD, Appl. Surf. Sci. 463 (2019) 197–202. doi:10.1016/j.apsusc.2018.08.208.

[30] S. Dhanapandian, A. Arunachalam, C. Manoharan, Effect of deposition parameters on the properties of TiO2 thin films prepared by spray pyrolysis, J. Sol-Gel Sci. Technol. 77 (2016) 119–135. doi:10.1007/s10971-015-3836-8.

[31] H. Adelkhani, S. Nasoodi, A.H. Jafari, A study of the morphology and optical properties of electropolished aluminum in the Vis-IR region, Int. J. Electrochem. Sci. 4 (2009) 238–246.

[32] G. Yang, B. Wang, K. Tawfiq, H. Wei, S. Zhou, G. Chan, Electropolishing of surfaces : theory and applications, Surf. Eng. (2016) 1–18. doi:10.1080/02670844.2016.1198452.

[33] V. Palmieri, Fundamentals of Electrocheestry. The Electrolytic Polishing of metals . Application to Copper and Niobium, Science (80-.). (2003) 1–9.

[34] P.A. Jacquet, Electrolytic polishing of metallic surfaces, Met. Finish. May (1949) 48–54.

[35] T.P. Hoar, D. Mears, G. Rothewell, The Relationships Between Anodic Passivity, Brightening and Pitting, Corros. Sci. 5 (1965) 279–289.

[36] A. Chandra, On the Mechanism of Niobium Electropolishing, The Ohio State University, 2012. doi:10.1149/2.054211jes.

[37] O. Jessensky, F. Müller, U. Gösele, Self-organized formation of hexagonal pore arrays in anodic alumina, Appl. Phys. Lett. 72 (1998) 1173–1175. doi:10.1063/1.121004.

[38] S. Van Gils, S. Holten, E. Stijns, M. Vancaldenhoven, H. Terryn, L. Mattsson, Electropolishing of aluminium: Processing and assessment of visual appearance, Surf. Interface Anal. 35 (2003) 121–127. doi:10.1002/sia.1477.

[39] M.G. Holló, A new interpretation of the substructure of electropolished aluminium surfaces, Acta Metall. 8 (1960) 265–268.

[40] M. Bauccio, “ASM Metal Reference Book ASM International.” Materials Park, USA, Third Edit, 1993.

[41] S. Ono, M. Saito, H. Asoh, Self-Ordering of Anodic Porous Alumina Induced by Local Current Concentration: Burning, Electrochem. Solid-State Lett. 7 (2004) B21–B24. doi:10.1149/1.1738553.

[42] S. Ono, N. Masuko, The duplex structure of cell walls of porous anodic films formed on aluminum, Corros. Sci. 33 (1992) 503–507. doi:10.1016/0010-938X(92)90078-H.

[43] G.S. Huang, X.L. Wu, L.W. Yang, X.F. Shao, G.G. Siu, P.K. Chu, Dependence of blue-emitting property on nanopore geometrical structure in Al-based porous anodic alumina membranes, Appl. Phys. A Mater. Sci. Process. 81 (2005) 1345–1349. doi:10.1007/s00339-005-3321-2.

[44] G.S. Huang, X.L. Wu, Y.F. Mei, X.F. Shao, G.G. Siu, Strong blue emission from anodic alumina membranes with ordered nanopore array, J. Appl. Phys. 93 (2003) 582–585. doi:10.1063/1.1529075.

[45] T. Kumeria, M.M. Rahman, A. Santos, J. Ferré-Borrull, L.F. Marsal, D. Losic, Structural and optical nanoengineering of nanoporous anodic alumina rugate filters for real-time and label-free biosensing applications, Anal. Chem. 86 (2014) 1837–1844. doi:10.1021/ac500069f.

[46] X. Hu, Y.J. Pu, Z.Y. Ling, Y. Li, Coloring of aluminum using photonic crystals of porous alumina with electrodeposited Ag, Opt. Mater. (Amst). 32 (2009) 382–386. doi:10.1016/j.optmat.2009.09.009.

[47] H. Asoh, S. Ono, T. Hirose, M. Nakao, H. Masuda, Growth of anodic porous alumina with square cells, Electrochim. Acta. 48 (2003) 3171–3174. doi:10.1016/S0013-4686(03)00347-5.

[48] S. Ono, M. Saito, H. Asoh, Self-ordering of anodic porous alumina formed in organic acid electrolytes, Electrochim. Acta. 51 (2005) 827–833. doi:10.1016/j.electacta.2005.05.058.

[49] H. Asoh, K. Nishio, M. Nakao, T. Tamamura, H. Masuda, Conditions for Fabrication of Ideally Ordered Anodic Porous Alumina Using Pretextured Al,

J. Electrochem. Soc. 148 (2001) B152–B156. doi:10.1149/1.1355686.

[50] F. Rashidi, T. Masuda, H. Asoh, S. Ono, Metallographic effects of pure aluminum on properties of nanoporous anodic alumina (NPAA), Surf. Interface Anal. 45 (2013) 1490–1496. doi:10.1002/sia.5285.

[51] C. Chi, J.-H. Lee, I. Kim, H.-J. Oh, Effects of Annealing Treatment of Aluminum Substrate on Nanopore Arrangements in Anodic Alumina, J. Mater. Sci. Technol. 31 (2015) 751–758. doi:10.1016/j.jmst.2014.09.019.

[52] C.K. Chung, M.W. Liao, H.C. Chang, C.T. Lee, Effects of temperature and voltage mode on nanoporous anodic aluminum oxide films by one-step anodization, Thin Solid Films. 520 (2011) 1554–1558. doi:10.1016/j.tsf.2011.08.053.

[53] J. De Laet, H. Terryn, J. Vereecken, Development of an optical model for steady state porous anodic films on aluminium formed in phosphoric acid, Thin Solid Films. 320 (1998) 241–252. doi:10.1016/s0040-6090(97)00741-4.

[54] J. Ferré-Borrull, J. Pallarès, G. Macías, L.F. Marsal, Nanostructural engineering of nanoporous anodic alumina for biosensing applications, Materials (Basel). 7 (2014) 5225–5253. doi:10.3390/ma7075225.

[55] L.P. Hernández-Eguía, J. Ferré-Borrull, G. Macias, J. Pallarès, L.F. Marsal, Engineering optical properties of gold-coated nanoporous anodic alumina for biosensing., Nanoscale Res. Lett. 9 (2014) 414. doi:10.1186/1556-276X-9-414.

[56] Alfred A. Schilt, Perchloric Acid and Perchlorates, THE G. FREDERICK SMITH CHEMICAL COMPANY, DeKalb, Illinois, 1979.

[57] Davis Joseph, Aluminum and Aluminum Alloys, 1993.

[58] K.M. Alam, A.P. Singh, S.C. Bodepudi, S. Pramanik, Fabrication of hexagonally ordered nanopores in anodic alumina: An alternative pretreatment, Surf. Sci. 605 (2011) 441–449. doi:10.1016/j.susc.2010.11.015.

[59] P.G. Wernick, S., Pinner, R., Sheasby, The Surface Treatment and Finishing of Aluminum and its Alloys, in: ASM Int., Fifth edit, Great Britain, 1987: pp. 1–1273.

[60] J.E. Hatch, Aluminum: Properties and Physical Metallurgy, ASM International, 1984. doi:10.1361/appm1984p001.

[61] Wood W G, Metals Handbook, in: Suface Clean. Finish. Coat., Vol 5, American Society of Metals, Materials Park, Ohio, 1982.

[62] D. Mardare, G.I. Rusu, The influence of heat treatment on the optical properties of titanium oxide thin films, Mater. Lett. 56 (2002) 210–214. doi:10.1016/S0167-577X(02)00441-X.

[63] Baker Hugh, ASM Handbook Volume 3 - Alloy Phase Diagrams, ASM Handb. (1992) 500. doi:10.1007/BF02869318.

[64] R. Ambat, A.J. Davenport, G.M. Scamans, A. Afseth, Effect of iron-containing intermetallic particles on the corrosion behaviour of aluminium, Corros. Sci. 48 (2006) 3455–3471. doi:10.1016/j.corsci.2006.01.005.

[65] J. Namahoot, EFFECT OF DEFORMATION ON CORROSION OF Al-Mn ALLOYS, The University of Birmingham, 2004.

[66] ASM International Handbook Committee, Metals Handbook Vol 13 - Corrosion, ninth, ASM International, USA, 1992. http://scholar.google.com/scholar?hl=en&btnG=Search&q=intitle:Metals+Handbook.+Volume+13:+Corrosion#0%5Cnhttp://scholar.google.com/scholar?hl=en&btnG=Search&q=intitle:Metals+Handbook.+Vol.+13:+Corrosion%230.

[67] Asm International, Heat Treating, Vol. 4, ninth, 1991.

[68] J.G. Kaufman, E.L. Rooy, Aluminum Alloy Castings Properties, Processes, and Applications, ASM International, United States of America, 2004.

[69] Lunn George, Sansone Eric, Destruction of Hazardous Chemicals in the Laboratory, Third, Wiley, United States of America, 2012.

[70] R.B.C. Cayless, Alloy and Temper Designation Systems for Aluminum and Aluminum Alloys, in: A.I.H. Committee (Ed.), ASM Handb. Vol. 2 Prop. Sel. Nonferrous Alloy. Spec. Mater., ASM International, United States of America, 1992: pp. 25–95.

[71] G. Hass, N.W. Scott, On the structure and properties of some metal and metal oxide films, J. Phys. Le Radium. 11 (1950) 394–402. doi:10.1051/jphysrad:01950001107039400.

[72] F. Eozenou, C. Antoine, A. Aspart, S. Berry, J.F. Denis, B. Malki, Efficiency of Electropolishing Versus Bath Composition and Aging : First Results, (2005) 2–5.

[73] M. Buhlert, M. Gartner, M. Modreanu, A. Jitianu, R. Gavrila, A. Awad, P.J. Plath, Characterization of electropolished aluminum surfaces, Galvanotechnik. 95 (2004) 1629–1634+iv.

[74] R. Pinner, Electroplating and Metal Finishing, Electroplat. Met. Finish. 6 (1953) 401–410.

[75] C.F. Mallinson, P.M. Yates, M.A. Baker, J.E. Castle, A. Harvey, J.F. Watts, The localised corrosion associated with individual second phase particles in AA7075-T6: A study by SEM, EDX, AES, SKPFM and FIB-SEM, Mater. Corros. (2017) 1–16. doi:10.1002/maco.201609312.

[76] S. mei Li, Y. dong Li, Y. Zhang, J. hua Liu, M. Yu, Effect of intermetallic phases on the anodic oxidation and corrosion of 5A06 aluminum alloy, Int. J. Miner. Metall. Mater. 22 (2015) 167–174. doi:10.1007/s12613-015-1057-3.

[77] O. Lunder, K. Nisancioglu, Effect of Alkaline-Etch Pretreatment on the Pitting Corrosion of Wrought Aluminum., Corrosion. 44 (1988) 414–422. doi:10.5006/1.3583956.

[78] B. Wielage, D. Nickel, G. Alisch, H. Podlesak, T. Lampke, Effects of pre-treatment on the growth rate and morphology of hard anodic films on aluminium (EN AW-6082), Surf. Coatings Technol. 202 (2007) 569–576. doi:10.1016/j.surfcoat.2007.06.052.

[79] Z. Szklarska-Smialowska, Pitting corrosion of aluminum, Corros. Sci. 41 (1999) 1743–1767.

[80] I. Son, H. Nakano, S. Oue, S. Kobayashi, H. Fukushima, Z. Horita, Effect of equal-channel angular pressing on pitting corrosion of pure aluminum, Int. J. Corros. 2012 (2012) 1–9. doi:10.1155/2012/450854.

[81] S.J. Garcia-Vergara, P. Skeldon, G.E. Thompson, P. Bailey, T.C.Q. Noakes, H. Habazaki, K. Shimizu, Morphology of enriched alloy layers in an anodized Al-Cu alloy, Appl. Surf. Sci. 205 (2002) 121–127. doi:10.1016/S0169-4332(02)01040-1.

[82] Y. Osawa, S. Takamori, T. Kimura, K. Minagawa, H. Kakisawa, Morphology of Intermetallic Compounds in Al-Si-Fe Alloy and Its Control by Ultrasonic Vibration, Mater. Trans. 48 (2007) 2467–2475. doi:10.2320/matertrans.F-MRA2007874.

[83] J.A. Taylor, Iron-Containing Intermetallic Phases in Al-Si Based Casting Alloys, Procedia Mater. Sci. 1 (2012) 19–33. doi:10.1016/j.mspro.2012.06.004.

[84] G. Ghosh, Aluminium – Iron – Silicon, in: G. Effenberg, S. Ilyenko (Eds.), Iron Syst. Part 1, Landolt-Börnstein, 2006. doi:10.1007/978-3-540-69761-9_11.

[85] Davis Joseph, Corrosion of Aluminum and Aluminum Alloys, ASM International, Ohio, 1999.

[86] I. Boukerche, S. Djerad, L. Benmansour, L. Tifouti, K. Saleh, Degradability of aluminum in acidic and alkaline solutions, Corros. Sci. 78 (2014) 343–352. doi:10.1016/j.corsci.2013.10.019.

[87] TOTTEN George E. MACKENZIE D. Scott, Handbook of aluminum: Vol. 1: physical metallurgy and processes, first, CRC Press, 2003.

[88] N.A. Belov, A.A. Aksenov, D.G. Eskin, Iron in Aluminium Alloys: Impurity and Alloying Element, in: J.N. Fridlyander, D.G. Eskin (Eds.), Adv. Met. Alloy., Taylor and Francis, London and New York, 2002.

[89] A.M. Abd-Elnaiem, A. Gaber, Parametric study on the anodization of pure aluminum thin film used in fabricating nano-pores template, Int. J. Electrochem. Sci. 8 (2013) 9741–9751.

[90] J.-J. Zhang, Z. Li, Z. Zhang, T. Wu, H. Sun, Optical and magnetic properties of porous anodic alumina/Ni nanocomposite films, J. Appl. Phys. 113 (2013) 244305. doi:10.1063/1.4812466.

[91] C.T. Wu, C.H. Lin, C. Cheng, C.S. Wu, H.C. Ting, F.C. Chang, F.H. Ko, Design of artificial hollow moth-eye structures using anodic nanocones for high-performance optics, Chem. Mater. 22 (2010) 6583–6589. doi:10.1021/cm102408d.

[92] A. Santos, T. Kumeria, Nanoporous Anodic Alumina for Optical Biosensing, in: Nanoporous Alumina, Springer International Publishing, Switzerland, 2015. doi:10.1007/978-3-319-20334-8.

[93] P.E. Petrochenko, G. Kumar, W. Fu, Q. Zhang, J. Zheng, C. Liang, P.L. Goering, R.J. Narayan, Nanoporous aluminum oxide membranes coated with atomic layer deposition-grown titanium dioxide for biomedical applications: An in vitro evaluation, J. Biomed. Nanotechnol. 11 (2015) 2275–2285. doi:10.1166/jbn.2015.2169.

[94] M. Singh, D. Gobind, Highly ordered anodic porous alumina membrane and its surface modification approaches for biomedical application, IOSR J. Appl. Chem. 7 (2014) 17–34. doi:10.9790/5736-07111734.

[95] P. Banerjee, I. Perez, L. Henn-Lecordier, S.B. Lee, G.W. Rubloff, Nanotubular

metal-insulator-metal capacitor arrays for energy storage, Nat. Nanotechnol. 4 (2009) 292–296. doi:10.1038/nnano.2009.37.

[96] S. Sukarno, C.S. Law, A. Santos, Realisation and optical engineering of linear variable bandpass filters in nanoporous anodic alumina photonic crystals, Nanoscale. (2017). doi:10.1039/C7NR02115A.

[97] P.C. Stair, C. Marshall, G. Xiong, H. Feng, M.J. Pellin, J.W. Elam, L. Curtiss, L. Iton, H. Kung, M. Kung, H.H. Wang, Novel, uniform nanostructured catalytic membranes, Top. Catal. 39 (2006) 181–186. doi:10.1007/s11244-006-0055-0.

[98] A. Mutalib, J. Zhou, M.R. Nussio, D. Losic, J.G. Shapter, N.H. Voelcker, Pore spanning lipid bilayers on silanised nanoporous alumina membranes, in: Proc. SPIE, 2008: pp. 1–10. doi:10.1117/12.808769.

[99] Y. Chen, A. Santos, Y. Wang, T. Kumeria, J. Li, C. Wang, D. Losic, Biomimetic Nanoporous Anodic Alumina Distributed Bragg Reflectors in the Form of Films and Microsized Particles for Sensing Applications, ACS Appl. Mater. Interfaces. 7 (2015) 19816–19824. doi:10.1021/acsami.5b05904.

[100] M. Porta-i-Batalla, C. Eckstein, E. Xifré-Pérez, P. Formentín, J. Ferré-Borrull, L.F. Marsal, Sustained, Controlled and Stimuli-Responsive Drug Release Systems Based on Nanoporous Anodic Alumina with Layer-by-Layer Polyelectrolyte, Nanoscale Res. Lett. 11 (2016) 1–9. doi:10.1186/s11671-016-1585-4.

[101] H. Masuda, F. Hasegwa, S. Ono, Self-Ordering of Cell Arrangement of Anodic Porous Alumina Formed in Sulfuric Acid Solution, J. Electrochem. Soc. 144 (1997) L127. doi:10.1149/1.1837634.

[102] F. Keller, M.S. Hunter, D.L. Robinson, Structural Features of Oxide Coatings on Aluminum, J. Electrochem. Soc. 100 (1953) 411–419. doi:10.1149/1.2781142.

[103] J.P. O'Sullivan, G.C. Wood, The morphology and mechanism of formation of porous anodic films on aluminium, Proc. R. Soc. London. 317 (1970) 511–543. doi:10.1098/rspa.1970.0129.

[104] H. Masuda, K. Fukuda, Ordered metal nanohole arrays made by a two-step replication of honeycomb structures of anodic alumina., Science (80-.). 268 (1995) 1466–1468. doi:10.1126/science.268.5216.1466.

[105] H. Masuda, K. Yada, A. Osaka, Self-Ordering of Cell Configuration of Anodic Porous Alumina with Large-Size Pores in Phosphoric Acid Solution Self-Ordering of Cell Configuration of Anodic Porous Alumina with Large-Size Pores in Phosphoric Acid Solution, J. Appl. Phys. 37 (1998) 1340–1342. doi:10.1143/JJAP.37.L1340.

[106] O. Jessensky, F. Müller, U. Gösele, F. Muller, U. Gösele, Self−Organized Formation of Hexagonal Pore Structures in Anodic Alumina, J. Electrochem. Soc. 145 (1998) 3735–3740. doi:10.1149/1.1838867.

[107] K. Nielsch, J. Choi, K. Schwirn, R.B. Wehrspohn, U. Gösele, Self-ordering Regimes of Porous Alumina: The 10 Porosity Rule, Nano Lett. 2 (2002) 677–680. doi:10.1021/nl025537k.

[108] G.D. Sulka, K.G. Parkoła, Temperature influence on well-ordered nanopore

structures grown by anodization of aluminium in sulphuric acid, Electrochim. Acta. 52 (2007) 1880–1888. doi:10.1016/j.electacta.2006.07.053.

[109] O. Nishinaga, T. Kikuchi, S. Natsui, R.O. Suzuki, Rapid fabrication of self-ordered porous alumina with 10-/sub-10-nm-scale nanostructures by selenic acid anodizing., Sci. Rep. 3 (2013) 2748. doi:10.1038/srep02748.

[110] S. Ono, M. Saito, M. Ishiguro, H. Asoh, Controlling Factor of Self-Ordering of Anodic Porous Alumina, J. Electrochem. Soc. 151 (2004) B473. doi:10.1149/1.1767838.

[111] W. Lee, R. Ji, U. Gösele, K. Nielsch, Fast fabrication of long-range ordered porous alumina membranes by hard anodization, Nat. Mater. 5 (2006) 741–747. doi:10.1038/nmat1717.

[112] J. Li, Z. Zhang, Y. Li, Y. Ma, L. Chen, Z. Zhang, R. Sun, Self-Organization Process of Aluminum Oxide during Hard Anodization, Electrochim. Acta. 213 (2016) 14–20. doi:10.1016/j.electacta.2016.06.044.

[113] B. Sellarajan, M. Sharma, S.K. Ghosh, H.S. Nagaraja, H.C. Barshilia, P. Chowdhury, Effect of electrolyte temperature on the formation of highly ordered nanoporous alumina template, Microporous Mesoporous Mater. 224 (2016) 262–270. doi:10.1016/j.micromeso.2015.12.045.

[114] M.A. Kashi, A. Ramazani, The effect of temperature and concentration on the self-organized pore formation in anodic alumina, J. Phys. D. Appl. Phys. 38 (2005) 2396–2399. doi:10.1088/0022-3727/38/14/015.

[115] L. Zaraska, A. Brudzisz, E. Wierzbicka, G.D. Sulka, The effect of electrolyte change on the morphology and degree of nanopore order of porous alumina formed by two-step anodization, Electrochim. Acta. 198 (2016) 259–267. doi:10.1016/j.electacta.2016.03.050.

[116] W. Lee, S.-J.S.S. Park, Porous anodic aluminum oxide: anodization and templated synthesis of functional nanostructures, Chem. Rev. 114 (2014) 7487–7556. doi:10.1021/cr500002z.

[117] X.Z. Liu, M.X. Xu, Y.M. Tian, M. Shang, P. Zhang, Regularity control of porous anodic alumina and photodegradation activity of highly ordered titania nanostructures, Trans. Nonferrous Met. Soc. China (English Ed. 16 (2006). doi:10.1016/S1003-6326(06)60206-9.

[118] W. Ce, T. S, S. K, S. T, S. S, Fabrication of Ordered Arrays of Anodic Aluminum Oxide Pores with Interpore Distance Smaller than the Pitch of Nano-pits formed by Ion Beam Etching, J. Mater. Sci. Nanotechnol. 1 (2014) 1–6. doi:10.15744/2348-9812.1.S105.

[119] M. Michalska-Domańska, M. Norek, W.J. Stepniowski, B. Budner, Fabrication of high quality anodic aluminum oxide (AAO) on low purity aluminum - A comparative study with the AAO produced on high purity aluminum, Electrochim. Acta. 105 (2013) 424–432. doi:10.1016/j.electacta.2013.04.160.

[120] L. Zaraska, W.J. Stępniowski, M. Jaskuła, G.D. Sulka, Analysis of nanopore arrangement of porous alumina layers formed by anodizing in oxalic acid at relatively high temperatures, Appl. Surf. Sci. 305 (2014) 650–657. doi:10.1016/j.apsusc.2014.03.154.

[121] R.A.V. Wojciech J. Stępniowskia, Agata Nowak-Stępniowskab, Adam Preszc,

Tomasz Czujkoa, The effects of time and temperature on the arrangement of anodic aluminum oxide nanopores, Mater. Charact. 91 (2014) 1–9.

[122] C. Toccafondi, W.J. Stępniowski, M. Leoncini, M. Salerno, Advanced morphological analysis of patterns of thin anodic porous alumina-supplementary info, Mater. Charact. 94 (2014) 26–36. doi:10.1016/j.matchar.2014.05.003.

[123] W.J. Stępniowski, M. Michalska-Domańska, M. Norek, T. Czujko, Fast Fourier transform based arrangement analysis of poorly organized alumina nanopores formed via self-organized anodization in chromic acid, Mater. Lett. 117 (2014) 69–73. doi:10.1016/j.matlet.2013.11.099.

[124] A.M. Abd-Elnaiem, A.M. Mebed, W.J. Stępniowski, T. Czujko, Characterization of arrangement and geometry of porous anodic alumina formed by one-step anodization of Al-1 wt% Si thin films, Surf. Coatings Technol. 307 (2016) 359–365. doi:10.1016/j.surfcoat.2016.09.013.

[125] W.J. Stępniowski, T. Durejko, M. Michalska-Domańska, M. Łazińska, J. Aniszewska, Characterization of nanoporous anodic aluminum oxide formed on laser pre-treated aluminum, Mater. Charact. 122 (2016) 130–136. doi:10.1016/j.matchar.2016.10.034.

[126] C.A. Schneider, W.S. Rasband, K.W. Eliceiri, NIH Image to ImageJ: 25 years of image analysis, Nat. Methods. 9 (2012) 671–675. doi:10.1038/nmeth.2089.

[127] I. Horcas, R. Fernandez, J.M. Gomez-Rodriguez, J. Colchero, J. Gomez-Herrero, A.M. Baro, Review of Scientific Instruments 78, 01375, (2007).

[128] L.E. Fratila-Apachitei, F.D. Tichelaar, G.E. Thompson, H. Terryn, P. Skeldon, J. Duszczyk, L. Katgerman, A transmission electron microscopy study of hard anodic oxide layers on AlSi(Cu) alloys, Electrochim. Acta. 49 (2004) 3169–3177. doi:10.1016/j.electacta.2004.02.030.

[129] L.E. Fratila-Apachitei, H. Terryn, P. Skeldon, G.E. Thompson, J. Duszczyk, L. Katgerman, Influence of substrate microstructure on the growth of anodic oxide layers, Electrochim. Acta. 49 (2004) 1127–1140. doi:10.1016/j.electacta.2003.10.024.

[130] K. Shimizu, G.M. Brown, K. Kobayashi, P. Skeldon, G.E. Thompson, G.C. Wood, Ultramicrotomy-a route towards the enhanced understanding of the corrosion and filming behaviour of aluminium and its alloys, Corros. Sci. 40 (1998) 1049–1072. doi:10.1016/S0010-938X(98)00006-7.

[131] X.Y. Han, W.Z. Shen, Improved two-step anodization technique for ordered porous anodic aluminum membranes, J. Electroanal. Chem. 655 (2011) 56–64. doi:10.1016/j.jelechem.2011.02.008.

[132] Q.W. Sun, G.Q. Ding, Y.B. Li, M.J. Zheng, W.Z. Shen, Tip-like anodic alumina, Nanotechnology. 18 (2007). doi:10.1088/0957-4484/18/21/215304.

[133] F. Li, L. Zhang, R. Metzger, On the growth of highly ordered pores in anodized aluminum oxide, Chem. Mater. 10 (1998) 2470–2480. doi:10.1021/cm980163a.

[134] W.J. Stępniowski, Z. Bojar, Synthesis of anodic aluminum oxide (AAO) at relatively high temperatures. Study of the influence of anodization conditions on the alumina satructural features, Surf. Coatings Technol. 206 (2011) 265–

272.

[135] G.D. Sulka, W.J. Stepniowski, Structural features of self-organized nanopore arrays formed by anodization of aluminum in oxalic acid at relatively high temperatures, Electrochim. Acta. 54 (2009) 3683–3691. doi:10.1016/j.electacta.2009.01.046.

[136] W.J. Stępniowski, Z. Bojar, Synthesis of anodic aluminum oxide (AAO) at relatively high temperatures. Study of the influence of anodization conditions on the alumina structural features, Surf. Coatings Technol. 206 (2011) 265–272. doi:10.1016/j.surfcoat.2011.07.020.

[137] W.J. Stepniowski, A. Nowak-Stepniowska, Z. Bojar, Quantitative arrangement analysis of anodic alumina formed by short anodizations in oxalic acid, Mater. Charact. 78 (2013) 79–86. doi:10.1016/j.matchar.2013.01.013.

[138] G.D. Sulka, Highly Ordered Anodic Porous Alumina Formation by Self-Organized Anodizing, in: Nanostructured Mater. Electrochem., 2008: pp. 1–116. doi:10.1002/9783527621507.ch1.

[139] D. Losic, A. Santos, Electrochemically Engineered Nanoporous Materials: Methods, Properties and Applications, 2015. doi:10.1007/978-3-319-20346-1.

[140] Y. Lei, W. Cai, G. Wilde, Highly ordered nanostructures with tunable size, shape and properties: A new way to surface nano-patterning using ultra-thin alumina masks, Prog. Mater. Sci. 52 (2007) 465–539. doi:10.1016/j.pmatsci.2006.07.002.

[141] J. Liu, S. Liu, H. Zhou, C. Xie, Z. Huang, C. Fu, Y. Kuang, Preparation of self-ordered nanoporous anodic aluminum oxide membranes by combination of hard anodization and mild anodization, Thin Solid Films. 552 (2014) 75–81. doi:10.1016/j.tsf.2013.12.023.

[142] X. Sheng, J. Liu, N. Coronel, A.M. Agarwal, J. Michel, L.C. Kimerling, Integration of self-assembled porous alumina and distributed bragg reflector for light trapping in Si photovoltaic devices, IEEE Photonics Technol. Lett. 22 (2010) 1394–1396. doi:10.1109/LPT.2010.2060717.

[143] J. Diggle, T. Downie, C. Goulding, Anodic Oxide Films on Aluminum, Chem. Rev. 69 (1969) 365–405. doi:10.1021/cr60259a005.

[144] A. Santos, T. Pereira, C.S. Law, D. Losic, Rational Engineering of Nanoporous Anodic Alumina Optical Bandpass Filters, Nanoscale. 8 (2016) 14846–14857. doi:10.1039/C6NR03490J.

[145] À. Ribes, E. Xifré -Pérez, E. Aznar, F. Sancenón, T. Pardo, L.F. Marsal, R. Martínez-Máñez, Molecular gated nanoporous anodic alumina for the detection of cocaine, Sci. Rep. 6 (2016) 1–9. doi:10.1038/srep38649.

[146] C.S. Law, G.M. Sylvia, M. Nemati, J. Yu, D. Losic, A.D. Abell, A. Santos, Engineering of Surface Chemistry for Enhanced Sensitivity in Nanoporous Interferometric Sensing Platforms, ACS Appl. Mater. Interfaces. 9 (2017) 8929–8940. doi:10.1021/acsami.7b01116.

[147] C.S. Law, A. Santos, M. Nemati, D. Losic, Structural Engineering of Nanoporous Anodic Alumina Photonic Crystals by Sawtooth-like Pulse Anodization, ACS Appl. Mater. Interfaces. 8 (2016) 13542–13554. doi:10.1021/acsami.6b03900.

[148] A. Santos, T. Kumeria, D. Losic, Nanoporous anodic alumina: A versatile platform for optical biosensors, Materials (Basel). 7 (2014) 4297–4320. doi:10.3390/ma7064297.

[149] A. Santos, T. Kumeria, D. Losic, Nanoporous anodic aluminum oxide for chemical sensing and biosensors, TrAC - Trends Anal. Chem. 44 (2013) 25–38. doi:10.1016/j.trac.2012.11.007.

[150] T. Kumeria, A. Santos, Sensing and Biosensing Applications of Nanoporous Anodic Alumina, in: Electrochem. Eng. Nanoporous Mater., Springer International Publishing, Switzerland, 2015: pp. 187–218. doi:10.1007/978-3-319-20346-1.

[151] A. Santos, V.S. Balderrama, M. Alba, P. Formentín, J. Ferré-Borrull, J. Pallarès, L.F. Marsal, Tunable Fabry-Pérot interferometer based on nanoporous anodic alumina for optical biosensing purposes, Nanoscale Res. Lett. 7 (2012) 370. doi:10.1186/1556-276X-7-370.

[152] J. Wang, A.-H. Lu, M. Li, W. Zhang, Y.-S. Chen, D.-X. Tian, W.-C. Li, Thin porous alumina sheets as supports for stabilizing gold nanoparticles, ACS Nano. 7 (2013) 4902–4910. doi:10.1021/nn401446p.

[153] F. Le Coz, L. Arurault, S. Fontorbes, V. Vilar, L. Datas, P. Winterton, Chemical composition and structural changes of porous templates obtained by anodising aluminium in phosphoric acid electrolyte, Surf. Interface Anal. 42 (2010) 227–233. doi:10.1002/sia.3199.

[154] C.T. Sousa, D.C. Leitao, M.P. Proenca, J. Ventura, A.M. Pereira, J.P. Araujo, Nanoporous alumina as templates for multifunctional applications, Appl. Phys. Rev. 1 (2014) 031102. doi:10.1063/1.4893546.

[155] Z. Wu, Y. Zhang, K. Du, A simple and efficient combined AC-DC electrodeposition method for fabrication of highly ordered Au nanowires in AAO template, Appl. Surf. Sci. 265 (2013) 149–156. doi:10.1016/j.apsusc.2012.10.154.

[156] J. Vanpaemel, A.M. Abd-Elnaiem, S. De Gendt, P.M. Vereecken, The formation mechanism of 3D porous anodized aluminum oxide templates from an aluminum film with copper impurities, J. Phys. Chem. C. 119 (2015) 2105–2112. doi:10.1021/jp508142m.

[157] A. Santos, J. Ferré-Borrull, J. Pallarès, L.F. Marsal, Hierarchical nanoporous anodic alumina templates by asymmetric two-step anodization, Phys. Status Solidi Appl. Mater. Sci. 208 (2011) 668–674. doi:10.1002/pssa.201026435.

[158] A. Brz, A. Brudzisz, K. Hnida, Sulka, Chemical and Structural Modifications of Nanoporous Alumina and Its Optical Properties, in: Electrochem. Eng. Nanoporous Mater., 2015: pp. 30–59. doi:10.1007/978-3-319-20346-1.

[159] G.E. Thompson, Porous anodic alumina: fabrication, characterization and applications, Thin Solid Films. 297 (1997) 192–201. doi:10.1016/S0040-6090(96)09440-0.

[160] L. Vojkuvka, L.F. Marsal, J. Ferré-Borrull, P. Formentin, J. Pallarés, Self-ordered porous alumina membranes with large lattice constant fabricated by hard anodization, Superlattices Microstruct. 44 (2008) 577–582. doi:10.1016/j.spmi.2007.10.005.

[161] L. Gelde, A. Cuevas, M. Martínez de Yuso, J. Benavente, V. Vega, A. González, V. Prida, B. Hernando, Influence of TiO2-Coating Layer on Nanoporous Alumina Membranes by ALD Technique, Coatings. 8 (2018) 60. doi:10.3390/coatings8020060.

[162] A.M. Md Jani, D. Losic, N.H. Voelcker, Nanoporous anodic aluminium oxide: Advances in surface engineering and emerging applications, Prog. Mater. Sci. 58 (2013) 636–704. doi:10.1016/j.pmatsci.2013.01.002.

[163] J. Ferré-Borrull, J. Pallarès, G. Macías, L.F. Marsal, Nanostructural engineering of nanoporous anodic alumina for biosensing applications, Materials (Basel). 7 (2014) 5225–5253. doi:10.3390/ma7075225.

[164] L. Cecchetto, C. Millon, D. Riassetto, M. Langlet, Study of Al2O3/TiO2 reflectivity enhancing bi-layer films on bright aluminium substrates, Appl. Surf. Sci. 254 (2008) 1604–1607. doi:10.1016/j.apsusc.2007.07.073.

[165] Y.J. Xu, J.X. Liao, Q.W. Cai, X.X. Yang, Preparation of a highly-reflective TiO2/SiO2/Ag thin film with self-cleaning properties by magnetron sputtering for solar front reflectors, Sol. Energy Mater. Sol. Cells. 113 (2013) 7–12. doi:10.1016/j.solmat.2013.01.034.

[166] V.C. Gudla, V.E. Johansen, S. Canulescu, J. Schou, R. Ambat, Simulation of reflectance from white-anodised aluminium surfaces using polyurethane-TiO2 composite coatings, J. Mater. Sci. 50 (2015) 4565–4575. doi:10.1007/s10853-015-9005-1.

[167] H.N. Umh, S. Yu, Y.H. Kim, S.Y. Lee, J. Yi, Tuning the Structural Color of a 2D Photonic Crystal Using a Bowl- like Nanostructure, (2016) 2–8. doi:10.1021/acsami.6b03717.

[168] X. Liu, Y. Tong, J. Chen, Surface Curing and Properties of Titanium Dioxide Self - Cleaning Ceramics, Ceram. Sci. Eng. 1 (2018) 1–6.

[169] R. Wang, K. Hashimoto, A. Fujishima, M. Chikuni, E. Kojima, A. Kitamura, M. Shimohigoshi, Toshiya Watanabe, Light-induced amphiphilic surfaces, Nature. 388 (1997) 431–432.

[170] M. Wang, G. Yang, P. Jin, H. Tang, H. Wang, Y. Chen, Highly hydrophilic poly(vinylidene fluoride)/meso-titania hybrid mesoporous membrane for photocatalytic membrane reactor in water, Sci. Rep. 6 (2016) 1–10. doi:10.1038/srep19148.

[171] H. Choi, A.C. Sofranko, D.D. Dionysiou, Nanocrystalline TiO2 photocatalytic membranes with a hierarchical mesoporous multilayer structure: Synthesis, characterization, and multifunction, Adv. Funct. Mater. 16 (2006) 1067–1074. doi:10.1002/adfm.200500658.

[172] J. Ciro, S. Mesa, J.F. Montoya, J.I. Uribe, R. Betancur, F. Jaramillo, Simultaneous top and bottom perovskite interface engineering by fullerene surface modification of titanium dioxide as electron transport layer, ACS Appl. Mater. Interfaces. 9 (2017) 29654–29659. doi:10.1021/acsami.7b06343.

[173] A. Brzózka, A. Brudzisz, K. Hnida, G.D. Sulka, Chemical and Structural Modifications of Nanoporous Alumina and Its Optical Properties, in: D. Losic and A. Santos (eds.) (Ed.), Electrochem. Eng. Nanoporous Mater., Springer International Publishing, Switzerland, 2015: pp. 219–288. doi:10.1007/978-3-

319-20346-1.

[174] M. Aramesh, J. Cervenka, Surface Modification of Porous Anodic Alumina for Medical and Biological Applications, in: Nanomedicine, Melbourne, 2014: pp. 439–467.

[175] S. Shingubara, Fabrication of nanomaterials using porous alumina templates, J. Nanoparticle Res. 5 (2003) 17–30. doi:10.1023/A:1024479827507.

[176] D.M. Giolando, Nano-crystals of titanium dioxide in aluminum oxide: A transparent self-cleaning coating applicable to solar energy, Sol. Energy. 97 (2013) 195–199. doi:10.1016/j.solener.2013.08.024.

[177] G. Celep, E. Cottancin, J. Lermé, M. Pellarin, L. Arnaud, J. Huntzinger, J. Vialle, M. Broyer, B. Palpant, O. Boisron, P. Mélinon, Optical properties of copper clusters embedded in alumina: An experimental and theoretical study of size dependence, Phys. Rev. B. 70 (2004) 165409. doi:10.1103/PhysRevB.70.165409.

[178] N. V. Gaponenko, I.S. Molchan, D.A. Tsyrkunov, G.K. Maliarevich, M. Aegerter, J. Puetz, N. Al-Dahoudi, J. Misiewicz, R. Kudrawiec, V. Lambertini, N. Li Pira, P. Repetto, Optical and structural properties of sol-gel derived materials embedded in porous anodic alumina, Microelectron. Eng. 81 (2005) 255–261. doi:10.1016/j.mee.2005.03.016.

[179] D. Perednis, L.J. Gauckler, Thin Film Deposition Using Spray Pyrolysis, J. Electroceramics. 14 (2005) 103–111.

[180] G. Cao, Nanostructures & Nanomaterials: Synthesis, Properties & Applications, Imperial College press, 2004.

[181] W.F. Zhang, M.S. Zhang, Z. Yin, Microstructures and Visible Photoluminescence of TiO2 Nanocrystals, Phys. Status Solidi A. 179 (2000) 319–327. doi:10.1002/1521-396X(200006)179:2<319::AID-PSSA319>3.0.CO;2-H.

[182] A.M.E. Raj, V. Agnes, V. Bena Jothy, C. Ravidhas, J. Wollschläger, M. Suendorf, M. Neumann, M. Jayachandran, C. Sanjeeviraja, Spray deposition and property analysis of anatase phase titania (TiO2) nanostructures, Thin Solid Films. 519 (2010) 129–135. doi:10.1016/j.tsf.2010.07.073.

[183] J.M. Herrmann, Heterogeneous photocatalysis: Fundamentals and applications to the removal of various types of aqueous pollutants, Catal. Today. 53 (1999) 115–129. doi:10.1016/S0920-5861(99)00107-8.

[184] H. Angus Macleod, Thin Film Optical Filters, CRC Press, 2010.

[185] M. Born, E. Wolf, Principles of Optics, Max Born and Emil Wolf, 1985.

[186] G. Hass, Physics of Thin Films, ACADEMIC PRESS INC, Virginia, 1963.

[187] S.M. Aguilar-Sierra, F. Echeverría E, Improvement of Electropolishing of 1100 Al Alloy for Solar Thermal Applications, J. Mater. Eng. Perform. 27 (2018) 1387–1395. doi:10.1007/s11665-018-3212-2.

[188] M.D. Abràmoff, P.J. Magalhães, S.J. Ram, Image processing with imageJ, Biophotonics Int. 11 (2004) 36–42.

[189] E.D. Palik, Handbook of Optical Constants of Solids, ACADEMIC PRESS LIMITED, 1997.

[190] A.D. Rakic, A.B. Djurisic, J.M. Elazar, M.L. Majewski, Optical properties of metallic films for vertical-cavity optoelectronic devices., Appl. Opt. 37 (1998) 5271–5283. doi:10.1364/AO.37.005271.

[191] W.L. Xu, M.J. Zheng, S. Wu, W.Z. Shen, Effects of high-temperature annealing on structural and optical properties of highly ordered porous alumina membranes, Appl. Phys. Lett. 85 (2004) 4364–4366. doi:10.1063/1.1815072.

[192] X. Sun, F. Xu, Z. Li, W. Zhang, Photoluminescence properties of anodic alumina membranes with ordered nanopore arrays, J. Lumin. 121 (2006) 588–594. doi:https://doi.org/10.1063/1.1815072.

[193] Y. Li, G.H. Li, G.W. Meng, L.D. Zhang, F. Phillipp, Photoluminescence and optical absorption caused by the F+ centres in anodic alumina membranes, J. Phys. Condens. Matter. 13 (2001) 2691–2699. doi:10.1088/0953-8984/13/11/323.

[194] G.H. Li, Y. Zhang, Y.C. Wu, L.D. Zhang, Wavelength dependent photoluminescence of anodic alumina membranes, J. Phys. Condens. Matter. 15 (2003) 8663–8671. doi:10.1088/0953-8984/15/49/034.

[195] Y. Yamamoto, N. Baba, S. Tajima, Coloured materials and photoluminiscence centres in anodic film on aluminium, Nature. 289 (1981) 572–574.

[196] Y. Yamamoto, N. Baba, Nature of the carboxilate species incorporated in anodic alumina films formed in oxalic acid solution, Thin Solid Films. 101 (1983) 329–338.

[197] G.C. Wood, A Model for the Incorporation of Electrolyte Species into Anodic Alumina, J. Electrochem. Soc. 143 (1996) 74. doi:10.1149/1.1836389.

[198] T. Gao, G. Meng, L. Zhang, Blue luminescence in porous anodic alumina films: the role of the oxalic impurities, J. Phys. Condens. Matter. 15 (2003) 2071–2079. doi:10.1088/0953-8984/15/12/324.

[199] A. Santos, M. Alba, M.M. Rahman, P. Formentín, J. Ferré-Borrull, J. Pallarès, L.F. Marsal, Structural tuning of photoluminescence in nanoporous anodic alumina by hard anodization in oxalic and malonic acids, Nanoscale Res. Lett. 7 (2012) 228. doi:10.1186/1556-276X-7-228.

[200] B. Hu, M. Yao, R. Xiao, J. Chen, X. Yao, Optical properties of amorphous Al2O3 thin films prepared by a sol-gel process, Ceram. Int. 40 (2014) 14133–14139. doi:10.1016/j.ceramint.2014.05.148.

[201] W.L. Xu, H. Chen, M.J. Zheng, G.Q. Ding, W.Z. Shen, Optical transmission spectra of ordered porous alumina membranes with different thicknesses and porosities, Opt. Mater. (Amst). 28 (2006) 1160–1165. doi:10.1016/j.optmat.2005.07.003.

[202] P. Nayar, A. Khanna, D. Kabiraj, S.R. Abhilash, B.D. Beake, Y. Losset, B. Chen, Structural, optical and mechanical properties of amorphous and crystalline alumina thin films, Thin Solid Films. 568 (2014) 19–24. doi:10.1016/j.tsf.2014.07.053.

[203] H. Yan, Preparation and optical characterization of nanoporous templates as a basis for nanocontact arrays, Technischen Universität Carolo-Wilhelmina zu Braunschweig, 2012.

[204] A. Brudzisz, A. Brzózka, G.D. Sulka, Effect of processing parameters on pore

opening and mechanism of voltage pulse detachment of nanoporous anodic alumina, Electrochim. Acta. 178 (2015) 374–384. doi:10.1016/j.electacta.2015.08.005.

[205] T. Kumeria, D. Losic, Controlling interferometric properties of nanoporous anodic aluminium oxide, Nanoscale Res. Lett. 7 (2012) 88. doi:10.1186/1556-276X-7-88.

[206] Y.F. Liu, Y.F. Tu, S.Y. Huang, J.P. Sang, X.W. Zou, Effect of etch-treatment upon the intensity and peak position of photoluminescence spectra for anodic alumina films with ordered nanopore array, J. Mater. Sci. 44 (2009) 3370–3375. doi:10.1007/s10853-009-3440-9.

[207] Z. Li, K. Huang, Optical properties of alumina membranes prepared by anodic oxidation process, J. Lumin. 127 (2007) 435–440. doi:10.1016/j.jlumin.2007.02.001.

[208] A. Rauf, M. Mehmood, M. Ahmed, M. ul Hasan, M. Aslam, Effects of ordering quality of the pores on the photoluminescence of porous anodic alumina prepared in oxalic acid, J. Lumin. 130 (2010) 792–800. doi:10.1016/j.jlumin.2009.11.035.

[209] L. Cantelli, J.S. Santos, T.F. Silva, M.H. Tabacniks, A.O. Delgado-Silva, F. Trivinho-Strixino, Unveiling the Origin of Photoluminescence in Nanoporous Anodic Alumina (NAA) Obtained by Constant Current Regime, J. Lumin. (2018). doi:10.1016/j.jlumin.2018.10.015.

[210] J.H. Chen, C.P. Huang, C.G. Chao, T.M. Chen, The investigation of photoluminescence centers in porous alumina membranes, Appl. Phys. A Mater. Sci. Process. 84 (2006) 297–300. doi:10.1007/s00339-006-3623-z.

[211] T.E. Nee, C.H. Fang, Y.R. Chen, J.C. Wang, P.L. Fan, J.A. Jiang, Characterization of the anomalous luminescence properties from self-ordered porous anodic alumina with oxalic acid electrolytes, Thin Solid Films. 518 (2009) 1439–1442. doi:10.1016/j.tsf.2009.09.079.

[212] Y. Li, C.-W. Wang, L.-R. Zhao, W.-M. Liu, Photoluminescence properties of porous anodic aluminium oxide membranes formed in mixture of sulfuric and oxalic acid, J. Phys. D. Appl. Phys. 42 (2009) 045407. doi:10.1088/0022-3727/42/4/045407.

[213] J. Wang, C.W. Wang, S.Y. Li, F. Zhou, The effect of oxalic and sulfuric ions on the photoluminescence of anodic aluminum oxide formed in a mixture of sulfuric and oxalic acid, Appl. Phys. A Mater. Sci. Process. 94 (2009) 939–942. doi:10.1007/s00339-008-4869-4.

[214] N.B.& S.T. Y. Yamamoto, Coloured materials and photoluminescence centres in anodic film on aluminium, Nature. 289 (1981) 572–574.

[215] Z. Li, K. Huang, The effect of high-temperature annealing on optical properties of porous anodic alumina formed in oxalic acid, Luminescence. 22 (2007) 355–361. doi:10.1002/bio.

[216] M. Ibadurrohman, K. Hellgardt, Morphological Modification of TiO_2 Thin Films as Highly Efficient Photoanodes for Photoelectrochemical Water Splitting, ACS Appl. Mater. Interfaces. 7 (2015) 9088–9097. doi:10.1021/acsami.5b00853.

[217] C. Pacholski, M. Sartor, M.J. Sailor, G.M. Miskelly, Biosensing Using Porous Silicon Double-Layer Interferometers, J Am Chem Soc. 127 (2008) 11636–11645. doi:10.1021/ja0511671.Biosensing.

[218] Y.B. Li, M.J. Zheng, L. Ma, High-speed growth and photoluminescence of porous anodic alumina films with controllable interpore distances over a large range, Appl. Phys. Lett. 91 (2007) 8–11. doi:10.1063/1.2772184.

[219] I. Vrublevsky, A. Jagminas, S. Hemeltjen, W.A. Goedel, Photoluminescent behavior of heat-treated porous alumina films formed in malonic acid, Appl. Surf. Sci. 256 (2010) 2013–2017. doi:10.1016/j.apsusc.2009.09.038.

[220] L. Cantelli, J.S. Santos, F. Trivinho-Strixino, The effect of anodization temperature on optical properties of nanoporous anodic alumina (NAA) films, J. Electroanal. Chem. 780 (2016) 386–390. doi:10.1016/j.jelechem.2016.01.009.

[221] Y.F. Mei, G.G. Siu, J.P. Zou, X.L. Wu, Color centers vs electrolytes for Si-based porous anodic alumina, Phys. Lett. Sect. A Gen. At. Solid State Phys. 324 (2004) 479–483. doi:10.1016/j.physleta.2004.02.061.

[222] M. Ghrib, R. Ouertani, M. Gaidi, N. Khedher, M. Ben Salem, H. Ezzaouia, Effect of annealing on photoluminescence and optical properties of porous anodic alumina films formed in sulfuric acid for solar energy applications, Appl. Surf. Sci. 258 (2012) 4995–5000. doi:10.1016/j.apsusc.2011.12.056.

[223] G.S. Huang, X.L. Wu, G.G. Siu, P.K. Chu, On the origin of light emission from porous anodic alumina formed in sulfuric acid, Solid State Commun. 137 (2006) 621–624. doi:10.1016/j.ssc.2006.01.005.

[224] Y. Han, L. Cao, F. Xu, T. Chen, Z. Zheng, K. Qian, W. Huang, Quantitative investigation in the influence of oxalic impurities on photoluminescence properties of porous AAOs, Mater. Chem. Phys. 129 (2011) 1247–1251. doi:10.1016/j.matchemphys.2011.06.008.

[225] A. Santos Alejandro, Structural Engineering of Nanoporous Anodic alumina and Applications, 2010.

[226] C. Sevik, C. Bulutay, Theoretical study of the insulating oxides and nitrides: SiO2, GeO2, Al2O3, Si3N4, and Ge3N4, J. Mater. Sci. 42 (2007) 6555–6565. doi:10.1007/s10853-007-1526-9.

[227] H. Efeoğlu, T. Karacali, K. Meral, I.Y. Erdoğan, Y. Onganer, Anodization of aluminium thin films on p++Si and annihilation of strong luminescence from Al2O3, J. Lumin. 130 (2010) 157–162. doi:10.1016/j.jlumin.2009.08.002.

[228] J. Wang, C.-W. Wang, Y. Li, W.-M. Liu, Optical constants of anodic aluminum oxide films formed in oxalic acid solution, Thin Solid Films. 516 (2008) 7689–7694. doi:10.1016/j.tsf.2008.03.023.

[229] B. Ealet, M.H. Elyakhloufi, E. Gillet, M. Ricci, Electronic and crystallographic structure of gamma-alumina thin films, Thin Solid Films. 250 (1994) 92–100. doi:10.1016/0040-6090(94)90171-6.

[230] F. Bertó-Roselló, E. Xifré-Pérez, J. Ferré-Borrull, J. Pallarès, L.F. Marsal, Nanoporous Anodic Alumina 3D FDTD Modelling for a Broad Range of Inter-pore Distances, Nanoscale Res. Lett. 11 (2016) 359. doi:10.1186/s11671-016-1575-6.

[231] D. Kuang, R. Charrière, N. Matsapey, M. Flury, J. Faucheu, P. Chavel, Modeling the specular spectral reflectance of partially ordered alumina nanopores on an aluminum substrate, Opt. Express. 23 (2015) 4506. doi:10.1364/OE.23.004506.

[232] I.V. Gasenkova, N.I. Mukhurov, S.P. Zhvavyi, E.E. Kolesnik, A.P. Stupak, Photoluminescent properties of nanoporous anodic alumina doped with manganese ions, J. Lumin. 185 (2017) 298–305. doi:10.1016/j.jlumin.2017.01.030.

[233] B.D. Evans, M. Stapelbroek, Optical properties of the F+ center in crystalline Al2O3, Phys. Rev. B. 18 (1978) 7089–7098. doi:10.1103/PhysRevB.18.7089.

[234] F.F. Komarov, A. V. Mudryi, L.A. Vlasukova, N.I. Mukhurov, A. V. Ivanyukovich, Intense blue luminescence of anodic aluminum oxide, Opt. Spectrosc. (English Transl. Opt. i Spektrosk. 104 (2008) 235–237. doi:10.1007/s11449-008-2014-9.

[235] E.J. Anglin, M.P. Schwartz, V.P. Ng, L.A. Perelman, M.J. Sailor, Engineering the chemistry and nanostructure of porous silicon fabry-Pérot films for loading and release of a steroid, Langmuir. 20 (2004) 11264–11269. doi:10.1021/la048105t.

[236] H. Fan, T. Lin, W. Zhang, J. Ma, S. Lu, X. Zhu, Formation mechanism of petal-like micropattern and nano fi bers in porous anodic alumina, 90 (2017) 119–124.

[237] I. Oja, A. Mere, M. Krunks, R. Nisumaa, C.H. Solterbeck, M. Es-Souni, Structural and Electrical Characterization of TiO2 Films Grown by Spray Pyrolysis, Thin Solid Films. 515 (2006) 674–677. doi:10.1016/j.tsf.2005.12.243.